Angular Correlation and Polarization of X-rays Emitted from Highly Charged Ions

seit 1558

Dissertation

To Fulfill the Requirements for the Degree of
doctor rerum naturalium (Dr. rer. nat.)

Submitted to the Council of the Faculty of Physics and Astronomy
of the Friedrich Schiller University Jena

by M.Sc. **Zhongwen Wu**

born on 28.09.1987 in Gansu, P.R. China

Reviewers:

1. Prof. Dr. Stephan Fritzsche
   Helmholtz-Institut Jena, Jena, Germany
   Friedrich-Schiller-Universität Jena, Jena, Germany

2. Prof. Dr. Alexei N. Grum-Grzhimailo
   Lomonosov Moscow State University, Moscow, Russia

3. Priv.-Doz. Dr. Zoltán Harman
   Max-Planck-Institut für Kernphysik, Heidelberg, Germany

Date of defense: 16.05.2017

Contents

1 Introduction **1**

2 Density matrix theory **5**

2.1 Pure and mixed states 6

2.2 Spin density matrix and statistical tensors 7

2.2.1 Spin density matrix of a free electron 9

2.2.2 Spin density matrix of atomic bound states 10

2.2.3 Spin density matrix of a photon: Stokes parameters 11

2.3 A time-independent description 13

2.4 Application to particular atomic processes 15

2.4.1 Production of polarized states 15

2.4.2 Radiative decay of polarized states 17

2.5 Calculation of many-electron transition amplitudes 19

2.5.1 Overview of multi-configuration Dirac-Fock method 20

2.5.2 Calculation of transition amplitudes of atoms and ions 22

3 Atomic photoionization of tungsten: A comparison with experiments 23

3.1 Photoionization of atoms and ions 23

3.2 DM description of photoionization and subsequent decay 24

3.2.1 Alignment of excited states after photoionization 24

3.2.2 Density matrix of the emitted photons 25

3.2.3 Polarization of the emitted photons 26

3.3 Results and discussion 27

3.3.1 Degree of linear polarization of the Ly-$\alpha_{1,2}$ lines 27

3.3.2 Comparison with experimental measurements 29

4 Radiative electron capture of atomic ions: Probing of nuclear parameters 31

4.1 Radiative electron capture of few-electron ions 31

4.2 DM description of radiative electron capture and subsequent decay . 33

4.2.1 Alignment of hyperfine levels following radiative electron capture 34

4.2.2 Angular distribution of hyperfine-resolved transition lines . . . 36

4.2.3 Angular distribution of the $K\alpha_1$ emission line 36

4.2.4 Evaluation of hyperfine transition amplitudes 39
4.3 Results and discussion 41
4.3.1 Ions with nuclear spin $I = 1/2$ 41
4.3.2 Ions with nuclear spin $I > 1/2$ 45

5 Two-step radiative cascades via overlapping resonances: Identification of level splitting of ions 47
5.1 Radiative decays via overlapping resonances 47
5.2 DM description of two-step radiative cascades 49
5.2.1 Angular correlation of the two-step photons 50
5.2.2 Angular distribution of the second-step photons 52
5.2.3 Polarization of the second-step photons 52
5.2.4 A particular case: Application to lithiumlike ions 53
5.3 Results and discussion 57
5.3.1 Angular distribution of the second-step photons 58
5.3.2 Linear polarization of the second-step photons 60
5.3.3 Photon-photon angular correlation 62

6 Stimulated plus spontaneous decay of ions: Determination of the hyperfine splitting 65
6.1 Hyperfine splitting in heavy few-electron ions 65
6.2 DM description of stimulated plus spontaneous decay 67
6.2.1 Second-order hyperfine transition amplitudes 68
6.2.2 Density matrix of emitted spontaneous decay photons 71
6.2.3 Angular distribution and polarization parameters 72
6.3 Results and discussion 72
6.3.1 Laser intensities required for the stimulated decay 73
6.3.2 Angular distribution and polarization of the spontaneous decay photons 74

7 Summary & Outlook 79

Bibliography 85

List of Figures 99

List of Tables 103

Acknowledgements **105**

Curriculum Vitae **107**

Publications **109**

Ehrenwörtliche Erklärung (Declaration of Authorship) **111**

1 Introduction

Since the first discovery of x rays by Röntgen in 1895 [1, 2], there have been numerous applications in a variety of fields such as medical diagnostics, materials science, industry, and quality control. In contrast to these practical applications, in atomic physics people are usually more interested in exploring how these x rays are produced by atoms or ions and, especially, in using them as a tool to study structure and dynamics of atoms or ions. It has been demonstrated that these x rays are generally emitted from excited highly charged (heavy) ions following various fundamental atomic collision processes or light-matter interactions, such as, electron impact excitation, radiative or resonant electron capture, photoexcitation and photoionization. For this reason, there have been continuous theoretical and experimental interest in studying x-ray spectroscopy of excited atoms and especially highly charged ions over the past many decades. Nowadays, this kind of studies becomes more practical due to the experimental advances in the production and storage of highly charged ions, for instance, by employing electron beam ion trap [3–9], heavy-ion accelerator and ion storage ring facilities [10–15].

When highly charged ions came to the role, such studies opened new perspective with regard to the properties of simple few-electron ionic systems such as hydrogenlike or heliumlike heavy ions in extreme physical conditions, i.e., relativistic collision energies and strong Coulomb fields generated by the nuclei. Such extreme conditions usually lead to remarkable effects not only on the electronic structure of ions but also on their collision dynamics. For instance, the strong Coulomb fields of heavy nuclei can give rise to a remarkably pronounced quantum electrodynamical effect on their energy level structure owing to the resulting strong spin-orbital interactions[16–18] and also to enhanced radiative decay rates [19].

Among those x-ray spectroscopy studies, in particular, much attention has been paid to angle-resolved properties of emitted characteristic fluorescence photons, such as, the angular distribution and correlation as well as the (linear) polarization [20–27]. Compared to total decay rates of characteristic x-ray fluorescence photon emissions, these angle-resolved experimental observables are often more sensitive to the electronic structure of atoms or ions and hence have provided significant insights on the relativistic, many-electron and quantum electrodynamical effects in fundamental electron-electron or photon-electron interactions [28–31]. Because of such a known

sensitivity, x-ray angular distribution and linear polarization have been employed to study the Breit interaction [30–35] and the hyperfine interaction [36–38] in electron-ion collisions as well as the multipole mixing of the radiation fields in spontaneous (radiative) decays of ions [29, 39, 40]. From these studies it has been demonstrated, for instance, that the Breit interaction remarkably dominates the Coulomb repulsion in the resonant electron capture of initially lithiumlike ions and therefore results in a qualitative change in the expected angular and polarization behaviours of subsequently emitted characteristic (x-ray) fluorescence photons [30, 32]. Furthermore, it has been also proved that a combined measurement of fluorescence photon angular distribution and linear polarization enables a very precise determination of the ratio of the electric-dipole and magnetic-quadrupole transition amplitudes and thus of the corresponding transition rates without any assumptions concerning the population mechanism of the excited states [39]. Apart from these typical examples, very naturally, similar angular and polarization studies of characteristic fluorescence photons are also expected to serve for other different purposes.

In experiment, efficient studies of x-ray photon polarization and angular correlation become very universal nowadays. This should be attributed to the fast progress in the techniques of both the production and the detection of x-ray fluorescence photons. With the present-day experimental facilities such as electron beam ion traps or ion storage rings, all possible charge states of each of the (stable) elements in the periodic table can be produced, i.e., up to the highest charge state of the heaviest element — bare uranium U^{92+} [41, 42]. In an electron beam ion trap, highly charged ions are directly generated just by successive electron impact with initially neutral atoms of the element to be considered. At (heavy-)ion storage rings, however, some relatively low charge states of the atoms are first produced also by electron impact but, subsequently, these lowly charged ions are then accelerated at ion accelerators and further stripped in a foil up to the desired high charge state. Admittedly, these obtained highly charged ions with various charge states may radiate very abundant (x-ray) fluorescence photons in fundamental electron-ion collisions or photon-ion interactions, as already mentioned above.

Different photon detectors can be employed to record the x-ray fluorescence radiation from highly charged ions. To measure, for instance, the (linear) polarization of these x-rays, two-dimensionally segmented solid-state germanium detectors could serve as Compton polarimeters [19, 43]. The Compton techniques in x-ray photon polarimetry have been known since 1950s and thus been widely utilized in nuclear

physics for many decades [44]. Nowadays, high-purity position- and energy-sensitive germanium detectors can even cover hard x-ray region up to several hundreds of keV, which have significantly improved energy resolution and polarization sensitivity [19]. Besides the germanium photon detectors, very recently, a lithium-drifted silicon strip detector designed as a hard x-ray Compton polarimeter was employed to explore the linear polarization characteristics of scattered photons from the Rayleigh scattering of incident linearly polarized synchrotron radiation by a high-Z scatterer, gold [45]. Moreover, by using the state-of-the-art x-ray polarimeter which is based on multiple (four or six) 90° reflections at channel-cut silicon crystals with a Bragg diffraction angle very close to 45°, the polarization of x-ray (fluorescence) photons can be measured with extremely high precision [41, 46]. For example, the polarization purity of 6.457-keV and 12.914-keV x rays from a brilliant undulator light source was determined to the level of 2.4×10^{-10} and 5.7×10^{-10}, respectively [41]. The performance and possible applications of such a channel-cut silicon crystal x-ray polarimeter has been demonstrated in a measurement of the optical activity of a sucrose solution [41]. In addition to the polarization measurements of x-ray photons, their angular distribution or correlation can also be measured with the utilization of these photon detectors [39, 42].

As accompanied by continuous experimental advances in studying the polarization and correlation phenomena in atomic collisions with electrons or in light-matter interactions, the corresponding theoretical studies are performed very extensively as well. For instance, a very systematic theoretical formalism that is based on density matrix theory has been developed to study these angular and polarization properties of characteristic fluorescence photon emissions in basic atomic processes [47, 48]. Within the framework of this formalism, all different kinds of atomic scattering or collision processes can be considered as long as the associated *transition amplitudes* are known. In the subsequent chapter, we shall introduce the density matrix theory and such a formalism in great detail.

In this thesis, we will perform a series of theoretical case studies on the angular distribution or correlation as well as the linear polarization of (characteristic) x-ray fluorescence photons emitted from excited highly charged ions. Such studies are motivated by the known sensitivity of these polarization and angle-resolved observables with regard to the details of electron-electron, electron-nuclei, and electron-photon interactions as explained above and, thus, also by our intention to explore other weak interaction effects in atomic physics by analyzing these observables. We expect that

these angle-resolved properties of fluorescence photons could serve as a promising tool, for instance, to determine nuclear parameters of isotopes or to resolve small fine- and hyperfine-structure level splittings in the overlapping resonances of highly charged ions. These expectations are confirmed by the present simulation results for each of the case studies carried out within the framework of the developed density matrix formalism and of the multi-configuration Dirac-Fock (MCDF) method.

The present thesis is structured as follows. In Chapter 2, we shall introduce the theoretical basis of the work presented in this thesis — density matrix theory, based on which the associated formalisms for the case studies to be considered below are developed. Moreover, the MCDF method will be briefly reviewed for it will be used to calculate many-electron transition amplitudes necessary in these case studies. In order to compare with experimental results to explain the validity of the theoretical basis of the thesis, linear polarization of the characteristic Ly-$\alpha_{1,2}$ lines following inner-shell photoionization of tungsten by an unpolarized light will be investigated in Chapter 3. In the following chapters, specific case studies are further performed. For instance, in Chapter 4 we shall study the angular distribution of the characteristic $K\alpha_1$ line following radiative electron capture into excited $1s2p_{3/2}\ ^{1,3}P_{1,2}$ levels of heliumlike ions with nonzero nuclear spin. Apart from x-ray photon emissions from isolated energy levels, we shall also explore the angular and polarization behaviors of fluorescence photons emitted from overlapping resonances of atoms or ions. In Chapter 5, the photon polarization and angular distribution as well as the photon-photon angular correlation will be studied for characteristic photons emitted from two-step radiative cascades proceeding via overlapping resonances of highly charged ions. In addition, in Chapter 6 we shall propose a novel experimental scheme to determine hyperfine splittings in highly charged heliumlike ions by exploring the angular and polarization properties of fluorescence photon emissions from overlapping hyperfine resonances. Finally, the results of this thesis will be summarized and a brief outlook on further possibilities of extending the present studies will be given in Chapter 7.

2 Density matrix theory

In the polarization and angular correlation studies of fluorescence photons emitted from excited atomic or ionic states following various atomic processes with electrons or photons, the most convenient and elegant theoretical description has been given by the density matrix theory. The main merit of the density matrix is its analytical power in the construction of general formulae and their further application to particular atomic processes that are considered. Moreover, the use of the density matrix method also has the advantage of providing a uniform description to all quantum mechanical states of a system, regardless of whether they are completely known or not. If this density matrix technique is not utilized, it would be very burdensome to calculate, for instance, the probabilities or averages of physical quantities of a given system. The density-matrix representation of quantum mechanical states enables the maximum information of the system to be expressed in a concise way and hence averts unnecessary variables.

The concept of density matrix was introduced for the first time by von Neumann in 1927 to describe statistical concepts in quantum mechanics [49]. After that, for quite a long period of time the use of the density matrix has been mainly restricted to statistical physics. However, when it came to the sixties its applications became more and more universal in other fields of physics such as in solid state physics, laser physics, atomic and molecular physics, as described particularly in the review papers by Fano in 1957 [50] and by ter Haar in 1961 [51]. In modern atomic physics, for instance, the density matrix technique has become a very important tool for describing various quantum mechanical interference and correlation phenomena such as in scattering theory, optical pumping, and quantum beat spectroscopy [47, 48]. In particular, as far as we are concerned, this technique has been successfully applied to numerous case studies on the polarization and correlation properties of fluorescence emission in the course of light-matter and electron-matter interactions.

Since the theory of the density matrix and the associated statistical tensors has been stated in great detail in the above references, as the basis of our work presented in the thesis, we here just give a brief outline of it. First of all, in Section 2.1 we shall review the very fundamental concepts—pure and mixed states—in the density matrix theory. Such a starting point is necessary and significant, since the density matrix would not exist at all if there were no mixed states in quantum mechan-

ics. In the density matrix theory, the explicit form of a density matrix depends on the particular representation in which the density matrix is written. A particular case of a density matrix of a system is a spin density matrix. This is a density matrix of the system in the representation of (spin, orbital, and/or total) angular momenta, which is of special interest in atomic physics. In Section 2.2, we will recall the spin density matrix and corresponding statistical tensors for a free electron, an atomic bound state, and a photon. On the basis of the spin density matrix, the fundamentals for the description of atomic "transitions"—a time-independent description—in the density matrix theory will be discussed in Section 2.3. In the next section (Section 2.4), this time-independent description will be applied to the production and radiative decay of polarized atomic states, from which physical observables such as polarization and angular distribution of fluorescence photons will be further obtained. Moreover, since the density matrices of initial and final atomic states are typically expressed in terms of many-electron transition amplitudes in the time-independent description, in Section 2.5 we shall briefly review the multiconfiguration Dirac-Fock method, based on which these amplitudes of atoms and ions are calculated.

2.1 Pure and mixed states

The states of physical systems in quantum mechanics can be classified in two categories: pure and mixed states. Usually, quantum mechanics deals with phenomena in which a maximum of information is available about the system under consideration. This maximal information can be achieved, for instance, for a nonrelativistic spinning electron in a central field with a specified full set of quantum numbers (n, l, j, m), or for a spinless particle whose state at a certain time is exclusively represented by a wave function $\psi(\mathbf{r})$. States of maximal information are usually referred to as *pure states* or simply *states* [50].

A pure state is characterized by the fact that there must be an experiment giving a result predictable with certainty when it is performed on a system in that state and in that state only. For instance, spin-up polarization of a beam of electrons is characterized by a full transmission of each electron through a suitably oriented Stern-Gerlach apparatus, while no other spin polarization state is fully transmitted by the same apparatus. An experiment which characterizes uniquely a pure state and thus provides a maximal information about the state is called a *complete* experiment.

It is worthy to point out that the term *complete* here is relative, with respect to only one part of the variables of a system, instead of absolute. For instance, filtration through a Stern-Gerlach apparatus is a complete experiment with respect to the spin polarization of electrons, but has no any relevance to their energy. In the language of mathematics, a pure state is characterized by a certain state vector $|\psi\rangle$ or by a wave function $\psi(\mathbf{r})$ in an abstract Hilbert space, as utilized for the spinless particle above. A pure state can be either an eigenstate of a particular Hermitian operator or a linear superposition of a (complete) set of eigenstates of another arbitrary Hermitian operator.

Apart from the systems in a pure state, other quantum mechanical systems also occur, for which one can not find a complete experiment to give a unique and fully predictable result. For instance, no Stern-Gerlach apparatus admits or rejects with certainty a beam of randomly oriented electrons. In other words, the information on such systems is not maximal in the sense of the lack of a complete experiment. In analogy with the concept of pure state, states of non-maximal information are often called *mixed states* or *mixtures*, or literally, states which are not pure are referred to as *mixed states* [50]. Compared with pure states, no corresponding state vector $|\psi\rangle$ can be found for mixed states to characterize them. For this reason, the necessity of introducing a "proper" description to mixed states arises naturally. In fact, *density operator* (or *density matrix*) is just such a description. Although, for mixed states of a system, no complete experiment gives a unique result predictable with certainty, the states of the system can nevertheless be fully identified by any set of data sufficient to predict the statistical results of all conceivable observations on the system. In the following section, we shall discuss such a density matrix and corresponding statistical tensors.

2.2 Spin density matrix and statistical tensors

From the discussion of pure and mixed states above, the concept of density matrix was introduced very naturally, which appears as a description of mixed states in quantum mechanics. In the density matrix theory, mixed states of a system are often described by a statistical or density operator ρ, which operates in the abstract Hilbert space and generally are constructed as

$$\rho = \sum_n a_n \left|\psi_n\right\rangle\left\langle\psi_n\right|, \tag{2.1}$$

where $|\psi_n\rangle$ is a complete set of state vectors, and a_n denotes the weight coefficients that are real positive numbers and characterize the probability of finding the system in a particular pure state. The density operator can be regarded as a generalization of the concept of state vector for pure states. Every mixed state is characterized by its density operator.

As well known, in quantum mechanics, the explicit form of a wave function which describes a pure state $|\psi\rangle$ depends on a given representation, say, ξ: $\psi(\xi) = \langle\xi|\psi\rangle$. Similarly, as mentioned above, the explicit form of a density matrix characterizing a mixed state also depends on a particular representation, for instance, ζ, on which the corresponding density operator ρ operates:

$$\langle\zeta|\rho|\zeta'\rangle = \sum_n a_n \langle\zeta|\psi_n\rangle \langle\psi_n|\zeta'\rangle = \sum_n a_n \psi_n(\zeta) \psi_n^*(\zeta') . \tag{2.2}$$

The matrix of the density operator such as $\langle\zeta|\rho|\zeta'\rangle$ is called the *density matrix*. It is worthy to point out that although the density matrix needs to be written out in a particular representation, the results of all physical observables such as mean values, polarization and angular correlation, are independent of the chosen representation.

A special case of the density operator (2.1) and the corresponding density matrix (2.2) is that only one weight coefficient is equal to unity and hence all others are zero. In this case, the system described by this density matrix is in a pure state $|\psi\rangle$. It follows from Eq. (2.1) that the density operator for the pure state $|\psi\rangle$ is given by

$$\rho = |\psi\rangle\langle\psi| , \tag{2.3}$$

and, accordingly, the corresponding density matrix is given by

$$\langle\zeta|\rho|\zeta'\rangle = \langle\zeta|\psi\rangle \langle\psi|\zeta'\rangle = \psi(\zeta) \psi^*(\zeta') . \tag{2.4}$$

It can be seen that a pure state is a particular case of a mixed state. Therefore, the description of a system in terms of the density operator (or density matrix) is the most general form of quantum-mechanical description of the system.

Apart from the density matrix, an equivalent description of a system with angular momenta can be given by the so-called *statistical tensors* [47, 48]. Other equivalent names of the statistical tensors utilized in literatures are *state multipoles*, *multipole moments*, *tensors of orientation*, and so on [48]. Here, we consider a very general case where a system is characterized by an angular momentum j that is well defined or that can take other different values such as j'. In this case, the statistical tensors

are constructed in terms of the elements of the density matrix $\langle jm|\rho|j'm'\rangle$ as follows [47]:

$$\rho_{kq}(j,j') = \sum_{mm'} (-1)^{j'-m'} \langle jm, j'-m'|kq\rangle \langle jm|\rho|j'm'\rangle \,, \tag{2.5}$$

where $\langle jm, j'-m'|kq\rangle$ represents the Clebsch-Gordan coefficients, rank k takes all integer numbers between $|j-j'|$ and $j+j'$ at fixed j and j', and for each number of k, component q runs over also all integers from $-k$ to $+k$. It is noted that the number of the statistical tensors $\rho_{kq}(j,j')$ is given by $\sum_k(2k+1) = (2j+1)(2j'+1)$, which is identical to the number of the elements of the density matrix $\langle jm|\rho|j'm'\rangle$. Compared with the density matrix, the main advantage of the statistical tensors is that they are easily transformable under different coordinate systems (and/or reference frames). With the use of the orthogonality of the Clebsch-Gordan coefficients, the inverse transformation of Eq. (2.5) is given by [47]

$$\langle jm|\rho|j'm'\rangle = \sum_{kq} (-1)^{j'-m'} \langle jm, j'-m'|kq\rangle \, \rho_{kq}(j,j') \,. \tag{2.6}$$

In atomic physics, for instance, the polarization and angular correlation properties of particles are described by means of the density matrix such as $\langle jm|\rho|j'm'\rangle$ in the representation of angular momenta, which is usually referred to as *spin density matrix*. The order and particular form of such a spin density matrix depend on the magnitude of the relevant angular momentum and on the physical properties of the considered particles. In the following subsections, in particular, we shall consider the spin density matrix and corresponding statistical tensors for three cases of special interest: a free electron (Subsection 2.2.1), an atomic (or ionic) bound state (Subsection 2.2.2), and a photon (Subsection 2.2.3).

2.2.1 Spin density matrix of a free electron

Owing to the fact that electrons have a spin $S = 1/2$, which has only two allowed projections $m_s = \pm 1/2$, the spin density matrix $\langle \frac{1}{2} m_s|\rho|\frac{1}{2} m_s'\rangle$ of a free electron is a 2×2 matrix. In quantum mechanics, any 2×2 Hermitian matrix can be expanded in terms of the identity matrix I and the Pauli matrices σ_x, σ_y and σ_x as follows,

$$\rho = \frac{1}{2} \left(I + P_x\sigma_x + P_y\sigma_y + P_z\sigma_z\right) = \frac{1}{2} \left(I + \boldsymbol{P}\boldsymbol{\sigma}\right) , \tag{2.7}$$

where the normalization constant $\frac{1}{2}$ has been chosen in accordance with the condition $\mathrm{Tr}\rho = 1$, and where P_x, P_y, and P_z forming the vector $\boldsymbol{P}$ represent real expansion coefficients. Since all of the density matrices are positively defined Hermitian matrix, Eq. (2.7) is also applicable to the spin density matrix $\langle \frac{1}{2} m_s | \rho | \frac{1}{2} m'_s \rangle$. By utilizing the explicit form of the Pauli matrices $\boldsymbol{\sigma}$, one can readily obtain [47, 48]

$$\rho_{m_s m'_s} \equiv \left\langle \frac{1}{2} m_s \middle| \rho \middle| \frac{1}{2} m'_s \right\rangle = \frac{1}{2} \begin{pmatrix} 1 + P_z & P_x - iP_y \\ P_x + iP_y & 1 - P_z \end{pmatrix} . \tag{2.8}$$

Here, the first m_s and second m'_s indices indicate the line and column of the matrix, respectively. Furthermore, the first line (column) corresponds to the spin projection $m_s(m'_s) = +1/2$, and the second one to $m_s(m'_s) = +1/2$. In fact, for this particular case of the spin density matrix of a free electron, the arbitrarily introduced vector $\boldsymbol{P}$ coincides with the *spin polarization vector* of the electron expressed in a particular Cartesian coordinate system. While the vector $\boldsymbol{P}$ points along the direction of the average spin of the electron, its magnitude P is the *degree of spin polarization* of the electron. If $P = 1$, one can say that the electron is in a pure spin state. Apart from the density matrix (2.8), the corresponding statistical tensors $\rho_{kq}(\frac{1}{2}, \frac{1}{2}) \equiv \rho_{kq}(\frac{1}{2})$ can be obtained with the use of the definition (2.5),

$$\rho_{00}\left(\frac{1}{2}\right) = \frac{1}{\sqrt{2}} , \tag{2.9}$$

$$\rho_{10}\left(\frac{1}{2}\right) = \frac{1}{\sqrt{2}} P_z , \tag{2.10}$$

$$\rho_{1\pm1}\left(\frac{1}{2}\right) = \mp\frac{1}{2}(P_x \mp iP_y) . \tag{2.11}$$

Note that only the tensors with rank $k = 0, 1$ exist due to the electron spin $S = 1/2$.

2.2.2 Spin density matrix of atomic bound states

In contrast to a free electron described by a wave function with well-defined momentum $\mathbf{p}$ and spin projection m_s on the quantization axis, an atomic (or ionic) bound state is characterized by a set of quantum numbers αJM, which are the total angular momentum J, its projection M, and all others α required for its unique specification. The polarization of such an atomic bound state is usually described by the spin density matrix $\langle \alpha JM | \rho | \alpha JM' \rangle$ with $M, M' = -J, -J+1, ...J$ in the representation of total angular momentum. If the state is unpolarized, $\langle \alpha JM | \rho | \alpha JM' \rangle = \delta_{MM'}/(2J+1)$.

Instead of using the spin density matrix, moreover, it is usually more convenient to describe the atomic state by means of the corresponding statistical tensors, as given below,

$$\rho_{kq}(\alpha J) = \sum_{MM'} (-1)^{J-M'} \langle JM, J-M'|kq\rangle \langle \alpha JM|\rho|\alpha JM'\rangle \,. \tag{2.12}$$

Similar to Eq. (2.5), here, $k = 0, 1, ...2J$, and for each k, $q = -k, -k+1, ... + k$.

In the studies of the polarization and angular correlation of fluorescence photons emitted from excited states of atoms or ions following various atomic collisions, the statistical tensors (2.12) are usually renormalized with respect to the corresponding *zero*-rank tensor ρ_{00} as follows,

$$\mathcal{A}_{kq}(\alpha J) = \frac{\rho_{kq}(\alpha J)}{\rho_{00}(\alpha J)} \,. \tag{2.13}$$

The renormalized tensors (2.13) are generally referred to as the *reduced statistical tensors*, which are often employed to describe the relative population of individual (magnetic) substates $|\alpha JM\rangle$ of the energy level as labeled by αJ. For the $2p_{3/2}$ level of hydrogen or hydrogen-like ions, for example, we have

$$\mathcal{A}_{20}(J = 3/2) = \frac{N_{M=\pm 3/2} - N_{M=\pm 1/2}}{N_{M=\pm 3/2} + N_{M=\pm 1/2}} \,, \tag{2.14}$$

where $N_{M=\pm 1/2}$ and $N_{M=\pm 3/2}$ represent the number of atoms (or ions) in the states $|2p_{3/2}\, M{=}\pm 1/2\rangle$ and $|2p_{3/2}\, M{=}\pm 3/2\rangle$, respectively. The reduced statistical tensor $\mathcal{A}_{20}$ is also known as the so-called *alignment parameter*.

2.2.3 Spin density matrix of a photon: Stokes parameters

In classical optics, a monochromatic electromagnetic wave (or light beam) is characterized by three physical quantities: angular frequency ω, wave vector $\mathbf{k}$, and state of polarization that is defined by the electric field vector $\mathbf{E}$. However, when the theory of relativistic quantum optics is applied to the electromagnetic field, the light wave behaves in the interactions with matter as if it was composed of "individual" photons. In this subsection, we shall discuss the spin density matrix and corresponding statistical tensors of an individual photon with wave vector $\mathbf{k}$.

In contrast to the cases of a free electron and an atomic bound state, the spin density matrix of a photon needs special consideration. This is because photons are a type of "particle" without rest mass. Since photons possess an intrinsic spin of

1 and its projection λ on the wave vector $\mathbf{k}$, i.e., the *helicity*, can take only two values ± 1 due to the transverse nature of light, the spin density matrix of a photon can be written out in the helicity representation λ and therefore has a dimension of two. Similar to the case of a free electron, such a spin density matrix $\rho_{\lambda\lambda'}$ can also be parameterized by three real parameters. Actually, these real parameters can be given by a set of so-called *Stokes parameters* and, accordingly, $\rho_{\lambda\lambda'}$ takes the form

$$\rho_{\lambda\lambda'} \equiv \langle \mathbf{k}\lambda|\rho|\mathbf{k}\lambda'\rangle = \frac{I(\mathbf{k})}{2}\begin{pmatrix} 1+P_3 & -P_1+iP_2 \\ -P_1-iP_2 & 1-P_3 \end{pmatrix}. \tag{2.15}$$

In this parameterization, the first line (column) of the density matrix corresponds to $\lambda = +1$ and the second one to $\lambda = -1$. In optics, these Stokes parameters are often employed in experiments in order to characterize the intensity and the polarization properties of emitted fluorescence photons (or light). While both $P_{1,2}$ describe the degree (and direction) of linear polarization of the light in the plane perpendicular to the wave vector $\mathbf{k}$, P_3 gives rise to its degree of circular polarization.

Experimentally, the Stokes parameters are determined simply by measuring the intensities I_ϑ of the light which is linearly polarized under particular angles ϑ with regard to the "reaction plane" as defined by the incoming beam and emitted light. The first Stokes parameter P_1, for instance, is given by the intensities of the light with the electric field vector $\mathbf{E}$ parallel ($\vartheta = 0°$) and perpendicular ($\vartheta = 90°$) to the reaction plane,

$$P_1 = \frac{I_{0°} - I_{90°}}{I_{0°} + I_{90°}}. \tag{2.16}$$

Moreover, the parameter P_2 is defined as follows in a pretty similar way but by the intensities of the light corresponding to the angels $\vartheta = 45°$ and $135°$, respectively,

$$P_2 = \frac{I_{45°} - I_{135°}}{I_{45°} + I_{135°}}. \tag{2.17}$$

Besides the parameters $P_{1,2}$ that characterize the linear polarization of light, we here also present the definition of the circular polarization parameter P_3 for completeness although it is not studied further in the thesis,

$$P_3 = \frac{I_{\lambda=+1} - I_{\lambda=-1}}{I_{\lambda=+1} + I_{\lambda=-1}}, \tag{2.18}$$

where $I_{\lambda=+1}$ and $I_{\lambda=-1}$ denote the intensities of the light transmitted through polarizers that are fully transmittable only for photons with helicity $\lambda = +1$ and -1,

respectively.

The statistical tensors of a photon can be given in the representation of total angular momentum (or multipolarity) L of the photon, which are different from the case of the corresponding density matrix. In the photon frame of reference, only the statistical tensors with projections $0, \pm 2$ turn out to be nonzero. For dipole photons, for instance, they are expressed in terms of the Stokes parameters as follows,

$$\rho_{00} = \frac{1}{\sqrt{3}}\,, \;\; \rho_{10} = \frac{1}{\sqrt{2}} P_3\,, \;\; \rho_{20} = \frac{1}{\sqrt{6}}\,, \;\; \rho_{2\pm 2} = -\frac{1}{2}(P_1 \mp i P_2)\,. \tag{2.19}$$

As discussed above, the statistical tensors (2.19) are equivalent to the density matrix (2.15) with regard to the representation of photon polarization.

2.3 A time-independent description

As well known, the time evolution of a quantum-mechanical state vector $|\psi(t)\rangle$ is described by the time-dependent Schrödinger equation. Likewise, the time evolution of a density operator $\rho(t_0)$ at time t_0 can also be achieved by a unitary transformation with the time evolution operator such as $U(t, t_0)$ from time t_0 to t [47, 48],

$$\rho(t) = U(t, t_0)\, \rho(t_0)\, U^{+}(t, t_0)\,. \tag{2.20}$$

This kind of time evolution is fully governed by the *Liouville equation*, which is given as follows (in atomic units $m_e = 1$, $e = 1$, $\hbar = 1$) [47]:

$$i\frac{\partial \rho(t)}{\partial t} = [H, \rho(t)]\,, \tag{2.21}$$

where H is the Hamiltonian of the system as described by the density operator $\rho(t)$.

A particular case of such a time evolution is the "transition" in atomic collision or decay processes. The transition starts from an initial state (i) of a composite system that is prepared at an "infinite time" before the processes and then reaches a final state (f) of the composite system at an "infinite time" after the processes. Similar to the scattering theory, such a transition is described by a *transition operator* T, which relates the density operators ρ^i and ρ^f of the initial i and final f states as follows [47, 48],

$$\rho^f = T\, \rho^i\, T^{+}\,. \tag{2.22}$$

The corresponding density matrix form of Eq. (2.22) depends on a (set of) particular

representation. If, for instance, the total angular momentum representations $\alpha_0 j_0 m_0$ and $\alpha j m$ are utilized for the initial i and final f states, respectively, such a density matrix form takes

$$\begin{aligned}
&\langle \alpha j m|\rho^f|\alpha' j' m'\rangle \\
&= \langle \alpha j m|T\Big(\sum_{\alpha_0 j_0 m_0}|\alpha_0 j_0 m_0\rangle\langle\alpha_0 j_0 m_0|\Big)\rho^i\Big(\sum_{\alpha_0' j_0' m_0'}|\alpha_0' j_0' m_0'\rangle\langle\alpha_0' j_0' m_0'|\Big)T^+|\alpha' j' m'\rangle \\
&\equiv \sum_{\alpha_0 j_0 m_0,\,\alpha_0' j_0' m_0'}\langle \alpha j m|T|\alpha_0 j_0 m_0\rangle\,\langle\alpha' j' m'|T|\alpha_0' j_0' m_0'\rangle^*\,\langle\alpha_0 j_0 m_0|\rho^i|\alpha_0' j_0' m_0'\rangle \\
&\equiv \sum_{\alpha_0 j_0 m_0,\,\alpha_0' j_0' m_0'}\langle \alpha j m|T|\alpha_0 j_0 m_0\rangle\,\langle\alpha' j' m'|T|\alpha_0' j_0' m_0'\rangle^*\,\langle\alpha_0 j_0 m_0|\rho^i|\alpha_0' j_0' m_0'\rangle\,\delta_{jj_0}\,\delta_{j'j_0'} \\
&\qquad\qquad \times \delta_{mm_0}\,\delta_{m'm_0'}\,. \qquad (2.23)
\end{aligned}$$

In this expression, $\langle\alpha_0 j_0 m_0|\rho^i|\alpha_0' j_0' m_0'\rangle$ and $\langle\alpha j m|\rho^f|\alpha' j' m'\rangle$ are the density matrices of the initial and final states, respectively, and $\langle\alpha j m|T|\alpha_0 j_0 m_0\rangle$ represents the transition amplitudes of the particular "transition" as described by the operator T. Moreover, the four Kronecker deltas in the third equation occur due to the fact that the transition operator conserves the total angular momentum and its projection on the quantization axis.

Besides utilizing Eq. (2.23), in practice, it is usually more convenient to employ the corresponding statistical tensor form,

$$\rho^f_{kq}(\alpha j,\alpha' j') = \frac{1}{\hat{j}\hat{j}'}\sum_{\alpha_0\alpha_0'}\langle\alpha j\|T\|\alpha_0 j_0\rangle\,\langle\alpha' j'\|T\|\alpha_0' j_0'\rangle^*\,\rho^i_{kq}(\alpha_0 j_0,\alpha_0' j_0')\,\delta_{jj_0}\,\delta_{j'j_0'}\,. \quad (2.24)$$

Here, $\hat{j}\hat{j}' \equiv \sqrt{(2j+1)(2j'+1)}$, $\langle\alpha j\|T\|\alpha_0 j_0\rangle$ represents the corresponding reduced transition amplitudes, $\rho^i_{kq}(\alpha_0 j_0,\alpha_0' j_0')$ and $\rho^f_{kq}(\alpha j,\alpha' j')$ are the respective statistical tensors of the initial and final states. It follows from Eq. (2.24) that the components of the statistical tensors of total angular momentum of a physical composite system evolve independently and therefore the composite system can not gain new components which are not present in its initial state. Moreover, it is instructive to indicate that Eq. (2.24) is derived with the use of the general relation (2.6) between the spin density matrix and corresponding statistical tensors, the *Wigner-Eckart theorem*, as well as the orthogonality of the Clebsch-Gordan coefficients.

As long as the statistical tensors of a composite system that consists of several subsystems are obtained after a particular atomic process, it is natural to separate

the statistical tensors of one of the subsystems. This is very important in practical applications that we will see in the following subsection. In the case of a composite system that consists of two subsystems 1 and 2 with the respective angular momenta j_1 and j_2, such a separation is given by [47]

$$\rho_{kq}^{(1)}(j_1, j_1') = \sum_{JJ'j_2} (-1)^{j_1+j_2+J'+k} \hat{J}\hat{J}' \begin{Bmatrix} j_1 & j_1' & k \\ J' & J & j_2 \end{Bmatrix} \rho_{kq}(j_1 j_2 J, j_1' j_2 J') \,. \quad (2.25)$$

In this equation, $\rho_{kq}(j_1 j_2 J, j_1' j_2 J')$ is a particular form with $j_2' = j_2$ of the statistical tensors $\rho_{kq}(j_1 j_2 J, j_1' j_2' J')$ of the composite system, and $\rho_{kq}^{(1)}(j_1, j_1')$ is the statistical tensors of its subsystem 1. Moreover, the standard notation of the Wigner $6j$ symbol has been utilized. Certainly, Eq. (2.25) can be generalized to the case of a composite system that consists of more than two subsystems.

2.4 Application to particular atomic processes

In this subsection, we shall apply the fundamental relations obtained in the previous subsection to two particular sorts of atomic processes: production (Subsection 2.4.1) and radiative decay (Subsection 2.4.2) of polarized atomic (and/or ionic) states. The formalism developed in this section can be readily applied to the polarization and angular correlation studies of emitted fluorescence photons. Before moving forward, here we must state clearly that the main content of this section as presented below is based on our paper [*Nucl. Instr. Meth. Phys. Res. B*, in press (2017)].

2.4.1 Production of polarized states

In atomic physics, atoms (or ions) can be polarized by a variety of atomic processes with electrons or photons, such as, electron impact excitation [36, 52], resonant electron capture [30–34], radiative electron capture [29, 39], inner-shell photoionization [53–56], and photoexcitation [56–58]. For the sake of simplicity, we consider below the resonant electron capture process

$$A^{q+}(\alpha_0 J_0) + \varepsilon e^-(lj) \quad \longrightarrow \quad A^{(q-1)+*}(\alpha J) \,. \quad (2.26)$$

In this process, a q-fold charged ion A^{q+} in its ground state $\alpha_0 J_0$ captures resonantly a free electron with kinetic energy ε as well as orbital and total angular momenta l and j, which results in the production of an excited state αJ of its neighboring

charged ion $A^{(q-1)+}$. While J_0 and J denote well-defined total angular momenta of the systems, α_0 and α refer to all other quantum numbers as required for a unique specification of the states. Before applying the general relation (2.24) to the process (2.26), we need to state that the initial ion A^{q+} is chosen as the reference frame and the free electron εe^- moves along the quantization z axis.

It follows from Eq. (2.24) that in order to obtain the statistical tensors of the excited state αJ one first needs to know both the reduced transition amplitudes of the process (2.26) and the statistical tensors of the initial state of the composite system that consists of the initial ion and the free electron. The reduced transition amplitudes can be formally expressed as $\langle \alpha J \| T \| \alpha_0 J_0, lj : J \rangle$ for the moment, the calculations of which will be discussed in the next section. As for the statistical tensors of the initial state of the composite system, they are simply given by

$$\begin{aligned} &\rho_{kq}(\alpha_0 J_0, lj : J;\, \alpha_0 J_0, l'j' : J) \\ &\quad = \sum_{k_0 q_0,\, k_e q_e} \hat{k_0} \hat{k_e} \hat{J}^2 \, \langle k_0 q_0, k_e q_e | k q \rangle \begin{Bmatrix} J_0 & j & J \\ J_0 & j' & J \\ k_0 & k_e & k \end{Bmatrix} \rho_{k_0 q_0}(\alpha_0 J_0)\, \rho_{k_e q_e}(j, j') \end{aligned} \tag{2.27}$$

in terms of the statistical tensors $\rho_{k_0 q_0}(\alpha_0 J_0)$ and $\rho_{k_e q_e}(j, j')$ of the initial ion and the free electron. Here, the standard notation for the Wigner $9j$ symbol has been used, and the indices k, q, k_0, q_0, k_e and q_e take similar numbers as in Eq. (2.5). Usually, the ground states of atoms (or ions) are unpolarized before a collision process and, therefore, $\rho_{k_0 q_0}(\alpha_0 J_0) = \hat{J}_0^{-1}\, \delta_{k_0 0}\, \delta_{q_0 0}$. In addition, since the total angular momentum of a free electron is coupled from its spin and orbital angular momenta, similar to Eq. (2.27) the statistical tensors $\rho_{k_e q_e}(j, j')$ of the free electron are expressed in terms of the statistical tensors of the spin and orbital angular momenta [47],

$$\rho_{k_e q_e}(j, j') = \sum_{k_l q_l,\, k_s q_s} \hat{k_l} \hat{k_s} \hat{j} \hat{j'} \, \langle k_l q_l, k_s q_s | k_e q_e \rangle \begin{Bmatrix} l & \frac{1}{2} & j \\ l' & \frac{1}{2} & j' \\ k_l & k_s & k_e \end{Bmatrix} \rho_{k_l q_l}(l, l')\, \rho_{k_s q_s}\left(\frac{1}{2}\right). \tag{2.28}$$

While the statistical tensors $\rho_{k_s q_s}(\frac{1}{2})$ are defined by Eqs. (2.9)–(2.11), the statistical tensors $\rho_{k_l q_l}(l, l')$ of the orbital angular momentum have the simple form [47]

$$\rho_{k_l q_l}(l, l') = \frac{(-1)^{l'}}{4\pi} \hat{l} \hat{l'} \, \langle l 0, l' 0 | k_l 0 \rangle \tag{2.29}$$

for the chosen quantization z axis and the frame of reference.

We are now ready to write out the statistical tensors $\rho_{kq}(\alpha J)$ of the excited state αJ after the resonant electron capture (2.26). The substitutions of Eqs. (2.27)–(2.29) and of the reduced transition amplitudes $\langle \alpha J \| T \| \alpha_0 J_0, lj : J \rangle$ into the fundamental relation (2.24) finally give rise to

$$\begin{aligned}
&\rho_{kq}(\alpha J) \\
&= \sum_{\substack{ll'jj' \\ k_s k_l}} \frac{1}{4\pi} \hat{k}_s \hat{k}_l \hat{J}_0^{-2} \hat{l}\hat{l}'\hat{j}\hat{j}' (-1)^{l'+j'+J_0+J+k} \langle k_l 0, k_s q | k q \rangle \langle l 0, l' 0 | k_l 0 \rangle \begin{Bmatrix} J & j' & J_0 \\ j & J & k \end{Bmatrix} \\
&\quad \times \begin{Bmatrix} l & \frac{1}{2} & j \\ l' & \frac{1}{2} & j' \\ k_l & k_s & k \end{Bmatrix} \langle \alpha J \| T \| \alpha_0 J_0, lj : J \rangle \langle \alpha J \| T \| \alpha_0 J_0, l'j' : J \rangle^* \rho_{k_s q}\left(\frac{1}{2}\right), \qquad (2.30)
\end{aligned}$$

from which the corresponding reduced statistical tensors $\mathcal{A}_{kq}(\alpha J)$ and the alignment parameter $\mathcal{A}_{20}(\alpha J)$, as defined in Subsection 2.2.2, can be readily obtained.

2.4.2 Radiative decay of polarized states

The excited states of atoms or ions produced in various atomic processes are usually not stable. The stabilization of these states is always accompanied with the emission of fluorescence photons (radiative decay) or electrons (non-radiative decay). In this subsection, the fundamental relation (2.24) will be applied to the radiative decay of polarized atomic (or ionic) states in order to derive the spin density matrix of emitted fluorescence photons. Below, for instance, we consider the following radiative decay of the ion $A^{(q-1)+*}(\alpha J)$ produced in the process (2.26) for consistency,

$$A^{(q-1)+*}(\alpha J) \quad \longrightarrow \quad A^{(q-1)+}\ (\alpha_f J_f) + \gamma(\hbar\omega)\,. \qquad (2.31)$$

Here, $\hbar\omega$ is the energy of the emitted γ photon, and its emission direction is described by the polar θ and azimuthal φ angles in the geometry as specified above.

Since the statistical tensors (2.30) of the excited αJ state have been obtained, it is straightforward to derive the density matrix of the emitted fluorescence γ photon. This can be accomplished in two steps: (i) Use the relation (2.24) again to obtain the statistical tensors of the final state [cf. "$A^{(q-1)+}\ (\alpha_f J_f) + \gamma$"], of the composite system after the radiative decay; (ii) Extract the statistical tensors of the γ photon with the use of Eq. (2.25) and then transform it to the corresponding density matrix

in the helicity representation. If we start with the first step, the statistical tensors of the final state of the composite system read as

$$\begin{aligned}&\rho_{kq}(\alpha_f J_f, pL : J;\, \alpha_f J_f, p'L' : J)\\ &\quad= \frac{1}{\hat{J}^2}\langle \alpha_f J_f \| H_\gamma(pL) \| \alpha J\rangle \langle \alpha_f J_f \| H_\gamma(p'L') \| \alpha J\rangle^* \rho_{kq}(\alpha J)\,,\end{aligned} \tag{2.32}$$

where $\langle \alpha_f J_f \| H_\gamma(pL) \| \alpha J\rangle$ denotes the reduced transition amplitudes for the radiative decay with well-defined multipolarity pL. If the final ion $A^{(q-1)+}$ $(\alpha_f J_f)$ remains unobserved, it follows from Eq. (2.25) that the statistical tensors of the fluorescence γ photon are extracted from $\rho_{kq}(\alpha_f J_f, pL : J;\, \alpha_f J_f, p'L' : J)$ as follows,

$$\rho_{kq}(pL,\, p'L') = (-1)^{J+J_f+L'+k}\, \hat{J}^2 \begin{Bmatrix} L & L' & k \\ J & J & J_f \end{Bmatrix} \rho_{kq}(\alpha_f J_f, pL : J;\, \alpha_f J_f, p'L' : J)\,. \tag{2.33}$$

It is worthy to point out that $\rho_{kq}(pL,\, p'L')$ denote statistical tensors of a photon in the representation of total angular momentum (or multipoles). Now, we are ready to finally write out the density matrix of the γ photon in the helicity representation, i.e., $\langle \mathbf{k}_\gamma \lambda | \rho | \mathbf{k}_\gamma \lambda' \rangle$. By transforming this density matrix to the one in the total angular momentum representation and then using the standard relation (2.6), we have

$$\begin{aligned}\langle \mathbf{k}_\gamma \lambda | \rho | \mathbf{k}_\gamma \lambda' \rangle = \frac{1}{8\pi} \sum_{pLp'L'kq} &\lambda^p \lambda'^{p'} \hat{L}\hat{L}' (-1)^{1+L'} \langle L\lambda, L' - \lambda' | k\lambda - \lambda' \rangle D^{k\,*}_{\lambda-\lambda' q}(0,\theta,\varphi)\\ &\times \rho_{kq}(pL,\, p'L')\,,\end{aligned} \tag{2.34}$$

where $\mathbf{k}_\gamma$ is the wave vector of the emitted fluorescence γ photon that is characterized by θ and φ, and where $D^{k\,*}_{\lambda-\lambda' q}(0,\theta,\varphi)$ represents the Wigner D-matrix.

So far, we have obtained the helicity density matrix $\langle \mathbf{k}_\gamma \lambda | \rho | \mathbf{k}_\gamma \lambda' \rangle$ of fluorescence photons emitted following some particular atomic process. When compared with the spin density matrix (2.15) of a photon, it can help us to study the polarization and angular distribution of the photons. In the dipole approximation of the radiation field, for instance, the polarization P_1 of the fluorescence γ photon is given by [47],

$$P_1(\theta,\varphi) = -\frac{\sqrt{\frac{3}{2}}\,\alpha_2^\gamma \sum_q \mathcal{A}_{2q}(\alpha J) \left[D^{2\,*}_{q2}(\varphi,\theta,0) + D^{2\,*}_{q-2}(\varphi,\theta,0) \right]}{1 + \alpha_2^\gamma \sqrt{\frac{4\pi}{5}} \sum_q \mathcal{A}_{2q}(\alpha J)\, Y_{2q}(\theta,\varphi)}\,. \tag{2.35}$$

Here, $Y_{2q}(\theta,\varphi)$ is a second-order spherical harmonics, and α_2^γ denotes the intrinsic anisotropy parameter of the particular $\alpha J \to \alpha_f J_f$ radiative decay, which depends on

total angular momenta of its initial and final states and is given by [47]

$$\alpha_2^\gamma = \sqrt{\frac{3}{2}}\,\hat{J}\,(-1)^{J+J_f+1} \left\{ \begin{array}{ccc} J & J & 2 \\ 1 & 1 & J_f \end{array} \right\} . \tag{2.36}$$

Apart from the polarizations of the γ photon, its angular distribution follows simply from the trace of the density matrix (2.34),

$$W(\theta,\varphi) \propto \frac{1}{4\pi}\left[1 + \alpha_2^\gamma \sqrt{\frac{4\pi}{5}} \sum_q \mathcal{A}_{2q}(\alpha J)\, Y_{2q}(\theta,\varphi)\right], \tag{2.37}$$

where the summation q runs over 0, ±1, and ±2. For most cases of atomic collision with electrons or photons, the collision system has only one preferential direction, say, the incoming direction of the projectile. In these cases, the angular distribution of the emitted fluorescence light is azimuthally symmetric, thus independent of the angle φ, and can be characterized only by a single *anisotropy parameter* β_2,

$$W(\theta) = \frac{I_0}{4\pi}\left[1 + \beta_2 P_2(\cos\theta)\right]. \tag{2.38}$$

Here, I_0 denotes total intensity of the emitted light, and $P_2(\cos\theta)$ is the second-order Legendre polynomial as a function of the polar angle θ. Thus, once the parameter β_2 is known, the corresponding angular distribution becomes known as well.

In the above, we have taken the resonant electron capture and subsequent radiative decay of ions as a simple example to show how the fundamental relation (2.24) presented in Section 2.3 is applied to atomic excitation and decay processes. While the analogues of the statistical tensors (2.30) for other atomic collision processes can be derived following the same procedures as above, Eqs. (2.32)–(2.38) obtained in this subsection are universal and thus applicable to other radiative decays of atoms (or ions). In the following chapters of case studies, we shall not show the derivation details of relevant formulae but just present necessary density-matrix formalism for the studies of photon polarization and angular correlation.

2.5 Calculation of many-electron transition amplitudes

As already mentioned in the previous two sections, in order to obtain the statistical tensors of final atomic states after a particular collision process or the density

matrix of subsequently emitted photons, one needs to know the reduced transition amplitudes of relevant atomic processes. It follows from quantum mechanics that in order to calculate atomic transition amplitudes one first has to know the structure of atoms as well as wave functions of the initial and final states of the "transition". Nowadays, there have been different semi-empirical, non-relativistic, and relativistic atomic structure theories that are used to study the structure of atoms or ions, such as, the Bohr model [59], the Hartree-Fock method [60], the many-body perturbation theory [61], and the MCDF method [62]. In the work presented in this thesis, in particular, the MCDF method is used to calculate transition amplitudes of atoms or ions that are necessary for photon polarization and angular correlation studies. Below, we will make a very brief overview of this method and discuss the calculations of these transition amplitudes.

2.5.1 Overview of multi-configuration Dirac-Fock method

In the MCDF method, the wave function of an atomic state with well-defined parity P, total angular momentum J, and its projection M on the quantization axis is approximated by a linear combination of a set of configuration-state functions (CSFs) with the same symmetry PJM [62, 63],

$$\Psi_\alpha(PJM) = \sum_{r=1}^{n_c} c_r(\alpha)\, \Phi_r(PJM)\,. \tag{2.39}$$

In this approximation, n_c represents the number of CSFs that are employed to construct the atomic-state function $\Psi_\alpha(PJM)$, and the expansion coefficients $c_r(\alpha)$ are referred to as the so-called configuration mixing coefficients. As required by the Pauli exclusion principle, the wave function of a N-electron atomic (or ionic) system should be anti-symmetric with regard to the interchange of coordinates of any two electrons. For this reason, the configuration-state functions $\Phi_r(PJM)$ are expressed by the anti-symmetric Slater determinant of relativistic one-electron orbitals,

$$\Phi_r(PJM) = \frac{1}{\sqrt{N!}} \begin{vmatrix} \psi_1(\boldsymbol{r_1}) & \psi_1(\boldsymbol{r_2}) & \cdots & \psi_1(\boldsymbol{r_N}) \\ \psi_2(\boldsymbol{r_1}) & \psi_2(\boldsymbol{r_2}) & \cdots & \psi_2(\boldsymbol{r_N}) \\ \vdots & \vdots & \vdots & \vdots \\ \psi_N(\boldsymbol{r_1}) & \psi_N(\boldsymbol{r_2}) & \cdots & \psi_N(\boldsymbol{r_N}) \end{vmatrix}. \tag{2.40}$$

Here, $N!$ is the factorial of N. Similar to the case of hydrogen atom or hydrogenlike ions, the one-electron orbital also has the following four-spinor form in a spherical

coordinate system, say, (r, θ, φ),

$$\psi_{n\kappa m}(\boldsymbol{r}) = \frac{1}{r} \begin{pmatrix} P_{n\kappa}(r)\, \chi_{\kappa m}(\theta, \varphi) \\ iQ_{n\kappa}(r)\, \chi_{-\kappa m}(\theta, \varphi) \end{pmatrix} . \tag{2.41}$$

In this four-spinor expression, n is the principal quantum number of bound electrons, κ is the Dirac (or relativistic) quantum number, which has $\kappa = \pm(j + \frac{1}{2})$ for $j = l \mp \frac{1}{2}$, and m is the projection of the total angular momentum j on the quantization axis. Moreover, $P_{n\kappa}(r)$ and $Q_{n\kappa}(r)$ denote the large and small components of the electron radial wave function, respectively. The two-component function $\chi_{\kappa m}(\theta, \varphi)$ is referred to as the spin-angular function and is defined by [63]

$$\chi_{\kappa m}(\theta, \varphi) = \sum_{m_s = \pm 1/2} \langle l, m - m_s; 1/2, m_s | jm \rangle\, Y_{l, m-m_s}(\theta, \varphi)\, \phi_{m_s} , \tag{2.42}$$

where $\langle l, m - m_s; 1/2, m_s | jm \rangle$ denotes a Clebsch-Gordan coefficient, $Y_{l,m-m_s}(\theta, \varphi)$ is a spherical harmonics, and

$$\phi_{+1/2} = \begin{pmatrix} 1 \\ 0 \end{pmatrix} , \quad \phi_{-1/2} = \begin{pmatrix} 0 \\ 1 \end{pmatrix} . \tag{2.43}$$

When the variational principle is applied to the expectation value of the Dirac-Coulomb Hamiltonian within the multi-configuration wave function expansion, one can obtain MCDF equations for both the one-electron radial wave functions and the configuration mixing coefficients. In practical calculations, a set of trial radial wave functions is employed to obtain initial values of the configuration mixing coefficients while the radial functions remain unchanged. And then, the radial functions are computed again while the mixing coefficients remain untouched. Such an iterative procedure stops when both of them converge respectively to a predetermined accuracy. Actually, in order to solve the MCDF equations, several widely used computer programs have been developed [63, 64]. One of them is the well-known "General-purpose Relativistic Atomic Structure Program (GRASP)" [64–67], which has the latest versions GRASP92 [66] and GRASP2K [67]. These programs have been applied to numerous atomic structure studies of atoms and their ions in the periodic table of elements. In the work presented in this thesis, the GRASP92 package has been employed to generate energy levels and wave functions of atomic states for the calculations of necessary transition amplitudes of atoms (or ions). In the following subsection, we will briefly explain how the obtained energy levels and wave functions are further utilized to calculate the many-electron transition amplitudes.

2.5.2 Calculation of transition amplitudes of atoms and ions

Once energy levels and wave functions of atomic (or ionic) states are obtained with the use of the GRASP92 program, one can employ them to further calculate the relevant transition amplitudes for involved atomic excitation and decay processes. For the processes with photons involved, the calculations of these transition amplitudes are governed by the radiation field of the photons. However, for the processes with free electrons involved, the Coulomb and Breit interactions govern the relevant transition amplitudes. In practice, there are different computer packages developed to perform such calculations. In the work presented in this thesis, we have employed the well-know RATIP package [68] to calculate necessary transition amplitudes for various atomic processes involved.

As a concluding remark of this chapter, we have discussed the fundamental density matrix formalism for the studies of fluorescence photon polarization and angular correlation. In the following chapters, we will apply this formalism to particular case studies of this kind and discuss the corresponding results obtained.

3 Atomic photoionization of tungsten: A comparison with experiments

In this chapter, we shall consider the linear polarization of characteristic x-ray fluorescence photons that are emitted following inner-shell photoionization of neutral atoms or highly charged ions. In particular, special attention is paid to the $Ly\text{-}\alpha_1$ ($3d_{5/2} \rightarrow 2p_{3/2}$) and $Ly\text{-}\alpha_2$ ($3d_{3/2} \rightarrow 2p_{3/2}$) emission lines of singly charged tungsten ions produced via inner-shell $2p_{3/2}$ ionization of neutral tungsten. In the following section, the photoionization of atoms and ions is reviewed. In Section 3.2, a density matrix formalism is presented for the description of photoionization and subsequent radiative decay, such as, for the alignment of excited ionic states after photoionization and for the polarization density matrix of subsequently emitted fluorescence photons. The formalism presented here is general, independent of particular atomic shell structures, and thus can be applied to any atoms or ions. Finally, the obtained linear polarizations of the $Ly\text{-}\alpha_{1,2}$ lines are discussed in Section 3.3, together with a comparison with experimental results.

Before proceeding with the following sections, here we must clearly indicate that the main content of this chapter as presented below is based on the theoretical part of our published paper [*Phys. Rev. A* **93**, 033409 (2016)].

3.1 Photoionization of atoms and ions

Photoionization is one of the most fundamental atomic processes occurring in light-matter interactions. In particular, the inner-shell photoionization of neutral atoms or (highly charged) ions results in the production of excited ionic states. The subsequent decay of these states may lead to the emission of characteristic fluorescence photons. Take a neutral atom such as A for example, the above photoionization and subsequent radiative decay can be formally formulated as,

$$\begin{aligned} A\ (\alpha_i J_i) + \hbar\omega \quad &\longrightarrow \quad A^+\ (\alpha_f J_f) + e^- \\ &\longrightarrow \quad A^+\ (\alpha_0 J_0) + \gamma + e^-\,, \end{aligned} \tag{3.1}$$

where the atom initially in its ground state $|\alpha_i J_i\rangle$ is photoionized into a hole state $A^+\ (\alpha_f J_f)$ by the ionizing photon $\hbar\omega$, and the subsequent decay of the hole state to

an energetically lower state $|\alpha_0 J_0\rangle$ gives rise to the fluorescence γ photon emission. While the spectroscopic analysis of characteristic fluorescence photons is widely performed in science and technology, in contrast, much less effort is placed on subtle signatures of these ionization and decay processes, such as the polarization of these photons. In the following section, we will present a general density-matrix formalism to study the polarization of fluorescence photons emitted following the ionization of atoms or (highly charged) ions by unpolarized light.

3.2 DM description of photoionization and subsequent decay

Theoretically, when one analyzes fluorescence photon emissions from atoms or ions, the production and subsequent radiative decay of excited atomic or ionic states are often treated separately. Such a treatment can be done most conveniently within the framework of the density-matrix (DM) theory. In this framework, the polarization of excited atomic energy levels is characterized by the associated density matrix or equivalently by the statistical tensors. As it is discussed in Section 2.4, here we just restrict ourselves to a rather short account of necessary density matrix formulae for the studies of photon polarization and refer to Refs. [54, 69] for more details.

3.2.1 Alignment of excited states after photoionization

Let us start this subsection with considering the first step of Equation (3.1), i.e., the photoionization of atoms. For the photoionization of atoms or ions by an unpolarized light beam, if the ionized photoelectron remains unobserved and the quantization (z) axis is chosen along the propagation direction of the beam, the statistical tensors of the photoion A^+ $(\alpha_f J_f)$ after the photoionization is given by [70]

$$\begin{aligned}\rho_{kq}(\alpha_f J_f) = \frac{\pi}{2J_i+1}\delta_{q0} \sum_{pLp'L'} \sum_{ljJJ'} \sum_{\lambda} i^{L+p-L'-p'} \lambda^{p+p'} [L, L', J, J']^{1/2} \\ \times (-1)^{J+J'+J_f+J_i+j+1} \langle L\lambda, L'-\lambda \,|\, kq\rangle \begin{Bmatrix} J_f & j & J' \\ J & k & J_f \end{Bmatrix} \begin{Bmatrix} J' & J_i & L' \\ L & k & J \end{Bmatrix} \\ \times \langle \alpha_f J_f, \epsilon lj : J \,\|\, H_\gamma(pL) \,\|\, \alpha_i J_i\rangle \langle \alpha_f J_f, \epsilon lj : J' \,\|\, H_\gamma(p'L') \,\|\, \alpha_i J_i\rangle^* . \end{aligned} \quad (3.2)$$

Equation (3.2) is obtained by the application of the basic relation (2.24) to atomic photoionization together with the use of the multipole expansion of radiation field

and the partial-wave expansion of free-electron wave function. In this equation, the short-hand notation $[a, b, ...] \equiv (2a+1)(2b+1)...$ has been utilized. Moreover, the reduced transition amplitudes $\langle \alpha_f J_f, \epsilon l j : J \parallel H_\gamma(pL) \parallel \alpha_i J_i \rangle$ describe the electron-photon interactions, which lead to the production of the excited resonance $|\alpha_f J_f\rangle$. While l and j denote the orbital and total angular momenta of the photoelectron, respectively, individual photons are characterized in terms of the electric ($p = 1$) and magnetic ($p = 0$) multipolarities pL.

In atomic collision theory, as discussed in Subsection 2.2.2, the statistical tensors (3.2) are usually renormalized with respect to the zero-rank tensor $\rho_{00}(\alpha_f J_f)$. These renormalized statistical tensors $\mathcal{A}_{kq}(\alpha_f J_f) = \rho_{kq}(\alpha_f J_f)/\rho_{00}(\alpha_f J_f)$ are often used to characterize the relative population (or polarization) of the associated atomic sub-states $|\alpha_f J_f M_f\rangle$. Actually, the polarization of photoions after the photoionization has been extensively studied both in theory and experiment [69, 71]. For instance, Kleiman *et al.* made a systematic theoretical study on the orientation and alignment of photoions produced via single photoionization of various neutral atoms with the ground state $^1S_0$ by using a single-configurational Hartree-Fock approach [72].

3.2.2 Density matrix of the emitted photons

After the inner-shell photoionization, the photoion A^+ appears to be in one of its excited states, that is, $|\alpha_f J_f\rangle$ as shown in Eq. (3.1), which decays subsequently to the energetically lower state $|\alpha_0 J_0\rangle$ with the emission of the fluorescence γ photon. In order to analyze the polarization properties of the emitted photon, one needs first obtain its helicity density matrix, i.e., $\langle \mathbf{k}_\gamma \lambda \,|\rho_\gamma|\, \mathbf{k}_\gamma \lambda' \rangle$, in which $\mathbf{k}_\gamma \equiv (\theta_\gamma, \varphi_\gamma)$ denotes the outgoing direction of the emitted γ photon in an arbitrarily defined coordinate system with its z axis as chosen along the ionizing photon beam. If, for instance, the polarization state of the final ion A^+ ($\alpha_0 J_0$) remains unobserved after the radiative decay, the density matrix of the γ photon is written as [70]

$$\begin{aligned}
\langle \mathbf{k}_\gamma \lambda \,|\, \hat{\rho}_\gamma \,|\, \mathbf{k}_\gamma \lambda' \rangle \;=\; & 2\pi \sum_{kqq'} \sum_{pLp'L'} D^k_{-qq'}(\varphi_\gamma, \theta_\gamma, 0) \rho_{kq}(\alpha_f J_f) i^{L'+p'-L-p} \lambda^p \lambda'^{p'} [L, L']^{1/2} \\
& \times (-1)^{J_0+J_f+k+q+1} \langle L\lambda, L' \, -\lambda' \,|\, k \, -q' \rangle \begin{Bmatrix} L & L' & k \\ J_f & J_f & J_0 \end{Bmatrix} \\
& \times \langle \alpha_0 J_0 \parallel H_\gamma(pL) \parallel \alpha_f J_f \rangle \langle \alpha_0 J_0 \parallel H_\gamma(p'L') \parallel \alpha_f J_f \rangle^* \,. \qquad (3.3)
\end{aligned}$$

In this density matrix, the reduced matrix elements $\langle \alpha_0 J_0 \,\|\, H_\gamma(pL) \,\|\, \alpha_f J_f \rangle$ denote the transition amplitudes of the radiative decay as presented in the second step of Equation (3.1). Moreover, $D^k_{-qq'}(\varphi_\gamma, \theta_\gamma, 0)$ represents the Wigner rotation D-matrix with its arguments φ_γ, θ_γ and 0 as characterized in terms of three Euler angles, which relate the propagation directions of the ionizing $\hbar\omega$ and fluorescence γ photons by means of the associated three-step rotations.

3.2.3 Polarization of the emitted photons

Once the density matrix (3.3) is obtained, one can readily utilize Equation (2.15) to study the polarization of the fluorescence γ photons. On the one hand, for instance, the linear polarization P_1 is given by

$$P_1(\mathbf{k}_\gamma) = -\frac{\langle \mathbf{k}_\gamma\, \lambda = +1 \,|\, \hat{\rho}_\gamma \,|\, \mathbf{k}_\gamma\, \lambda' = -1 \rangle + \langle \mathbf{k}_\gamma\, \lambda = -1 \,|\, \hat{\rho}_\gamma \,|\, \mathbf{k}_\gamma\, \lambda' = +1 \rangle}{\langle \mathbf{k}_\gamma\, \lambda = +1 \,|\, \hat{\rho}_\gamma \,|\, \mathbf{k}_\gamma\, \lambda' = +1 \rangle + \langle \mathbf{k}_\gamma\, \lambda = -1 \,|\, \hat{\rho}_\gamma \,|\, \mathbf{k}_\gamma\, \lambda' = -1 \rangle} \tag{3.4}$$

in terms of the elements of the density matrix. On the other hand, the linear polarization P_1 is characterized experimentally by Eq. (2.16), which can be determined simply by measuring the intensities of the emitted fluorescence light with its electric field vector parallel and perpendicular, respectively, to the reaction plane as defined by the ionizing photon beam and the emitted light.

Eqs. (3.2)–(3.4) presented above are general and thus can be applied to investigate the linear polarization of fluorescence photons following the photoionization of any atoms (or ions) by an unpolarized light beam. In the following, in particular, we will consider the Ly-$\alpha_{1,2}$ fluorescence photon emissions following the inner-shell $2p_{3/2}$ photoionization of tungsten atoms. If the Ly-α_1 ($3d_{5/2} \to 2p_{3/2}$, 8398 eV) and Ly-α_2 ($3d_{3/2} \to 2p_{3/2}$, 8335 eV) emission lines are observed in the geometry where $\theta_\gamma = 90^\circ$ and $\varphi_\gamma = 0^\circ$, for instance, their linear polarization P_1 can be parameterized, respectively, as [70]

$$P_1(Ly\text{-}\alpha_1) = \frac{3\mathcal{A}_{20}}{20 - \mathcal{A}_{20}}\,, \tag{3.5}$$

$$P_1(Ly\text{-}\alpha_2) = -\frac{3\mathcal{A}_{20}}{\mathcal{A}_{20} + 5}\,. \tag{3.6}$$

It is worthy to mention that Eqs. (3.5)–(3.6) are obtained within the electric-dipole ($E1$) approximation for the radiation field of the fluorescence light, i.e., by setting $p = p' = 1$ and $L = L' = 1$ in Equation (3.3). In this parameterization, moreover, it is noted that the linear polarization P_1 for both the two emission lines depends

only on the alignment parameter $\mathcal{A}_{20} \equiv \rho_{20}(2p_{3/2})/\rho_{00}(2p_{3/2})$ of the $2p_{3/2}$ hole-state produced via the photoionization.

As can be clearly seen from Eqs. (3.2)–(3.6), any further discussion of the linear polarization of the Ly-$\alpha_{1,2}$ emission lines has to be traced back to the computation of the reduced bound-free transition amplitudes $\langle \alpha_f J_f, \epsilon lj : J \,\|\, H_\gamma(pL) \,\|\, \alpha_i J_i \rangle$ as shown in Eq. (3.2). Similar to the treatment of the fluorescence light, if the radiation field of the ionizing light is treated also within the $E1$ approximation, there are only three photoionization channels that are allowed, i.e., $s_{1/2}$, $d_{3/2}$, and $d_{5/2}$ partial waves, due to the restriction of total angular momentum and parity conservations. Following the previous work [54, 69], these reduced transition amplitudes are calculated with the use of the GRASP92 [66] and RATIP [68] computer programs, which have been developed within the framework of the MCDF method, as discussed in Section 2.5. However, in the present calculation, a single-configurational approximation is employed to obtain the relevant atomic-state wave functions and energy levels. Such an approximation works well enough to obtain stable results for the inner-shell $2p_{3/2}$ photoionization and subsequent radiative decay of tungsten. While the CSFs are constructed as an anti-symmetric product of a set of orthonormal orbitals and then are optimized self-consistently on the basis of the Dirac-Coulomb Hamiltonian, the QED effect is further incorporated into the expansion coefficients $c_r(\alpha)$ by diagonalizing the Dirac-Coulomb-Breit Hamiltonian matrix within first-order perturbation theory.

3.3 Results and discussion

Once the reduced transition amplitudes $\langle \alpha_f J_f, \epsilon lj : J \,\|\, H_\gamma(pL) \,\|\, \alpha_i J_i \rangle$ are obtained for the partial waves $s_{1/2}$, $d_{3/2}$, and $d_{5/2}$, they can be used to calculate the alignment parameter $\mathcal{A}_{20}$ and further the linear polarization P_1 as given by Eqs. (3.5)–(3.6). In this section, we will discuss the obtained degree of linear polarization for the Ly-$\alpha_{1,2}$ lines following the inner-shell photoionization of tungsten and then compare them with the experimental results measured by a crystal-based spectropolarimeter.

3.3.1 Degree of linear polarization of the Ly-$\alpha_{1,2}$ lines

In Figure 3.1, we display the calculated degree of linear polarization of the Ly-$\alpha_{1,2}$ fluorescence emission lines following the inner-shell $2p_{3/2}$ ionization of tungsten by

an unpolarized photon beam, as functions of the ionizing photon energy in the range of 10–23 keV. The theoretical prediction shows a very weak dependence of the linear polarization on the ionizing photon energy for both the emission lines. For the Ly-α_1 ($3d_{5/2} \rightarrow 2p_{3/2}$) line, the most intense line from the L-shell emission, the obtained degree of linear polarization is positively signed and varies between +1% and +2% within the ionizing photon energy range. In contrast, the linear polarization of the Ly-α_2 ($3d_{3/2} \rightarrow 2p_{3/2}$) line has a negative sign and changes in the range –5% $\sim$ –7%. Since the sign of the degree of linear polarization describes the preferential polarization direction of emission photons, we obtain that such preferential directions are mutually perpendicular to each other for the Ly-$\alpha_{1,2}$ lines.

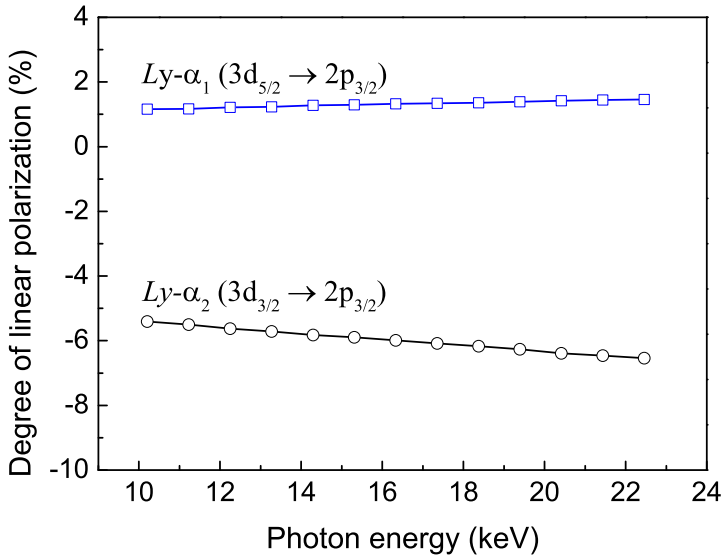

Figure 3.1: Degree of linear polarization of the Ly-α_1 ($3d_{5/2} \rightarrow 2p_{3/2}$; blue squares) and Ly-α_2 ($3d_{3/2} \rightarrow 2p_{3/2}$; black circles) fluorescence emission lines following the inner-shell $2p_{3/2}$ photoionization of tungsten by an unpolarized photon beam, as functions of the ionizing photon energy in the range of 10–23 keV. The photon energies of the Ly-α_1 and Ly-α_2 lines are calculated to be 8398 eV and 8335 eV, respectively. Calculations are performed within the MCDF method.

It is important to point out that the obtained weak dependence of the degree of linear polarization upon the ionizing photon energy is very helpful for a direct comparison with experimentally measured results. Due to such a weak dependence, for instance, the comparison between theoretical calculations and experimental measurements would not be affected by the non-monochromatic effect of the ionizing

photon radiation. In the following subsection, we will compare the above calculated degrees of linear polarization with the ones measured experimentally for both the Ly-$\alpha_{1,2}$ emission lines.

3.3.2 Comparison with experimental measurements

As discussed in Section 2.2.3, the linear polarization P_1 as given by Eqs. (3.5)–(3.6) can be determined in experiment simply by measuring the intensities of emitted fluorescence light with its electric field vector parallel and perpendicular to the reaction plane, respectively. In Fig. 3.2, the calculated degrees of linear polarization for both the Ly-$\alpha_{1,2}$ lines are compared with the experimental results that are measured with the utilization of a crystal-based spectropolarimeter [70]. Here, we will not discuss the detail of the experimental set-up and technique such as the ionizing light source, target and spectropolarimeter, but just make such a comparison and explain the validity of it. Firstly, although the theoretical method presented above is for isolated atoms (or ions) and the experiment is performed for solid-state tungsten, nevertheless, it can still be applied to account for the experimental results. For inner-shell such as $2p$ and $3d$ electrons of high-Z atoms like tungsten, they are tightly bounded and highly localized, and thus are hardly affected by neighboring atoms even in solid

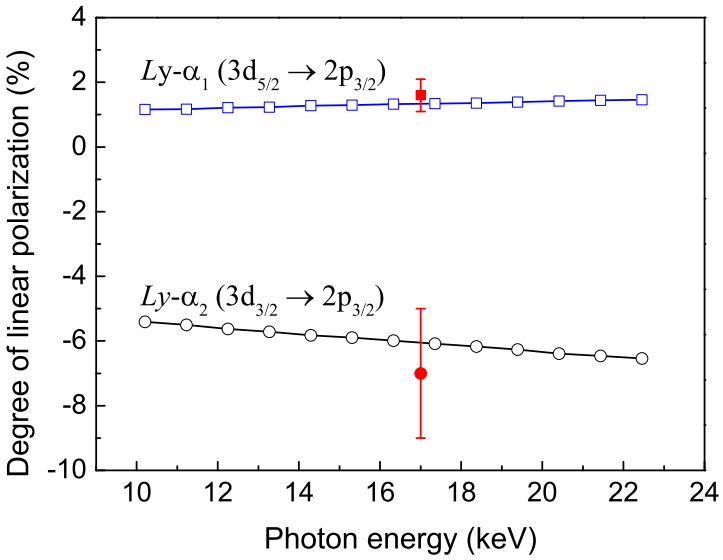

Figure 3.2: The same as Figure 3.1 but together with a comparison with the experimental results measured by a crystal-based spectropolarimeter.

state. Secondly, as already mentioned above, the experimental measurements would not be influenced by the non-monochromaticity of the ionizing light radiation due to the obtained weak dependence of the polarization upon the ionizing photon energy. Thirdly, the use of the crystal-based spectropolarimeter is essential for the successful polarization measurements as the $Ly\text{-}\alpha$ doublet is typically not resolved by solid-state detectors. Moreover, the measurements of fluorescence photon intensities are supervised by the ratio $I(Ly\text{-}\alpha_1)/I(Ly\text{-}\alpha_2)$ that is known with high accuracy since it can be measured very easily with x-ray spectrometers. In the present measurement, the value of such a ratio is determined to be 0.118 ± 0.01, which is in good agreement with other existing results such as 0.114 ± 0.002 in Ref. [73].

As can be seen from Fig. 3.2, experimentally, the linear polarization P_1 is determined to be $+(1.6 \pm 0.5)\%$ for the $Ly\text{-}\alpha_1$ line (solid square) and $-(7.0 \pm 2.0)\%$ for the $Ly\text{-}\alpha_2$ one (solid circle), respectively, which are in good agreement with the theoretical results within the experimental uncertainties. It is important to point out that these experimental data are acquired at the averaged photon energy 18.5 keV, due to the non-monochromaticity of the ionizing light radiation. The detail of determining such an averaged ionizing photon energy can be found in Ref. [70]. Finally, the alignment parameter $\mathcal{A}_{20}$ of the $2p_{3/2}$ hole-state can be readily deduced, respectively, from the measured degrees of linear polarization of the $Ly\text{-}\alpha_{1,2}$ lines.

4 Radiative electron capture of atomic ions: Probing of nuclear parameters

In this chapter, we will explore the angular distribution of x-ray fluorescence photons emitted following radiative electron capture (REC) of highly charged ions with nonzero nuclear spin. As a particular example, we here consider the characteristic $K\alpha_1$ ($1s2p_{3/2}\ ^{1,3}P_{1,2} \rightarrow 1s^2\ ^1S_0$) line emission following the REC into initially hydrogenlike ions. Emphasis is placed especially on the hyperfine interaction of the magnetic moment of the nucleus with those of the ionic electrons and on how this interaction affects the angular properties of the $K\alpha_1$ emission. In the next section, we present a brief review on the studies of the REC of initially hydrogenlike ions and the subsequent radiative decay of the corresponding heliumlike ions. In Sec. 4.2, a theoretical density-matrix description is outlined for the angle-resolved fluorescence photon emission from heliumlike ions with nonzero nuclear spin. To be more specific, we follow our previous work on the linear polarization of the $K\alpha_1$ emission [37] and explain how an effective anisotropy parameter can be defined for the $K\alpha_1$ angular distribution without any need to resolve its individual hyperfine- and fine-structure components. Finally, the effective anisotropy parameter and corresponding angular distribution of the $K\alpha_1$ emission, calculated for selected heliumlike isotopes with different nuclear spin and magnetic dipole moment, are presented and discussed in Sec. 4.3. While a quite sizable effect of the hyperfine interaction on the $K\alpha_1$ angular emission is found for isotopes with nuclear spin $I = 1/2$, such an effect is suppressed for (most) isotopes with nuclear spin $I > 1/2$. We therefore suggest that accurate measurements of the $K\alpha_1$ angular distribution can be used as a tool for probing the nuclear parameters of rare stable and radioactive isotopes with $I \geq 1/2$.

Before proceeding to the next section, here we must state that the main content of this chapter as presented below is based on our published papers [*Phys. Rev. A* **89**, 022513 (2014); **91**, 056502 (2015); *Phys. Scr.* **T166**, 014029 (2015)].

4.1 Radiative electron capture of few-electron ions

In the collisions of highly charged projectile ions with (low-Z) target atoms, one of the most basic processes is the transfer of the atomic electron to the ions [74]. For not

very high collision energies, this process is dominated by the non-radiative electron capture, in which the energy and momentum of the collision system are shared among the projectile ion, the target atom, and the captured electron. However, with the increase of the collision energy T_p, say, roughly at $T_p \gtrsim 10$ MeV/u, the electron capture becomes to be accompanied with a simultaneous emission of a fluorescence photon that carries away the excess energy and momentum [74, 75]. Such a process is usually referred to as the radiative electron capture and, nowadays, it has attracted much attention both theoretically and experimentally. For the collisions between high-Z projectile ions and low-Z target atoms, the REC is nearly identical to the radiative recombination of ions with free electrons, which is the time reversal process of the photoionization [42, 76, 77]. Therefore, the studies on the REC of highly charged heavy ions enable us to explore various different physical effects not only in strong Coulomb fields but also in the radiation (or light) fields.

The experimental studies on the REC process can be performed at the ion storage rings. In the past decades, for instance, the REC of initially bare or singly charged high-Z ions has been intensively investigated at the GSI experimental storage ring (ESR) in Darmstadt [39, 78–81]. Such kind of experiments become more significant nowadays due to the prominent progress in the field of precision x-ray spectroscopy. In fact, the use of efficient x-ray photon detectors enables us not only to determine total REC cross sections but also to study the angle-resolved properties such as the polarization and angular correlation of the simultaneously and subsequently emitted fluorescence photons [39, 76]. When compared with the measurements on total decay rates of these high-Z ions, such angle-resolved studies have been proven to be much more sensitive to the details of various physical effects and interactions and, thus, helped provide new insights into the electron-electron [31, 82] and electron-photon [83–85] interactions in the presence of strong Coulomb fields.

Among those experimental REC studies, in particular, while the observed Ly-α_1 emission following the electron capture into the $2p_{3/2}$ state of (finally) hydrogenlike ions shows a strong anisotropic angular distribution [42], the $K\alpha_1$ fluorescence line from the decay of the $1s2p_{3/2}$ state of heliumlike ions is found to be nearly isotropic [86]. However, such a qualitative difference of the Ly-α_1 and $K\alpha_1$ angular emission behaviors can be readily understood if the $1s2p_{3/2}\ ^{1,3}P_{1,2} \rightarrow 1s^2\ ^1S_0$ fine-structure components of the $K\alpha_1$ line is taken into account. In fact, the tiny anisotropy of the $K\alpha_1$ line is resulted from the opposite angular behavior of the $1s2p_{3/2}\ ^1P_1 \rightarrow 1s^2\ ^1S_0$ electric-dipole (E1) and the $1s2p_{3/2}\ ^3P_2 \rightarrow 1s^2\ ^1S_0$ magnetic-quadrupole (M2) fine-

structure components [87, 88]. From such a rather detailed analysis on this mutual cancelation of the E1 and M2 radiative decay channels with respect to the angular distribution of the $K\alpha_1$ fluorescence emission, valuable knowledge could be revealed on the structure and dynamics of heliumlike ions.

Up to the present, however, most theoretical and experimental studies on characteristic fluorescence photon emissions have just dealt with highly charged ions with zero nuclear spin, $I = 0$, or have simply neglected all contributions caused by such a nonzero spin of the ions considered. Little attention has been paid so far to the effect of the hyperfine interaction for highly charged ions with $I \neq 0$ or to the question of how the nuclear spin affects the fluorescence photon emissions. Early studies on the polarization and angular properties of the fluorescence photons emitted from the ions with $I \neq 0$ were performed, by Dubau and co-workers [36, 89, 90] and, more recently, by Surzhykov *et al.* [37]. In these studies, the hyperfine-induced effects were explored and discussed on the $1s2p_{3/2}\ ^{1,3}P_{1,2} \rightarrow 1s^2\ ^1S_0$ radiative decays of heliumlike ions following either the electron-impact excitation or the REC processes, respectively. To be more specific, the emphasis was placed on their individual hyperfine- or fine-structure-resolved transition components, which have been found to be strongly affected by the magnetic dipole moment μ_I of the ionic nucleus. In the high-Z domain, however, the observation of the individual components is hardly possible due to the relatively small hyperfine splitting of the fine-structure levels as well as the limited energy resolution of modern x-ray photon detectors. Therefore, it is important to explore and thus better understand how the hyperfine interaction affects the emission properties of the overall $K\alpha_1$ fluorescence line consisting of these (yet) unresolved hyperfine- and fine-structure components. For this purpose, in the following section we will present a general theoretical method within the framework of the density matrix theory for studying the $K\alpha_1$ angular distribution following the REC of finally heliumlike ions with nonzero nuclear spin.

4.2 DM description of radiative electron capture and subsequent decay

Let us proceed with considering the following REC and subsequent radiative decay

$$\begin{aligned} A^{(Z-1)+}\ (1s) + e^- &\longrightarrow A^{(Z-2)+}\ (1s2p_{3/2}\ ^{1,3}P_{1,2}) + \gamma_{\rm REC} \\ &\longrightarrow A^{(Z-2)+}\ (1s^2\ ^1S_0) + K\alpha_1 + \gamma_{\rm REC} \end{aligned} \tag{4.1}$$

of initially hydrogenlike (or finally heliumlike) ions with nuclear charge Z. In more detail, an initially hydrogenlike ion $A^{(Z-1)+}$ in its ground state captures a (quasi-)free electron into its subshell $2p_{3/2}$ and simultaneously emits a "recombination" photon γ_{REC}, which leads to the formation of one of the excited fine-structure $1s2p_{3/2}\ ^{1,3}P_{1,2}$ levels of the corresponding heliumlike ion, $A^{(Z-2)+}$. The subsequent radiative decay of these excited levels then gives rise to the so-called fluorescence $K\alpha_1$ emission that is typically observed without resolving the associated fine- and hyperfine-structure components. Actually, the production of the $1s2p_{3/2}\ ^{1,3}P_{1,2}$ levels can be described independently from the subsequent radiative decay of them. Moreover, we assume that the hyperfine interaction is weak enough to be neglected in the REC process but could still be able to perturb the excited $1s2p_{3/2}\ ^{1,3}P_{1,2}$ levels during their radiative decay, and also that the initially hydrogenlike ions and (quasi-)free electrons are not polarized themselves.

4.2.1 Alignment of hyperfine levels following radiative electron capture

The process (4.1) is mostly observed at ion storage rings, and hence the projectile ion beam defines naturally a preferential direction that is chosen as the quantization z axis, with respect to which the excited heliumlike ions could be aligned. Such an alignment depends upon the collision energy of the projectile ions and also upon the detail of the prior electron capture process [42, 81]. As discussed in Subsection 2.2.2, this alignment of the ions describes the non-statistical population of the magnetic substates with different modulus of the projection $|M_{J_i}|$ on the z axis, and is usually characterized by the so-called alignment parameters $\mathcal{A}_{k0}(\alpha_i J_i)$. These parameters describe the formation process of the $\alpha_i J_i$ level and thus enable us to utilize them only to further study the subsequent photon emission without any reference to the detail of the prior REC process, i.e., the first step of the process (4.1).

The production of the excited levels $1s2p_{3/2}\ ^{1,3}P_{1,2}$ of heliumlike ions following the REC of initially hydrogenlike ions has been discussed in great detail within the framework of the density matrix theory [87, 91]. Here, we will therefore recall only the relevant formulae necessary to obtain the alignment parameters of the hyperfine-structure levels and also the effective anisotropy parameters of the $K\alpha_1$ emission for ions with nonzero nuclear spin. Within the density matrix theory [47, 48], the alignment parameter of an atomic (or ionic) level after a particular atomic process

is related to the partial cross sections $\sigma_{|\alpha_i J_i M_i\rangle}$ of populating the magnetic substates $|\alpha_i J_i M_i\rangle$ during this process. For the REC into the $1s2p_{3/2}\ ^{1,3}P_{1,2}$ levels of heliumlike ions, for instance, these alignment parameters can be expressed, respectively, as [91]

$$\mathcal{A}_{20}(^1P_1) = \sqrt{2}\,\frac{\sigma_{|1,\pm1\rangle} - \sigma_{|1,0\rangle}}{2\sigma_{|1,\pm1\rangle} + \sigma_{|1,0\rangle}}\,, \tag{4.2}$$

$$\mathcal{A}_{20}(^3P_2) = -\sqrt{\frac{10}{7}}\,\frac{\sigma_{|2,0\rangle} + \sigma_{|2,\pm1\rangle} - 2\sigma_{|2,\pm2\rangle}}{\sigma_{|2,0\rangle} + 2\sigma_{|2,\pm1\rangle} + 2\sigma_{|2,\pm2\rangle}}\,. \tag{4.3}$$

In the above expressions, $\sigma_{|1,0\rangle}$ and $\sigma_{|1,\pm1\rangle}$ represent the partial REC cross sections of the magnetic substates $M = 0$ and $M = \pm1$ of the $1s2p_{3/2}\ ^1P_1$ level and, moreover, $\sigma_{|2,0\rangle}$, $\sigma_{|2,\pm1\rangle}$ and $\sigma_{|2,\pm2\rangle}$ have similar meanings with respect to the $1s2p_{3/2}\ ^3P_2$ level. For the fine-structure $1s2p_{3/2}\ ^3P_2$ level with total angular momentum $J = 2$, apart from the existing alignment parameter $\mathcal{A}_{20}(^3P_2)$, its alignment should be completely described together by an additional fourth-rank parameter $\mathcal{A}_{40}(^3P_2)$. For the REC of high-Z projectile ions, however, such a fourth-rank parameter is always much smaller than the corresponding second-rank parameter $\mathcal{A}_{20}(^3P_2)$ [87, 91], and thus will be neglected in the following analysis on the angular distribution of the fluorescence $K\alpha_1$ emission.

For the ions with $I \neq 0$, the fine-structure level $\alpha_i J_i$ will further split to corresponding hyperfine-structure levels, say, $(\alpha_i J_i I F_i \equiv)\beta_i F_i$, due to the hyperfine interaction of the nuclear magnetic dipole moment μ_I with those related to the spin and orbital motion of the ionic electrons. If such a hyperfine interaction is considered simply via the I–J coupling but otherwise does not influence the prior REC process, as assumed above, the alignment parameters $\mathcal{A}_{k0}(\beta_i F_i)$ of these hyperfine levels $\beta_i F_i$ can be expressed in terms of the alignment parameter $\mathcal{A}_{k0}(\alpha_i J_i)$ of the corresponding fine-structure level as follows [37, 38],

$$\mathcal{A}_{k0}(\beta_i F_i) = (-1)^{J_i+I+F_i-k}\,[J_i, F_i]^{1/2} \left\{ \begin{array}{ccc} F_i & F_i & k \\ J_i & J_i & I \end{array} \right\} \mathcal{A}_{k0}(\alpha_i J_i)\,. \tag{4.4}$$

Here, $[J_i, F_i] \equiv (2J_i + 1)(2F_i + 1)$ and the standard notation of the Wigner $6j$ symbols is employed. For initially unpolarized projectile ions and (quasi-)free electrons, these alignment parameters fully characterize the respective hyperfine magnetic substate population of the ions and thus can be used further to formulate the angular properties of the subsequent fluorescence photon emissions. Below, we will consider again just the second-order alignment parameter $\mathcal{A}_{20}(\beta_i F_i)$ for the same reason.

4.2.2 Angular distribution of hyperfine-resolved transition lines

To analyze the angular properties of the characteristic $K\alpha_1$ fluorescence emission, we first begin with considering the individual hyperfine-resolved transition component $\beta_i F_i \to \beta_f F_f + \gamma_{\rm hf}$, for which the angular distribution reads as [37, 38]

$$W_{if}(\theta) = \frac{1}{4\pi} \left[1 + \mathcal{A}_{20}(\beta_i F_i)\, f_2(\beta_i F_i, \beta_f F_f)\, P_2(\cos\theta)\right] . \tag{4.5}$$

Here, $P_2(\cos\theta)$ represents the second-order Legendre polynomial, θ is the polar angle of the emitted $\gamma_{\rm hf}$ photon with respect to the quantization z axis, and $f_2(\beta_i F_i, \beta_f F_f)$ denotes the so-called fine-structure function. Such a structure function depends only on the electronic structure of the upper and lower levels of the ions but is independent of the prior REC process; cf. Ref. [47, 91] for more details.

4.2.3 Angular distribution of the $K\alpha_1$ emission line

In most cases, however, neither the individual hyperfine- nor even the fine-structure transition components can be resolved by modern photon detectors with respect to the $K\alpha_1$ fluorescence photons emitted from (high-Z) heliumlike ions. Therefore, in order to compare with experimental results, one then needs to sum (or average) over the angular distribution (4.5) for all the individual hyperfine-structure components to account for their respective contribution to the overall $K\alpha_1$ emission spectra. This summation can be performed coherently or statistically, just depending upon the relative magnitude between the hyperfine splitting of the upper fine-structure level $\alpha_i J_i$ and the natural linewidth of it.

For the $1s2p_{3/2}\ ^1P_1$ level, its hyperfine splitting is much smaller than the linewidth of it for all heliumlike ions with big nuclear magnetic dipole moment μ_I, and thus the individual hyperfine components of the $1s2p_{3/2}\ ^1P_1 \to 1s^2\ ^1S_0$ fine-structure transition should be summed coherently. Such a coherent summation indicates that the considered hyperfine interaction has no influence on the $1s2p_{3/2}\ ^1P_1 \to 1s^2\ ^1S_0$ angular distribution, which means that it remains the same as the one in the case of zero nuclear spin and hence is given by [91]

$$W_{^1P_1}(\theta) = \frac{1}{4\pi} \left[1 + \frac{1}{\sqrt{2}}\, \mathcal{A}_{20}(^1P_1)\, P_2(\cos\theta)\right] . \tag{4.6}$$

In contrast, however, the hyperfine splitting of the $1s2p_{3/2}\ ^3P_2$ level is much larger than its linewidth, and thus the hyperfine components of the $1s2p_{3/2}\ ^3P_2 \to 1s^2\ ^1S_0$

fine-structure transition is summed as follows via a statistical average [37, 38],

$$W_{^3P_2}(\theta) = \frac{\sum_{F_i F_f} N_{if}\, W_{if}(\theta)}{\sum_{F_i F_f} N_{if}}\,. \tag{4.7}$$

Here, the summations over the total (hyperfine) angular momentum quantum numbers $F_{i,\,f}$ take the values $F_{i,\,f} = |I - J_{i,\,f}|, |I - J_{i,\,f}| + 1,\, ...,\, I + J_{i,\,f}$, respectively. Moreover, $N_{if}(\equiv N_{F_i F_f})$ denote the statistical weights of each (individual) hyperfine components to the $\alpha_i J_i \to \alpha_f J_f$ fine-structure transition. For sufficiently short lifetimes of the excited hyperfine levels, in order to ensure that all of the emitted fluorescence photons are indeed recorded by photon detectors, these weight coefficients are given simply by the relative population of the upper levels $\beta_i F_i$. In the following, we assume that these hyperfine levels are populated just by the REC process, and thus, we define $N_{if} = \sigma(\beta_i F_i)/\sum_{F_i} \sigma(\beta_i F_i)$, where $\sigma(\beta_i F_i)$ denotes the known REC cross sections.

Since the respective angular distributions (4.6) and (4.7) of the two fine-structure components have been obtained, one can utilize them to further derive the angular distribution of the overall $K\alpha_1$ emission. Following the similar procedure, such an angular distribution is given by, again, averaging the two components [38],

$$W_{K\alpha_1}(\theta) = N_{^1P_1} W_{^1P_1}(\theta) + N_{^3P_2} W_{^3P_2}(\theta)\,, \tag{4.8}$$

where the statistical weights $N_{^1P_1}$ and $N_{^3P_2}$ are determined from the corresponding total cross sections of populating the upper levels, together with a consideration of their branching ratios of decaying directly to the $1s^2\ ^1S_0$ ground state. As discussed in Subsection 2.4.2, alternatively, the $K\alpha_1$ angular distribution, i.e., Eq. (4.8), can be also parameterized in terms of a single *effective* anisotropy parameter as follows,

$$W_{K\alpha_1}(\theta) = \frac{1}{4\pi}\left[1 + \beta_2^{\rm eff}(K\alpha_1)\, P_2(\cos\theta)\right]\,. \tag{4.9}$$

With this parameterization, the $K\alpha_1$ angular distribution is determined uniquely by the effective anisotropy parameter $\beta_2^{\rm eff}(K\alpha_1)$ and there is no need to resolve the individual hyperfine- or fine-structure transitions.

Equations (4.5)–(4.9) obtained above are general and thus can be used to derive the parameter $\beta_2^{\rm eff}$ for the $K\alpha_1$ emission from any heliumlike ions with either zero or nonzero nuclear spin. By inserting Eqs. (4.5)–(4.7) into Eq. (4.8) and making use of Eq. (4.4), this effective anisotropy parameter can be expressed in terms of the respective anisotropy parameters of the two fine-structure transition lines. For the

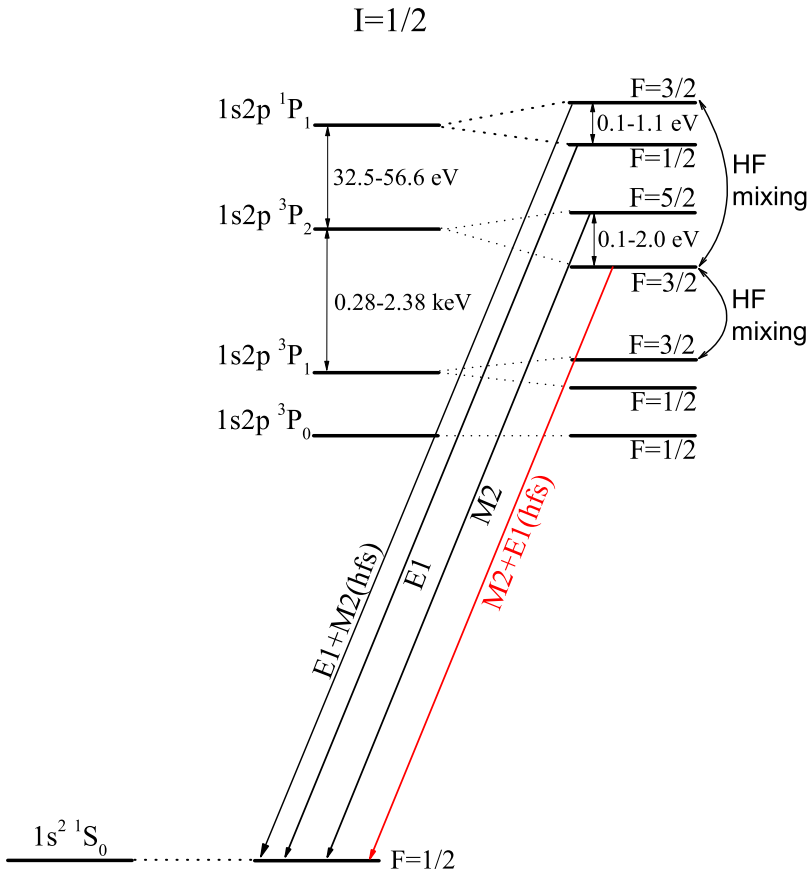

Figure 4.1: Scheme of the low-lying energy levels of heliumlike ions with nuclear spin $I = 1/2$. The energy splittings in the fine- and hyperfine-structure levels are estimated here for the ions with nuclear charge in the range $50 \leq Z \leq 81$.

ions with nuclear spin $I = 1/2$, for instance, it has the following form [92],

$$\beta_2^{\rm eff}(K\alpha_1;\ I=1/2) = \frac{1}{\sqrt{2}}\, N_{^1P_1}\, \mathcal{A}_{20}(^1P_1) \,+\, \frac{2}{5}\sqrt{\frac{7}{5}}\, N_{^3P_2}\, \mathcal{A}_{20}(^3P_2) \times \left(\frac{1}{2\sqrt{2}}\, \frac{a_{E1}^2 + 2\sqrt{3}\, a_{E1}\, a_{M2} - a_{M2}^2}{a_{E1}^2 + a_{M2}^2} - \frac{3\sqrt{2}}{7} \right) . \qquad (4.10)$$

In deriving this expression, we have already made utilization of the short-hand notation $a_{pL} = \left\langle 1s^2\ {}^1S_0,\ F_f = 1/2 \,\|\, H_\gamma(pL) \,\|\, 1s2p_{3/2}\ {}^3P_2,\ F_i = 3/2 \right\rangle$ in order to denote the reduced transition amplitudes for the leading M2 and the hyperfine-induced E1 components of the $1s2p_{3/2}\ {}^3P_2,\ F_i = 3/2 \,\rightarrow\, 1s^2\ {}^1S_0,\ F_f = 1/2$ hyperfine transition as marked by the red line in Figure 4.1 [93]. In more detail, these reduced amplitudes

are introduced by the structure function of the relevant transition. In contrast, for the transition $1s2p_{3/2}\ ^1P_1,\ F_i = 3/2 \rightarrow 1s^2\ ^1S_0,\ F_f = 1/2$, the hyperfine-induced M2 decay channel is much weaker when compared to the leading E1 one and, hence, only the E1 decay is taken into account.

Fig. 4.1 displays a level scheme for the low-lying fine-structure levels and their hyperfine splittings of heliumlike ions with nuclear spin $I = 1/2$. The energy splittings as given in this figure are roughly estimated for the ions with nuclear charge in the range $50 \leq Z \leq 81$. Apart from the $1s2p_{3/2}\ ^3P_2,\ F_i = 3/2 \rightarrow 1s^2\ ^1S_0,\ F_f = 1/2$ transition as discussed above, for other hyperfine components only one dominant decay channel is considered and thus their structure functions become a 'geometrical' constant, independent of the particular transition amplitudes [37, 91]. Due to this reason, only the two reduced amplitudes a_{E1} and a_{M2} occur explicitly in Eq. (4.10). For heliumlike ions with $I = 0$, in contrast, there is no hyperfine splitting and, thus, the corresponding effective anisotropy parameter follows directly from averaging over the two fine-structure components [91],

$$\beta_2^{\rm eff}(K\alpha_1;\ I=0) = \frac{1}{\sqrt{2}}\, N_{^1P_1}\, \mathcal{A}_{20}(^1P_1) - \sqrt{\frac{5}{14}}\, N_{^3P_2}\, \mathcal{A}_{20}(^3P_2)\,. \tag{4.11}$$

This anisotropy parameter purely depends on the weight coefficients and the alignment parameters of the $1s2p_{3/2}\ ^{1,3}P_{1,2}$ levels, independent of any nuclear parameters and the associated transition amplitudes.

4.2.4 Evaluation of hyperfine transition amplitudes

As can be seen clearly from Eq. (4.10), any further analysis on the effective anisotropy parameter $\beta_2^{\rm eff}(K\alpha_1, I = 1/2)$ will be traced back to the computations of the reduced hyperfine transition amplitudes $\langle \beta_f F_f \,\|H_\gamma(pL)\|\, \beta_i F_i\rangle$. In order to compute these reduced matrix elements, one needs first to solve the following secular equation,

$$(\hat{H}_0 + \hat{H}_{\rm hfs})\ |\beta F M_F\rangle = E_{\beta F}\ |\beta F M_F\rangle\ . \tag{4.12}$$

Here, $|\beta F M_F\rangle$ represents the (hyperfine) eigen wave function with the corresponding eigen energy $E_{\beta F}$. Moreover, $\hat{H}_0$ and $\hat{H}_{\rm hfs}$ denote the electronic Hamiltonian and the hyperfine interaction Hamiltonian, respectively. The latter has the following general representation,

$$\hat{H}_{\rm hfs} = \sum_{k\geq 1} T^{(k)} \cdot M^{(k)}\,, \tag{4.13}$$

where $T^{(k)}$ and $M^{(k)}$ denote the k-order spherical tensor operators of the electronic and nuclear parts, respectively. If we consider only the dominant nuclear magnetic dipole interaction, as done in the following, Eq. (4.13) will be simplified as

$$\hat{H}_{\rm hfs} = T^{(1)} \cdot M^{(1)} \,. \tag{4.14}$$

Assuming that we have already solved Eq. (4.12) for only the electronic Hamiltonian $\hat{H}_0$ corresponding to atomic fine-structure energy eigenstates, the corresponding hyperfine states can be written as a linear combination of the basis states constructed as a product of the electronic $|\alpha J M_J\rangle$ and the nuclear $|I M_I\rangle$ states,

$$\begin{aligned} |\beta F M_F\rangle &= \sum_{\alpha J} C^F_{\alpha J} \, |\alpha J I : F M_F\rangle \\ &= \sum_{\alpha J} \sum_{M_I M_J} C^F_{\alpha J} \, \langle I M_I J M_J \,|\, F M_F\rangle \, |I M_I\rangle \, |\alpha J M_J\rangle \,. \end{aligned} \tag{4.15}$$

By inserting this ansatz into Eq. (4.12) and then projecting it upon some particular basis states, we find that the hyperfine mixing coefficients $C^F_{\alpha J}$ satisfy the following eigenvalue equation,

$$E_{\beta F} \, C^F_{\alpha J} = \sum_{\alpha' J'} \left(E_{\alpha J} \delta_{\alpha \alpha'} \delta_{J J'} + W^F_{\alpha J, \, \alpha' J'} \right) \, C^F_{\alpha' J'} \,. \tag{4.16}$$

Here, $E_{\alpha J}$ represents the eigen energy of the corresponding fine-structure level αJ. Moreover, the interaction matrix elements $W^F_{\alpha J, \, \alpha' J'}$ are given as follows in terms of the (reduced) electronic and the nuclear matrix elements,

$$W^F_{\alpha J, \, \alpha' J'} = (-1)^{I+J+F} \left\{ \begin{array}{ccc} I & J & F \\ J' & I & 1 \end{array} \right\} \left\langle \alpha J \left\| T^{(1)} \right\| \alpha' J' \right\rangle \left\langle I \left\| M^{(1)} \right\| I \right\rangle \,. \tag{4.17}$$

While a proper representation of the atomic state vectors is required in order to calculate the (reduced) electronic amplitudes $\left\langle \alpha J \left\| T^{(1)} \right\| \alpha' J' \right\rangle$ [68, 94], the nuclear amplitudes are simply given by

$$\langle I \| M^{(1)} \| I \rangle = \mu_I \sqrt{(2I+1)(I+1)/I} \,, \tag{4.18}$$

in terms of the nuclear magnetic dipole moment μ_I and the spin I of the particular ions under consideration.

As seen clearly from Eqs. (4.16)–(4.18), the nuclear magnetic dipole moment μ_I enters into the (hyperfine) mixing coefficients $C^F_{\alpha J}$. Since these coefficients have been used to express the hyperfine-structure eigenstates $|\beta F M_F\rangle$ as given by Eq. (4.15),

very naturally, the magnetic moment μ_I also enters into the following reduced hyperfine radiative transition amplitudes [37, 38],

$$\langle \beta_f F_f \,\|\, H_\gamma(pL) \,\|\, \beta_i F_i \rangle = \sum_{\alpha_i J_i} \sum_{\alpha_f J_f} C^{F_i}_{\alpha_i J_i}\, C^{F_f}_{\alpha_f J_f}\, [F_i, F_f]^{1/2}\, (-1)^{J_i + I + F_f + L} \times \left\{ \begin{array}{ccc} F_i & F_f & L \\ J_f & J_i & I \end{array} \right\} \langle \alpha_f J_f \,\|\, H_\gamma(pL) \,\|\, \alpha_i J_i \rangle \ . \qquad (4.19)$$

In order to compute these reduced amplitudes for the particular hyperfine-resolved transitions of interest, as discussed in Sec. 2.5, we use the GRASP92 code [66] based on the MCDF method to generate the necessary wave functions and then use the RATIP code [68] to calculate the required hyperfine mixing coefficients and the fine-structure reduced amplitudes. Moreover, the (partial) REC cross sections and thus the alignment parameters are calculated also with the use of the RATIP package.

4.3 Results and discussion

At present, we are ready to employ Eqs. (4.2)–(4.11) to study the angular properties of the characteristic $K\alpha_1$ fluorescence emission following the REC into the excited $1s2p_{3/2}\ ^{1,3}P_{1,2}$ levels of finally heliumlike ions. For isotopes with nuclear spin $I \geq 1/2$, the $K\alpha_1$ angular emission of the corresponding ions appears to be rather different when compared to other isotopes of the same elements but with zero nuclear spin. Apart from the fine and hyperfine structure of the ions themselves, naturally, the $K\alpha_1$ angular emission also depends upon the details of the prior excitation process. In the following, we shall consider the radiative decay of heliumlike ions following the REC into initially hydrogenlike projectile ions with kinetic energies of roughly $T_p = 10 - 200$ MeV/u. Such high energies are quite typical in the collisions of high-Z projectiles with light gas targets, and have been performed before, for instance, at ion storage rings. For these energies of the projectile ions, the alignment parameters $\mathcal{A}_{20}$ as given by Eqs. (4.2)–(4.3) have been studied at several places [87, 91]. Below, we will analyze and discuss in great detail the effects of the hyperfine interaction on the angular emission properties of the overall $K\alpha_1$ fluorescence line.

4.3.1 Ions with nuclear spin $I = 1/2$

For the excited fine-structure $1s2p_{3/2}\ ^{1,3}P_{1,2}$ levels of heliumlike ions with a nonzero initial alignment, an extremely weak anisotropic angular distribution has been known

well for the associated characteristic $K\alpha_1$ fluorescence emission. Here, however, we are mainly interested in the modifications to the angular distribution of the overall $K\alpha_1$ emission for the isotopes with nonzero nuclear spin and sizable magnetic dipole moment owing to the hyperfine interaction. For this reason, Figure 4.2 displays the calculated effective anisotropy parameter $\beta_2^{\rm eff}$ for the overall $K\alpha_1$ emission following the REC into initially hydrogenlike ions, as functions of the nuclear magnetic dipole moment [92]. All the anisotropy parameters plotted in this figure are calculated at a projectile energy of $T_p = 50$ MeV/u. Results are shown for isotopes with nuclear spin $I = 0$ (shadowed area) as well as for selected tin isotopes ${}^{A}_{50}\mathrm{Sn}^{48+}$ ($A = 119$, 113, 121; black points), xenon isotopes ${}^{A}_{54}\mathrm{Xe}^{52+}$ ($A = 129$, 127, 125, 123; red squares), and thallium isotopes ${}^{A}_{81}\mathrm{Tl}^{79+}$ ($A = 187$, 205, 207; blue triangles) [95], all of which have nuclear spin $I = 1/2$. While the effective anisotropy parameter $\beta_2^{\rm eff}(K\alpha_1;\, I = 0)$ in

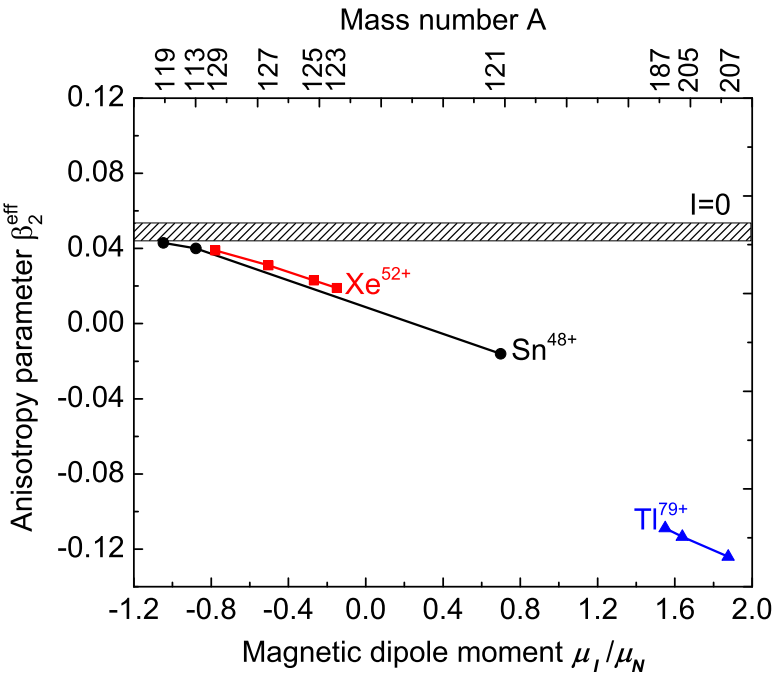

Figure 4.2: Effective anisotropy parameters $\beta_2^{\rm eff}$ of the characteristic $K\alpha_1$ emission as functions of the magnetic dipole moment μ_I following the REC into the two excited $1s2p_{3/2}\ {}^{1,3}P_{1,2}$ levels of (finally) heliumlike projectile ions with a kinetic energy of $T_p = 50$ MeV/u. Results are shown for the ions ${}^{A}_{50}\mathrm{Sn}^{48+}$ ($A = 119$, 113, 121; black points), ${}^{A}_{54}\mathrm{Xe}^{52+}$ ($A = 129$, 127, 125, 123; red squares) and ${}^{A}_{81}\mathrm{Tl}^{79+}$ ($A = 187$, 205, 207; blue triangles) as well as their zero-spin counterparts (shadowed area), respectively. Lines are drawn just to guide the eyes.

the case of zero nuclear spin remains nearly the same for all given medium- and high-Z elements, the anisotropy parameter $\beta_2^{\rm eff}(K\alpha_1;\, I = 1/2)$ changes roughly linearly with the magnetic dipole moment μ_I of the isotopes. The sign and particular values of the $\beta_2^{\rm eff}$ parameter hereby depend on the alignment parameters of the two fine-structure levels as well as on the mixing of the hyperfine-induced E1 with the leading M2 amplitudes in the hyperfine-resolved $1s2p_{3/2}\ ^3P_2,\ F_i = 3/2 \rightarrow 1s^2\ ^1S_0,\ F_f = 1/2$ transition.

For instance, if we have a look at the tin isotope $^{121}_{50}\mathrm{Sn}^{48+}$ with a nuclear magnetic dipole moment $\mu_I = +0.698\ \mu_N$, the corresponding anisotropy parameter $\beta_2^{\rm eff}(K\alpha_1)$ changes from 0.046 to -0.016, when compared to other tin isotopes with zero spin. Such a sizable change of the effective anisotropy parameter $\beta_2^{\rm eff}$ can be readily measured with the present-day detection techniques [39, 86]. For thallium, moreover, all of its spin-1/2 isotopes have large positive magnetic dipole moments, as tabulated in Reference [95], which give rise to a sizable negative effective anisotropy. A similar increase or decrease in the effective anisotropy parameter $\beta_2^{\rm eff}(K\alpha_1;\, I = 1/2)$ occurs also for other (nuclear) spin-1/2 ions, depending on the particular sign and magnitude of their magnetic dipole moment μ_I.

Up to the present, we have discussed the effective anisotropy parameter $\beta_2^{\rm eff}$ only for the kinetic energy $T_p = 50$ MeV/u of the projectile ions when colliding with a (light) gas target. For other projectile collision energies, naturally, this parameter will become different due to the change of the initial alignments of the excited fine- or hyperfine-structure levels. In order to much better understand the corresponding modifications to the overall $K\alpha_1$ anisotropy, Figure 4.3 displays the effective anisotropy parameter $\beta_2^{\rm eff}(K\alpha_1)$ as functions of the projectile energy. Results are shown for the two ions $^{119}_{50}\mathrm{Sn}^{48+}(I = 1/2,\ \mu_I = -1.047\ \mu_N$; left panel) and $^{207}_{81}\mathrm{Tl}^{79+}(I = 1/2,\ \mu_I = +1.876\ \mu_N$; right panel), respectively. Again, detailed calculations for these two spin-1/2 isotopes (black solid lines) with the magnetic moments μ_I of different sign are compared with those for the corresponding zero-spin isotopes of the same elements (blue dashed lines). As can be seen from this figure, a sizable but opposite shift in the anisotropy parameter $\beta_2^{\rm eff}(K\alpha_1)$ is observed for the two isotopes. For the thallium isotope $^{207}_{81}\mathrm{Tl}^{79+}$, for instance, the effective anisotropy parameter $\beta_2^{\rm eff}(K\alpha_1;\, I = 1/2)$ is always negative at all of the given projectile energies due to its large and positive magnetic dipole moment $\mu_I = +1.876\,\mu_N$, in contrast to the corresponding anisotropy parameter $\beta_2^{\rm eff}(K\alpha_1;\, I = 0)$ for its zero-spin counterpart. Moreover, the biggest effect of the hyperfine interaction is usually observed

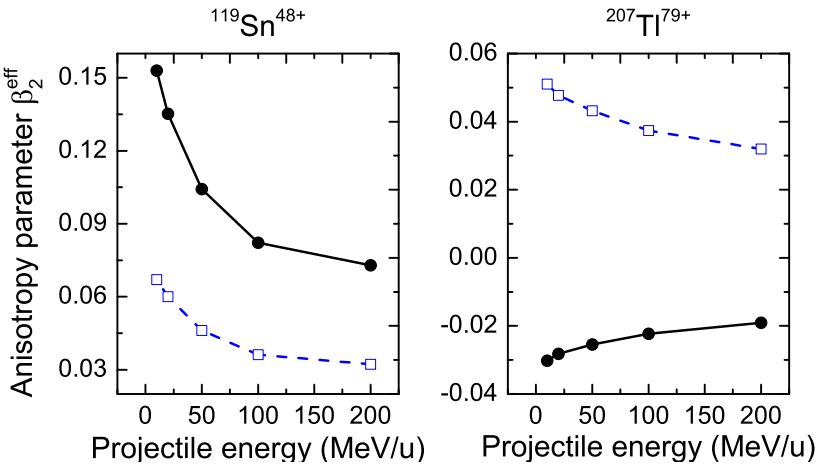

Figure 4.3: Effective anisotropy parameter β_2^{eff} of the characteristic $K\alpha_1$ emission as functions of the projectile energy T_p following the REC into the excited $1s2p_{3/2}\ ^{1,3}P_{1,2}$ levels of (finally) heliumlike ions. Results are shown for the ions $^{119}_{50}\text{Sn}^{48+}$ ($I = 1/2$, $\mu_I = -1.047\,\mu_N$; left panel) and $^{207}_{81}\text{Tl}^{79+}$ ($I = 1/2$, $\mu_I = +1.876\,\mu_N$; right panel), respectively. Computations for the two spin-1/2 ions (black solid lines) are compared with those for the corresponding zero-spin ions (blue dashed lines).

for low projectile energies, at which the prior REC process gives rise to the strongest initial alignments for the excited fine-structure $1s2p_{3/2}\ ^{1,3}P_{1,2}$ levels and, hence, also leads to a large effective anisotropy parameter.

The (more or less) large difference of the effective anisotropy parameter $\beta_2^{\text{eff}}(K\alpha_1)$ for zero-spin and spin-1/2 isotopes of the same element makes the measurements on the $K\alpha_1$ angular distribution become a sensitive tool for determining nuclear parameters such as the nuclear spin I and magnetic dipole moment μ_I via their influences upon the overall $K\alpha_1$ fluorescence emission. For this reason, Figure 4.4 displays the associated $K\alpha_1$ angular distribution calculated at a low projectile collision energy of $T_p = 10$ MeV/u for the same two isotopes $^{119}_{50}\text{Sn}^{48+}$ and $^{207}_{81}\text{Tl}^{79+}$ as discussed in Figure 4.3. Once again, the results for these two spin-1/2 ions (black solid lines) are compared with those for their zero-spin counterparts (blue dashed lines). Obviously, the remarkable change of the $K\alpha_1$ angular distribution in the case of the $^{207}_{81}\text{Tl}^{79+}$ ion (right panel) results again from the change of the sign of the associated anisotropy parameter $\beta_2^{\text{eff}}(K\alpha_1)$ as discussed above. To the best of our knowledge, this is the first case in the physics of high-Z ions in which the hyperfine interaction results in a qualitatively different angular behavior of the emitted characteristic x-ray fluorescence photons, compared to what one would expect for the corresponding zero-spin

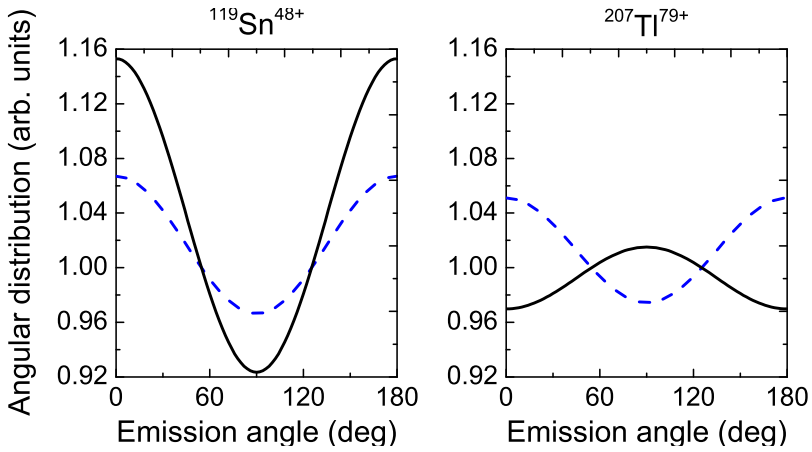

Figure 4.4: Angular distribution of the $K\alpha_1$ characteristic emission following the REC into the excited $1s2p_{3/2}$ $^{1,3}P_{1,2}$ levels of (finally) helium-like ions. Results for the spin-1/2 isotopes from Fig. 4.3 (black solid lines) are compared with computations for zero-spin isotopes (blue dashed lines) of the same element. All calculations were performed within the projectile frame and for projectile ions with kinetic energy $T_p = 10$ MeV/u.

isotopes with rich natural abundances. Until now, we have only discussed the $K\alpha_1$ angular distribution for heliumlike spin-1/2 ions together with the corresponding zero-spin ions for the sake of facilitating a comparison. Among all of the (rare) stable and radioactive isotopes, however, most of them have the nuclear spin $I > 1/2$. In the following subsection, we shall study the effect of the hyperfine interaction on the $K\alpha_1$ angular distribution for this category of isotopes.

4.3.2 Ions with nuclear spin $I > 1/2$

Compared to the spin-1/2 ions which have just a hyperfine doublet for each of their fine-structure levels with $J \neq 0$, the ions with nuclear spin $I > 1/2$ have more hyperfine-structure levels or splittings. For the $K\alpha_1$ radiative decay of the upper $1s2p_{3/2}$ $^3P_2$ level, especially, the hyperfine-induced mixing of the fine-structure $1s2p_{3/2}$ $^3P_2$ level with the $1s2p_{3/2}$ $^1P_1$ (or other) fine-structure levels leads to the E1 admixture to the $1s2p_{3/2}$ $^3P_2 \rightarrow 1s^2$ $^1S_0$ transition that affects significantly the M2 emission behavior of this fine-structure transition itself. For other ions with nuclear spin $I > 1/2$, a similar E1-M2 multipole mixing also occurs but with much less influences upon the overall $K\alpha_1$ fluorescence emissions owing to the reduced statistical weights of those (single) hyperfine transitions with such a mixing involved. Generally, each of the fine-structure levels splits into the hyperfine levels $|J-I|$, $|J-$

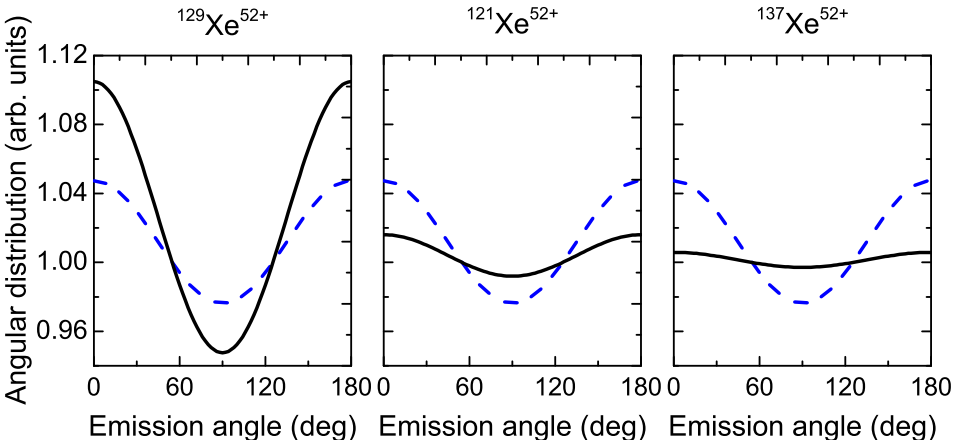

Figure 4.5: The same as Figure 4.4 but for the projectile energy $T_p = 50$ MeV/u and for three different xenon isotopes with nuclear spin $I \geq 1/2$ and comparable magnetic dipole moment μ_I: $^{129}_{54}\mathrm{Xe}^{52+}$ ($I = 1/2$, $\mu_I = -0.778\,\mu_N$; left panel), $^{121}_{54}\mathrm{Xe}^{52+}$ ($I = 5/2$, $\mu_I = -0.701\,\mu_N$; middle panel), and $^{137}_{54}\mathrm{Xe}^{52+}$ ($I = 7/2$, $\mu_I = -0.968\,\mu_N$; right panel).

$I|+1$, ..., $J+I$, among which only two or three (hyperfine-resolved) transitions may benefit from this significant E1-M2 mixing. As a consequence, such an effect of the hyperfine interaction will be weakened as the nuclear spin I increases. This can be clearly seen from Fig. 4.5, in which we compare the angular distributions of the overall $K\alpha_1$ fluorescence emission for different xenon ions with nuclear spin $I = 1/2$, 5/2 and 7/2, respectively. To facilitate such a comparison, we here have chosen the three isotopes with a comparable (negative) magnetic moment.

From the above discussion we conclude that a quite sizable effect of the hyperfine interaction on the $K\alpha_1$ angular emission is found for heliumlike ions with nuclear spin $I = 1/2$, while this effect is remarkably suppressed for (most) ions with the nuclear spin $I > 1/2$. Therefore, we suggest that accurate experimental measurements on the $K\alpha_1$ angular distribution at ion storage rings might be used as an independent tool for determining the nuclear parameters of stable or radioactive isotopes with nonzero nuclear spin.

5 Two-step radiative cascades via overlapping resonances: Identification of level splitting of ions

In this chapter, we shall study the photon polarization and angular distribution as well as the photon-photon angular correlation for the characteristic fluorescence photon emissions from two-step radiative cascades proceeding via intermediate overlapping resonances. Such a study is motivated by the following two questions: (i) how the level splitting of these overlapping resonances affects the emitted fluorescence photons; (ii) whether or not experimental measurements on the photon polarization or angular correlation can help resolve tiny level splittings in highly charged ions, if analyzed along their isoelectronic sequences. In the next section, we will very briefly discuss the current status of studies on radiative or non-radiative decays of atoms or ions that are associated with their overlapping resonances. In order to explore the two questions, a density-matrix formalism is developed in Section 5.2 to describe the two-step radiative cascades that proceeds via overlapping atomic resonances. While the obtained formalism is general, we here apply it to a particular radiative cascade $1s2p^2\ J_i = 1/2,\, 3/2 \rightarrow 1s2s2p\ J = 1/2,\, 3/2 + \gamma_1 \rightarrow 1s^2 2s\ J_f = 1/2 + \gamma_1 + \gamma_2$ of lithiumlike ions, for which a level crossing between the two intermediate resonances $1s2s2p\ J = 1/2,\, 3/2$ occurs among $74 \leq Z \leq 79$. In Sec. 5.3, finally, the obtained γ_2 polarization and angular distribution as well as the γ_1–γ_2 angular correlation are presented and discussed. From this discussion, we therefore suggest that accurate polarization or angle-resolved measurements on characteristic fluorescence photon emissions may serve as an independent tool for determining tiny level splittings in excited highly charged ions.

The main content of this chapter as presented below is based on our published papers [*Phys. Rev. A* **90**, 052515 (2014); *J. Phys.: Conf. Ser.* **635**, 012020 (2015)].

5.1 Radiative decays via overlapping resonances

As discussed above, characteristic x-ray emissions from excited atoms or ions have attracted a lot of attention over the past decades [96–99]. In addition, the angular

distribution and polarization of the x-rays were also studied extensively, due to their sensitivity with regard to various (relatively weak) atomic effects or interactions [30, 38, 39]. Up to the present, however, almost all of these studies were performed for the x-ray photons that are emitted from well isolated (fine-structure) energy levels. In contrast, little attention was paid so far to those emitted from the radiative decays or cascades proceeding via two (or even more) overlapping atomic resonances. When compared to well isolated energy levels, x-ray fluorescence emissions from these overlapping resonances are influenced also by spin-spin and spin-orbit interactions that may lead to a (more or less) depolarization of these (intermediate) resonances due to their finite lifetimes. A polarization of the intermediate resonances usually occurs if the initial resonance of a two-step radiative cascade is polarized, for instance, in the processes of resonant electron capture or electron impact excitation. If no further details are known on the exact time interval between the two sequential radiative decay processes of the cascade, this depolarization can be characterized by a so-called depolarization factor, which just depends on the splitting and respective linewidths of the intermediate resonances [69, 100, 101]. Such an effect of (partially) overlapping atomic resonances on the emission of electrons or photons is usually called lifetime-induced depolarization.

Most work on such a depolarization effect was performed so far just for angular distributions of electron as well as for electron-electron angular correlations in the photoionization of atoms by strong light fields [101–103] or in the non-radiative decay of inner-shell excited atoms and ions [57, 104, 105]. In the two-photon double ionization process, however, the depolarization factor will depend not only upon the (natural) linewidths and the splitting of the coherently excited overlapping resonances but also upon the duration of laser pulses [101]. For the two-step radiative cascades via overlapping resonances, in contrast, the lifetime-induced depolarization is described merely by the linewidths and the splitting of these resonances. We therefore expect that the polarization and angular behaviors of the associated fluorescence photons may be affected by the splitting for given linewidths and that this effect on the fluorescence photons might be measurable near to the crossing point of the resonances along a given isoelectronic sequence. To further explore this, in the following section we will present a general density-matrix formalism for studying photon emission behaviors in the two-step radiative cascades proceeding via overlapping intermediate resonances.

5.2 DM description of two-step radiative cascades

Let us start with considering the following two-step radiative decay cascade

$$A^{q+**}(\alpha_i J_i) \longrightarrow \gamma_1 + \left\{ \begin{array}{c} A^{q+*}(\alpha J) \\ A^{q+*}(\alpha' J') \end{array} \right\} \longrightarrow \gamma_1 + \gamma_2 + A^{q+}(\alpha_f J_f)\,, \qquad (5.1)$$

where a q-fold charged ion A^{q+**} is assumed to be initially in a doubly excited level as denoted by $\alpha_i J_i$. In the first step of this cascade, the two intermediate overlapping resonances αJ and $\alpha' J'$ are produced coherently due to the γ_1 photon emission. Subsequently, the second-step radiative decay starting from the overlapping resonances brings the ion to its ground level $\alpha_f J_f$ together with the γ_2 photon emission, as shown schematically also in Fig. 5.1 [100]. Here, while J's denote total angular momenta of the corresponding levels, α's refer to all other quantum numbers that are required for a unique specification of these levels.

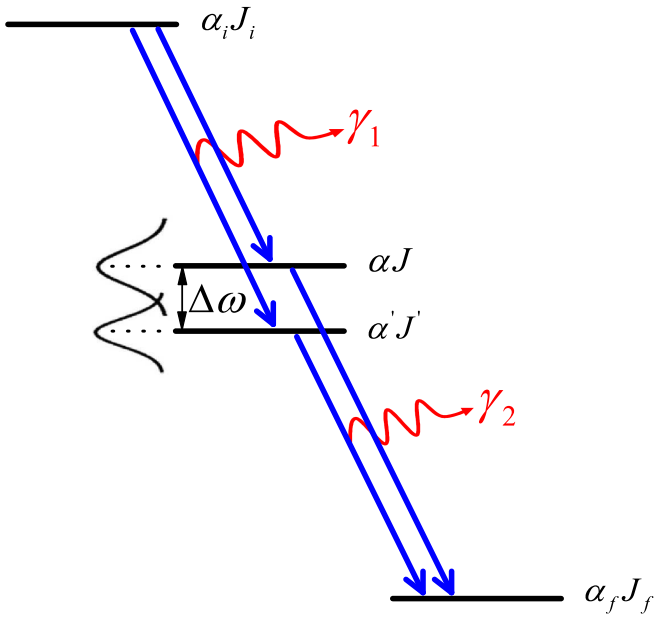

Figure 5.1: Level scheme of the two-step radiative cascade (5.1). The ion that is assumed to be initially in the doubly excited level $\alpha_i J_i$ decays radiatively to the ground level $\alpha_f J_f$ via the two intermediate overlapping resonances αJ and $\alpha' J'$. While the γ_1 and γ_2 photons can be distinguished energetically, no further line structure could be resolved individually due to (partial) overlap of the αJ and $\alpha' J'$ resonances.

5.2.1 Angular correlation of the two-step photons

In studying x-ray emissions from atoms or ions, the formation and subsequent decay of excited states are often described independently, cf. Refs. [106–108]. Therefore, not much need to be discussed on the prior excitation process, and here we just begin our analysis of the process (5.1) simply with the statistical tensors $\rho_{k_i q_i}(\alpha_i J_i)$ of the initial $\alpha_i J_i$ level. This set of statistical tensors fully characterizes the polarization state of the level produced in some particular collision processes and, thus, affects certainly the angular and polarization properties of the subsequent fluorescence photon emissions. In this subsection, we explain very briefly how the angular correlation of the emitted photons can be expressed in terms of these tensors and the associated radiative transition amplitudes without going into the details of its derivation.

In contrast to other decay cascade processes that proceed via well isolated energy levels, the main difference in dealing with overlapping resonances arises from their statistical tensors $\rho^{ion}_{kq}(\alpha J, \alpha' J'; t)$. These statistical tensors evolve with time in terms of $\sim \exp[(i\omega_{\alpha J,\alpha' J'} - \Gamma_{\alpha J,\alpha' J'})t]$ owing to the spin-orbit interaction in the ion [101–103]. In the vector model of angular momenta, this evolution can be also understood as a precession of total angular momentum of the ion around the quantization axis during the time interval between the γ_1 and γ_2 photon emissions. However, since nothing is known about the exact time interval between the two-step photon emissions, one needs to average the tensors $\rho^{ion}_{kq}(\alpha J, \alpha' J'; t)$ over time. Such a time average gives rise to the so-called depolarization factor and thus naturally to time-averaged statistical tensors of the intermediate resonances. Once the time-averaged statistical tensors are obtained, the polarization and angular correlation of the emitted characteristic photons can be further derived in the light of the density matrix theory. For instance, the γ_1–γ_2 angular correlation is described by the following correlation function [100],

$$
\begin{aligned}
W(\theta_1, \varphi_1;\, \theta_2, \varphi_2) = & \sum_{k_i q_i\, \bar{k}\bar{q}\, kq} \sum_{\alpha J\, \alpha' J'} \sum_{\bar{p}\bar{L}\bar{p}'\bar{L}' pLp'L'} 4\pi\, \rho_{k_i q_i}(\alpha_i J_i)\, \bar{M}_{\bar{p}\bar{L}}\, \bar{M}^*_{\bar{p}'\bar{L}'}\, M_{pL}\, M^*_{p'L'} \\
& \times (-1)^{L'+J+J_f+k} \left\langle kq, \bar{k}\bar{q} \,|\, k_i q_i \right\rangle \left\{ \begin{array}{ccc} J' & L' & J_f \\ L & J & k \end{array} \right\} \left\{ \begin{array}{ccc} J & \bar{L} & J_i \\ J' & \bar{L}' & J_i \\ k & \bar{k} & k_i \end{array} \right\} \\
& \times \varepsilon^{\mathrm{det}^*}_{\bar{k}0}(\bar{p}\bar{L}, \bar{p}'\bar{L}')\, \varepsilon^{\mathrm{det}^*}_{k0}(pL, p'L')\, h_{\alpha J,\alpha' J'}\, Y_{\bar{k}\bar{q}}(\theta_1, \varphi_1)\, Y_{kq}(\theta_2, \varphi_2)\,. \qquad (5.2)
\end{aligned}
$$

In this expression, Y_{kq} denotes the spherical harmonics, and the short-hand notations

$\bar{M}_{\bar{p}\bar{L}} \equiv \langle \alpha J \left\| H_{\gamma_1}(\bar{p}\bar{L}) \right\| \alpha_i J_i \rangle$ and $M_{pL} \equiv \langle \alpha_f J_f \| H_{\gamma_2}(pL) \| \alpha J \rangle$ are used to represent the reduced transition amplitudes for the first- and second-step decays, respectively, in which individual photons are characterized by their multipolarity pL with $p = 0$ for the electric multipoles and with $p = 1$ for the magnetic ones. Moreover, there are two further entities in the correlation function (5.2). One of them is the tensors $\varepsilon^{\rm det}_{k0}(pL, p'L')$, which are introduced here to account for the efficiency of detectors for observing the individual photons with multipolarities pL and $p'L'$. In the (so-called) *photon frame* [47], they have their simplest form as follows [47],

$$\varepsilon^{\rm det}_{k0}(pL, p'L') = (-1)^{L'-1} \frac{\hat{L}\hat{L}'}{16\pi} \langle L1, L'-1 \,|\, k0 \rangle \, [1 + (-1)^f] \tag{5.3}$$

where $f = L+p+L'+p'-k$ and $\hat{L} \equiv (2L+1)^{1/2}$. Another entity is the depolarization factor of the (partially) overlapping intermediate resonances αJ and $\alpha' J'$, as already discussed above, which is the consequence of the performed time-average procedure and, finally, is expressed in terms of the energy splitting (or difference) $\omega_{\alpha J, \alpha' J'}$ and the overall natural linewidths $\Gamma_{\alpha J, \alpha' J'}$ of the intermediate resonances [47],

$$h_{\alpha J, \alpha' J'} = \frac{\Gamma_{\alpha J, \alpha' J'} - i\omega_{\alpha J, \alpha' J'}}{\Gamma^2_{\alpha J, \alpha' J'} + \omega^2_{\alpha J, \alpha' J'}} \,. \tag{5.4}$$

To be more specific, $\omega_{\alpha J, \alpha' J'} = E_{\alpha J} - E_{\alpha' J'}$ and $\Gamma_{\alpha J, \alpha' J'} = \frac{1}{2}(\Gamma_{\alpha J} + \Gamma_{\alpha' J'})$, with the energy $E_{\alpha J}$ and linewidth $\Gamma_{\alpha J}$ corresponding to the level αJ, respectively.

A complete set of the depolarization factor forms a Hermitian matrix in which the diagonal matrix elements denote the incoherent contribution of the resonances and the non-diagonal ones represent the coherent superposition of them. This superposition arises from the fact that the 'decay pathes' via the intermediate resonances in the radiative cascade are spectrally indistinguishable. If the splitting of the resonances is much larger than their widths, i.e., $\omega_{\alpha J, \alpha' J'} \gg \Gamma_{\alpha J, \alpha' J'}$, the non-diagonal matrix elements vanish and only the ones with $J = J'$ contribute to the cascade. This corresponds to the decay behavior as expected for two (or even more) isolated resonances, in which the overall emission is obtained just as an incoherent sum over all individual decay paths. In contrast, if the level splitting is negligible when compared to the overall width, i.e., $\omega_{\alpha J, \alpha' J'} \ll \Gamma_{\alpha J, \alpha' J'}$, for instance, for the (partially) overlapping resonances of atoms or ions, the non-diagonal matrix elements will be very important. In this case, the precession of the total angular momentum of each resonance will always depolarize the resonances, as determined from the non-diagonal elements of the time-dependent statistical tensors for $J \neq J'$ [101].

5.2.2 Angular distribution of the second-step photons

Besides observing the γ_1–γ_2 angular correlation in coincidence under different emission angles, it is usually much easier just to measure the angular distribution for one of the two characteristic fluorescence photons. For this purpose, the photon-photon angular correlation function (5.2) is used to derive the angular distribution of either photon by simply integrating it over the emission angles (θ_u, φ_u) of the other unobserved one. For the angular distribution of the second-step fluorescence γ_2 photon, for instance, we then obtain [100]

$$
\begin{aligned}
W(\theta_2, \varphi_2) = \sum_{k_i q_i} \sum_{\alpha J,\, \alpha' J'} \sum_{\bar{p}\bar{L}\bar{p}'\bar{L}' p L p' L'} & \rho_{k_i q_i}(\alpha_i J_i)\, \hat{k_i}^{-1}\, \bar{M}_{\bar{p}\bar{L}}\, \bar{M}^*_{\bar{p}'\bar{L}'}\, M_{pL}\, M^*_{p'L'} \\
& \times (-1)^{L'+J+J_f+J_i+J+\bar{L}} \left\{ \begin{array}{ccc} J' & L' & J_f \\ L & J & k_i \end{array} \right\} \left\{ \begin{array}{ccc} J' & J_i & \bar{L} \\ J_i & J & k_i \end{array} \right\} \\
& \times \varepsilon^{\mathrm{det}\,*}_{k_i 0}(pL, p'L')\, h_{\alpha J,\, \alpha' J'}\, \sqrt{\pi}\, Y_{k_i q_i}(\theta_2, \varphi_2)\,, \qquad (5.5)
\end{aligned}
$$

where the same notations as in Eqs. (5.2)–(5.4) are employed. As seen from Eq. (5.5), an interference of the transition amplitudes of the individual decay paths occurs owing to the coherent population of the intermediate resonances.

One may note that an expression similar to Equation (5.5) can be obtained also for the angular distribution of the first-step fluorescence γ_1 photon, if the correlation function (5.2) is integrated over the emission angles θ_2, φ_2. At the first glance, this might be very surprising as the γ_1 angular distribution appears to be more complex than usual dipole distributions of fluorescence photons [47] even if the second-step characteristic photon γ_2 remains unobserved. This behavior, however, is caused by the known emission of a second photon and, actually, has been discussed in the context of the sequential two-photon double ionization [101, 102].

5.2.3 Polarization of the second-step photons

Apart from the angular properties of the characteristic fluorescence photons, usually, it is also convenient to measure their degrees of (linear or circular) polarization. In order to analyze this polarization, one needs first to obtain the corresponding spin density matrix of the photons, as discussed in Subsection 2.4.2. If we assume the first-step γ_1 photons to be unobserved, the spin density matrix of the second-step

γ_2 photons can be expressed as follows [109],

$$\left\langle \hat{\mathbf{k}}_{\gamma_2}, \lambda \,|\rho|\, \hat{\mathbf{k}}_{\gamma_2}, \lambda' \right\rangle = \frac{1}{8\pi} \sum_{\bar{p}\bar{L},pL,p'L'} \sum_{k_i q_i} \sum_{\alpha J,\alpha' J'} \lambda^p \lambda'^{p'} \hat{L}\hat{L}' \, (-1)^{J_i+2J+J_f+\bar{L}+1} \, \rho_{k_i q_i}(\alpha_i J_i)$$
$$\times \left\{ \begin{array}{ccc} L & L' & k_i \\ J' & J & J_f \end{array} \right\} \left\{ \begin{array}{ccc} J & J' & k_i \\ J_i & J_i & \bar{L} \end{array} \right\} \langle L\lambda, L'-\lambda' \mid k_i \lambda - \lambda' \rangle$$
$$\times \bar{M}_{\bar{p}\bar{L}} \, \bar{M}^*_{\bar{p}'\bar{L}'} \, M_{pL} \, M^*_{p'L'} \, D^{k_i\,*}_{\lambda-\lambda' q_i}(0, \theta_2, \varphi_2) \, h_{\alpha J,\alpha' J'} \, . \tag{5.6}$$

In this expression, we have made use of the same notations as in Eq. (5.2). Moreover, $\hat{\mathbf{k}}_{\gamma_2}$ denotes the unit wave vector of the second-step γ_2 photon.

5.2.4 A particular case: Application to lithiumlike ions

In this subsection, we will apply the formalism obtained above to a particular case of lithiumlike ions, that is, the two-step radiative cascade

$$\begin{aligned} 1s2p^2 \; J_i = 1/2, 3/2 \;\; &\longrightarrow \;\; \gamma_1 + \left\{ \begin{array}{l} 1s2s2p \; J = 1/2 \\ 1s2s2p \; J' = 3/2 \end{array} \right\} \\ &\longrightarrow \;\; \gamma_1 + \gamma_2 + 1s^2 2s \; J_f = 1/2 \, . \end{aligned} \tag{5.7}$$

It is noted that all the radiative transitions involved here are E1-allowed. For dipole fluorescence photons, their angular and polarization properties are determined just by second-rank statistical tensors, $\rho_{2q}(\alpha_i J_i)$. In the radiative decay cascade (5.7), the initial levels $1s2p^2 \; J_i = 1/2, 3/2$ might be produced either by electron impact excitation or by resonant electron capture, for which the quantization z axis can be chosen along the corresponding electron beam direction. For this particular choice of the "collision" geometry, only one projection, $\rho_{20}(\alpha_i J_i)$, of the statistical tensors remains nonzero and, hence, the initial levels are fully characterized by the alignment parameter $\mathcal{A}_2(\alpha_i J_i) = \rho_{20}(\alpha_i J_i)/\rho_{00}(\alpha_i J_i)$. In the following, this radiative cascade is considered always in the chosen geometry and also within the E1 approximation of the radiation fields, i.e., $p = p' = \bar{p} = \bar{p}' = 0$ and $L = L' = \bar{L} = \bar{L}' = 1$. Furthermore, the cascade process (5.7) is also displayed in Figure 5.2 for lithium-like W^{71+} ions together with other dominant decay channels from the $1s2p^2 \; J_i = 1/2, 3/2$ levels and their branching fractions estimated [100]. While the doubly excited (initial) states decay predominantly via the $1s^2 2p \; J_f = 1/2, 3/2$ levels, about 0.01% of them proceeds via the radiative cascade (5.7) and, indeed, might be measured experimentally.

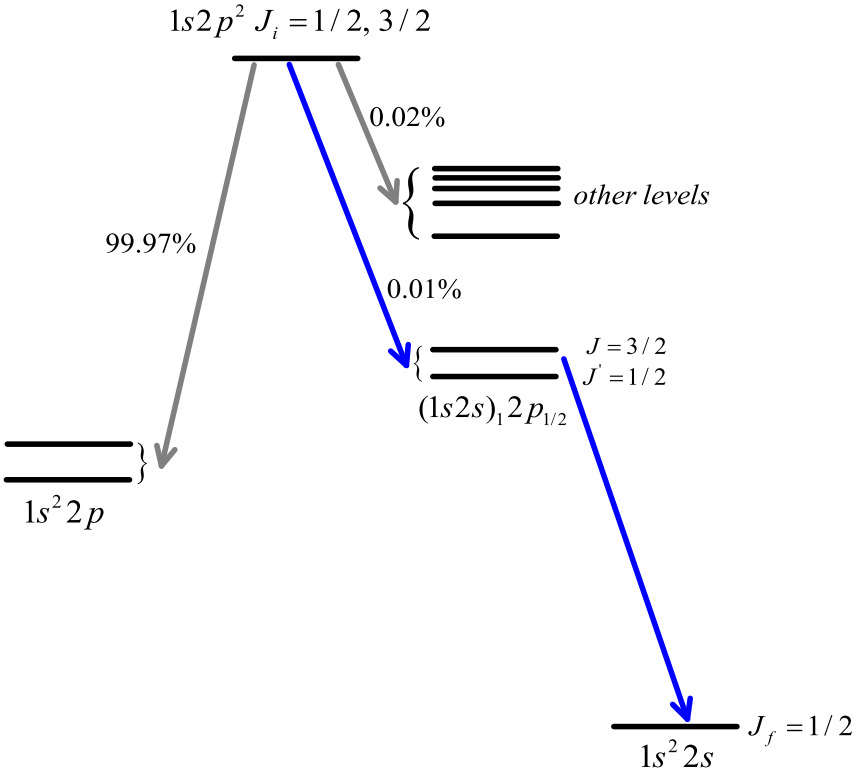

Figure 5.2: Level scheme and dominant decay channels of the doubly excited (initial) levels $1s2p^2\ J_i = 1/2, 3/2$ for lithiumlike W^{71+} ions, together with their branching fractions estimated. About 0.01% of them proceeds via the radiative cascade (5.7) of interest as marked in blue.

For the radiative cascade starting from the initial $J_i = 1/2$ level, the associated angular correlation function can be expressed as the following normalized form [100],

$$W^{\gamma_1\gamma_2}_{J_i=1/2}(\Omega_{12}) \propto 1 + \beta^{\gamma_1\gamma_2}_{J_i=1/2}\, P_2(\cos\Omega_{12})\,. \tag{5.8}$$

Here, $P_2(\cos\Omega_{12})$ denotes the second-order Legendre polynomial as a function of the opening angle $\cos\Omega_{12} = \cos\theta_1\cos\theta_2 + \sin\theta_1\sin\theta_2\cos(\varphi_1 - \varphi_2)$ between the emission directions of the two characteristic photons γ_1 and γ_2. Moreover, the corresponding anisotropy parameter $\beta^{\gamma_1\gamma_2}_{J_i=1/2}$ is given by [100]

$$\beta^{\gamma_1\gamma_2}_{J_i=1/2} = \frac{\frac{1}{4}\,|M^{\gamma_1}_{3/2}|^2\,|M^{\gamma_2}_{3/2}|^2\,\frac{1}{\Gamma_{3/2}} - \Re(M^{\gamma_1}_{1/2}\,M^{\gamma_1 *}_{3/2}\,M^{\gamma_2}_{1/2}\,M^{\gamma_2 *}_{3/2}\,h_{1/2,3/2})}{|M^{\gamma_1}_{3/2}|^2\,|M^{\gamma_2}_{3/2}|^2\,\frac{1}{\Gamma_{3/2}} + 2\,|M^{\gamma_1}_{1/2}|^2\,|M^{\gamma_2}_{1/2}|^2\,\frac{1}{\Gamma_{1/2}}}\,, \tag{5.9}$$

in which the shorthand notations $M^{\gamma_1}_J \equiv \langle 1s2s2p\ J\,\|H_{\gamma_1}(E1)\|\,1s2p^2\ J_i = 1/2\rangle$ and

$M_J^{\gamma 2} \equiv \langle 1s^2 2s\ J_f = 1/2 \,\|H_{\gamma_2}(E1)\|\, 1s2s2p\ J\rangle$ with $J = 1/2, 3/2$ have been used to denote the reduced transition amplitudes for the first- and second-step decays in the cascade (5.7). Moreover, $\Re$ stands for taking the real part of the complex term. The depolarization factor $h_{1/2,3/2}$ has been simplified from Eq. (5.4) for the particular $1s2s2p\ J = 1/2, 3/2$ resonances. As can be found, the anisotropy parameter $\beta^{\gamma_1\gamma_2}_{J_i=1/2}$ is independent of the polarization state $\rho_{k_i q_i}(\alpha_i J_i)$ of the initial level. This can be readily understood as energy levels with total angular momentum $J = 1/2$ cannot be aligned in the course of any axially symmetric process.

In contrast to the $1s2p^2\ J_i = 1/2$ level, the initial $1s2p^2\ J_i = 3/2$ one is usually aligned along some preferential direction, such as, the electron beam direction if it is populated via electron collision processes. In this case, if we employ the coordinate system in which the z axis is along the alignment and the x axis is chosen to give rise to $\varphi_1 = 0$, the associated angular correlation function $W^{\gamma_1\gamma_2}_{J_i=3/2}$ would depend on three angles θ_1, θ_2, and φ_2. As usual, if the photon detectors are mounted in a plane perpendicular to the beam, i.e., $\theta_1 = \theta_2 = 90^\circ$, the correlation function depends just on φ_2. After a standard normalization procedure, it gets the following form [100],

$$W^{\gamma_1\gamma_2}_{J_i=3/2}(\varphi_2) \propto 1 + \beta^{\gamma_1\gamma_2}_{J_i=3/2}\, P_2(\cos\varphi_2)\,. \tag{5.10}$$

Here, φ_2 is the azimuth angle of the second-step γ_2 photon emission, and $\beta^{\gamma_1\gamma_2}_{J_i=3/2}$ is the corresponding anisotropy parameter [100]

$$\beta^{\gamma_1\gamma_2}_{J_i=3/2} = \frac{2(1-\mathcal{A}_2)\left[\sqrt{10}\,\Re\left(M^{\gamma_1}_{1/2} M^{\gamma_1 *}_{3/2} M^{\gamma_2}_{1/2} M^{\gamma_2 *}_{3/2}\ h_{1/2,3/2}\right) \ -\ 2\,\frac{|M^{\gamma_1}_{3/2}|^2 |M^{\gamma_2}_{3/2}|^2}{\Gamma_{3/2}}\right]}{10(4-\mathcal{A}_2)\,\frac{|M^{\gamma_1}_{1/2}|^2 |M^{\gamma_2}_{1/2}|^2}{\Gamma_{1/2}} \ +\ (20+\mathcal{A}_2)\,\frac{|M^{\gamma_1}_{3/2}|^2 |M^{\gamma_2}_{3/2}|^2}{\Gamma_{3/2}} \ -\ 3\sqrt{10}\,\mathcal{A}_2\,\Re\left(M^{\gamma_1}_{1/2} M^{\gamma_1 *}_{3/2} M^{\gamma_2}_{1/2} M^{\gamma_2 *}_{3/2}\ h_{1/2,3/2}\right)}\,. \tag{5.11}$$

In this expression, while the depolarization factor $h_{1/2,3/2}$ and the reduced transition amplitudes $M_J^{\gamma 2}$ remain the same as in Eq. (5.9), the reduced amplitudes for the first-step decay is defined by $M_J^{\gamma 1} \equiv \langle 1s2s2p\ J \,\|H_{\gamma_1}(E1)\|\, 1s2p^2\ J_i = 3/2\rangle$. Moreover, $\mathcal{A}_2$ is the alignment parameter of the initial $1s2p^2\ J_i = 3/2$ level.

Now, let us proceed with the parameterization of the angular distribution of the second-step γ_2 photons emitted in the process (5.7) by using Equation (5.5). For the radiative cascade starting initially from the $1s2p^2\ J_i = 1/2$ level, the corresponding γ_2 angular distribution is isotropic and, thus, is not sensitive to the splitting of the two intermediate resonances, as can be deduced from Eq. (5.5). Of course, this case is not interesting for our purpose to analyze level splittings in highly charged ions. If the radiative cascade starts initially from the doubly excited $1s2p^2\ J_i = 3/2$ level,

however, the angular distribution of the emitted characteristic γ_2 photons depends on the splitting and can be parametrized as [100]

$$W^{\gamma_2}_{J_i=3/2}(\theta_2) \propto 1 + \beta^{\gamma_2}_{J_i=3/2}\, P_2(\cos\theta_2)\,. \tag{5.12}$$

Here, θ_2 is the polar angle of the second-step photon emission with respect to the quantization axis. The anisotropy parameter $\beta^{\gamma_2}_{J_i=3/2}$ is defined by [100]

$$\beta^{\gamma_2}_{J_i=3/2} = \mathcal{A}_2\, \frac{|M^{\gamma_1}_{3/2}|^2\, |M^{\gamma_2}_{3/2}|^2\, \frac{1}{\Gamma_{3/2}} \;+\; 4\sqrt{10}\,\Re\left(M^{\gamma_1}_{1/2}\, M^{\gamma_1 *}_{3/2}\, M^{\gamma_2}_{1/2}\, M^{\gamma_2 *}_{3/2}\, h_{1/2,3/2}\right)}{10\left(|M^{\gamma_1}_{3/2}|^2\, |M^{\gamma_2}_{3/2}|^2\, \frac{1}{\Gamma_{3/2}} \;+\; 2\,|M^{\gamma_1}_{1/2}|^2\, |M^{\gamma_2}_{1/2}|^2\, \frac{1}{\Gamma_{1/2}}\right)}. \tag{5.13}$$

Again, all of the reduced transition amplitudes and the depolarization factor here are defined the same as in the anisotropy parameter (5.11). As seen from this expression, this anisotropy parameter is proportional directly to the alignment parameter $\mathcal{A}_2$ of the $1s2p^2\ J_i = 3/2$ level, which means that the strongest anisotropy of the emitted second-step photons is always given by the largest alignment of it.

Apart from the angular distribution of the characteristic fluorescence γ_2 photons as discussed above, one can also study their polarization properties. By comparing Equations (2.15) and (5.6) and then applying them to the particular cascade (5.7), for instance, one can readily obtain the linear polarization $P_1(\theta_2)$ for the second-step γ_2 photons as follows [109],

$$P_1 = \frac{3\mathcal{A}_2 \sin^2\theta_2 \left[\frac{|M^{\gamma_1}_{3/2}|^2 |M^{\gamma_2}_{3/2}|^2}{4\Gamma_{3/2}} + \sqrt{10}\Re\left(M^{\gamma_1}_{1/2} M^{\gamma_1 *}_{3/2} M^{\gamma_2}_{1/2} M^{\gamma_2 *}_{3/2} h_{1/2,3/2}\right)\right]}{\mathcal{A}_2(1-3\cos^2\theta_2)\left[\frac{|M^{\gamma_1}_{3/2}|^2 |M^{\gamma_2}_{3/2}|^2}{4\Gamma_{3/2}} + \sqrt{10}\Re\left(M^{\gamma_1}_{1/2} M^{\gamma_1 *}_{3/2} M^{\gamma_2}_{1/2} M^{\gamma_2 *}_{3/2} h_{1/2,3/2}\right)\right] - 5\left[2\frac{|M^{\gamma_1}_{1/2}|^2 |M^{\gamma_2}_{1/2}|^2}{\Gamma_{1/2}} + \frac{|M^{\gamma_1}_{3/2}|^2 |M^{\gamma_2}_{3/2}|^2}{\Gamma_{3/2}}\right]}, \tag{5.14}$$

in which all of the quantities denote the same meanings as defined in Equation (5.13).

Up to now, we have parameterized all necessary formulae for studying the photon polarization and angular distribution as well as the photon-photon angular correlation of the characteristic fluorescence emissions from the radiative cascade (5.7). It follows from these formulae that any further analysis of them requires to calculate firstly the reduced transition amplitudes. As discussed in Sec. 2.5, again, these amplitudes are calculated with the use of the GRASP92 [66] and RATIP [68] packages. In order to produce accurate energy levels and wave functions, the configurations $1s^22s$, $1s^22p$, $1s2s^2$, $1s2s2p$ and $1s2p^2$ are used in the computations.

5.3 Results and discussion

Now, we are ready to make use of the formulas (5.8)–(5.14) to study the angular and polarization properties of the characteristic fluorescence γ_1 and γ_2 photons emitted from the radiative cascade via overlapping intermediate resonances. This particular cascade of inner-shell excited lithiumlike ions is chosen here as all of its individual transitions are E1-allowed and thus no other higher multipoles of the radiation fields and corresponding transition amplitudes need to be considered. Moreover, a level crossing of its two intermediate resonances $1s2s2p_{1/2}$ $J = 1/2,\ 3/2$ along the lithium isoelectronic sequence is found among $74 \leq Z \leq 79$ [100], which makes these ions very interesting for exploring the depolarization effect. In Figure 5.3, we display the level splitting $\Delta\omega$ (in a.u.) of the intermediate resonances $1s2s2p_{1/2}$ $J = 1/2, 3/2$ as a function of nuclear charge Z along the lithium isoelectronic sequence. A crossing of these resonances appears approximately among $74 \leq Z \leq 79$, near to which the depolarization effect is expected to be the largest.

Below, all calculations are performed for the radiative cascade (5.7) of lithiumlike W^{71+} ions to investigate the angular and polarization properties of the emitted characteristic fluorescence photons. In these calculations, the level splitting of the

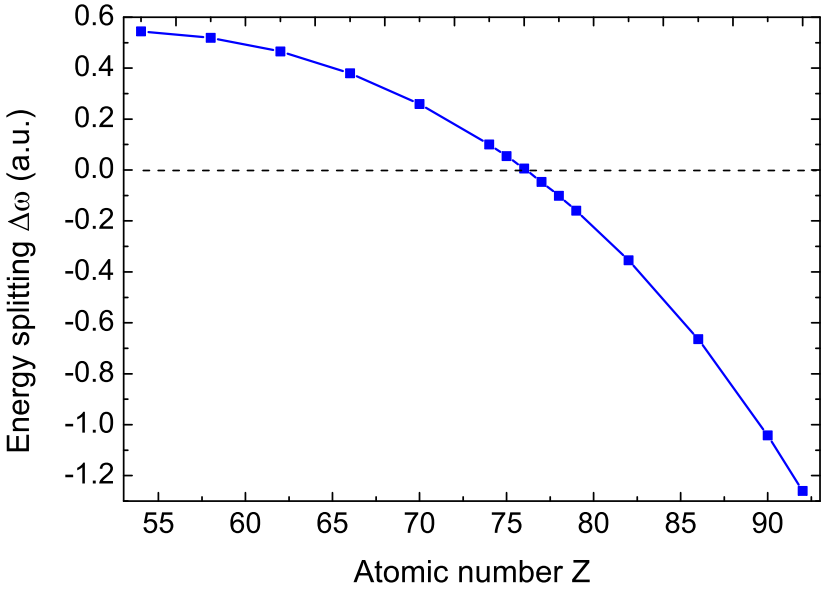

Figure 5.3: Level splitting $\Delta\omega$ of the two intermediate $1s2s2p_{1/2}$ $J = 1/2, 3/2$ resonances as a function of nuclear charge Z along the lithium isoelectronic sequence. A crossing of these two resonances occurs among $74 \leq Z \leq 79$ approximately.

intermediate overlapping resonances is assumed to be a variable. While the transition amplitudes used depend weakly on the exact level energies and nuclear charge, an accurate calculation of the level splitting is difficult especially near to the crossing of the resonances. Therefore, we here propose several experimental scenarios for determining this splitting either by means of measurements on the angular distribution or polarization of the second-step γ_2 photons or by a coincidence measurement on the photon-photon angular correlation.

5.3.1 Angular distribution of the second-step photons

How large is the depolarization effect on a well-defined single line in x-ray emission spectrum of highly charged ions? To answer this question, let us first consider the angular distribution of the second-step γ_2 photons from the radiative cascade (5.7), which is usually much easier to be observed than two-photon angular correlation in coincidence measurements. While the angular distribution of the γ_2 photon is always isotropic for the cascade starting initially from the unpolarized $1s2p^2\ J_i = 1/2$ level, a strong dependence upon the level splitting is found for the one that starts from

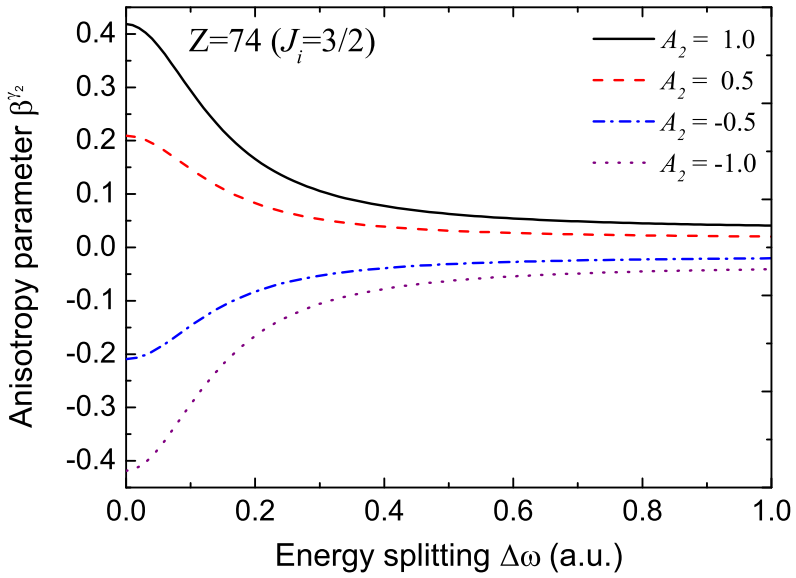

Figure 5.4: Anisotropy parameters (5.13) of the γ_2 angular distribution as functions of the level splitting $\Delta\omega$. Results are shown for four assumed alignment parameters of the $1s2p^2\ J_i = 3/2$ resonance of lithiumlike W^{71+} ions owing to its prior excitations: $\mathcal{A}_2 = 1.0$ (black solid line), 0.5 (red dashed lined), -0.5 (blue dashed-dotted line), and -1.0 (gray dotted line).

the aligned $1s2p^2\ J_i = 3/2$ resonance.

Figure 5.4 displays the anisotropy parameters (5.13) of the γ_2 angular distribution as functions of the level splitting $\Delta\omega$ of the intermediate (overlapping) resonances $1s2s2p_{1/2}\ J = 1/2,\ 3/2$ [100]. Results are shown here for assumed alignment parameters of the $1s2p^2\ J_i = 3/2$ resonance of lithiumlike W^{71+} ions, as they may arise owing to different excitation processes of it. As can be seen from this figure, the anisotropy parameter $\beta^{\gamma_2}_{J_i=3/2}$ appears to be very sensitive to the level splitting and, especially, in the range of $\Delta\omega \lesssim 0.2$ a.u. ≈ 5.4 eV. The large changes of the γ_2 anisotropy parameter within this range can be measured quite readily for highly charged ions by using present-day photon detection techniques [39, 86]. This kind of measurements requires to consider the anisotropy parameter as a function of the nuclear charge Z since for any given lithiumlike ions the level splitting $\Delta\omega$ is fixed. Moreover, as seen clearly from Figure 5.4, the observed anisotropy parameter should be proportional to the alignment of the initial $1s2p^2\ J_i = 3/2$ resonance.

Besides the anisotropy parameter $\beta^{\gamma_2}_{J_i=3/2}$, Fig. 5.5 also displays the corresponding angular distribution of the second-step γ_2 photons as emitted in the cascade (5.7). Different level splittings of the intermediate resonances $1s2s2p_{1/2}\ J = 1/2, 3/2$ are

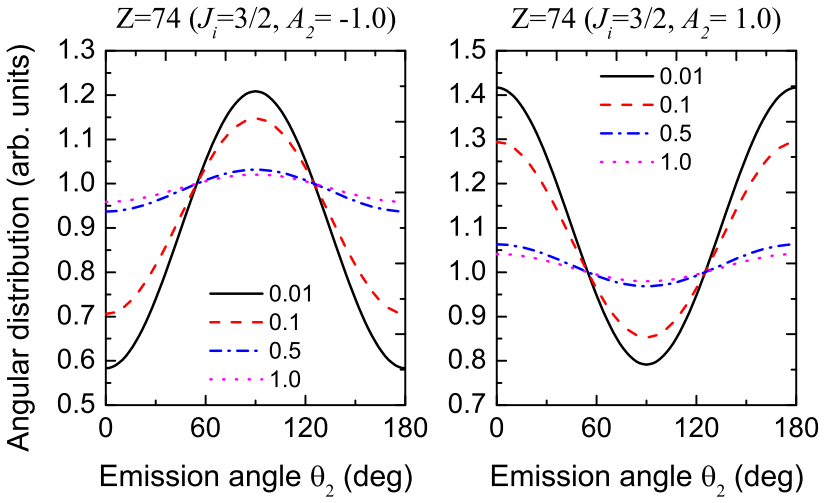

Figure 5.5: Angular distribution of the second-step γ_2 photons emitted in the decay cascade (5.7). Results are shown for two assumed alignment parameters $\mathcal{A}_2 = -1.0$ (left panel) and 1.0 (right panel) of the $1s2p^2\ J_i = 3/2$ resonance of lithiumlike W^{71+} ions. For each of them, four different level splittings of the intermediate resonances $1s2s2p_{1/2}\ J = 1/2, 3/2$ are assumed: $\Delta\omega = 0.01$ a.u. (black solid line), 0.1 a.u. (red dashed line), 0.5 a.u. (blue dash-dotted line), and 1.0 a.u. (pink dotted line).

assumed here in order to show a strong dependence of the γ_2 angular distribution on the level splitting. Obviously, moreover, the overall angular emission pattern of the fluorescence γ_2 photons depends also on the alignment of the initial $1s2p^2\ J_i = 3/2$ level, which is possible to be controlled experimentally in its prior excitations. This alignment can be readily monitored by recording other fluorescence photons emitted from the (radiative) decay of this level to other energetically lower (isolated) levels such as $1s^2 2p\ J = 1/2, 3/2$, as shown graphically in Fig. 5.2. Therefore, such a rather strong dependence obtained for the γ_2 angular distribution might make experimental measurements on it become a suitable tool for determining tiny level splittings in excited highly charged ions.

5.3.2 Linear polarization of the second-step photons

For the emitted second-step γ_2 photons, another feasible experimental scenario is to measure the polarization of them. Figure 5.6, for instance, displays the calculated degree of linear polarization P_1 as defined by Eq. (5.14), as functions of the emission

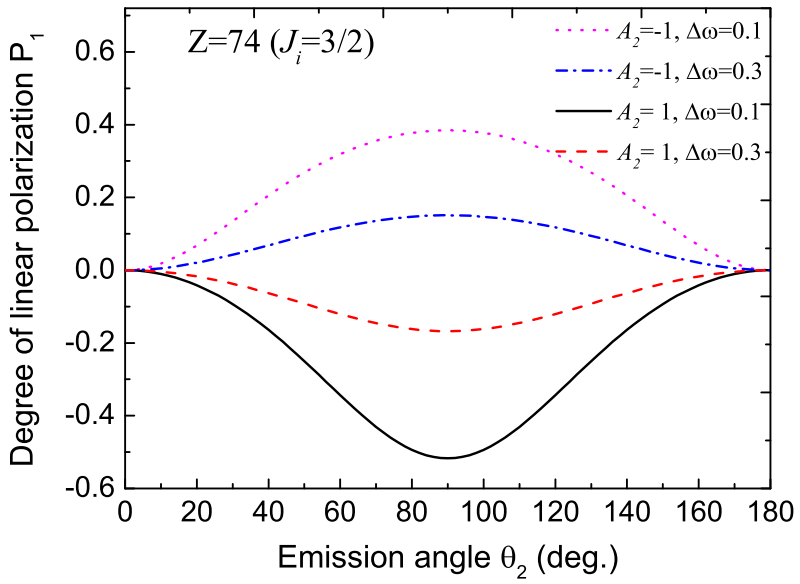

Figure 5.6: Degree of linear polarization of the γ_2 photons as functions of the emission angle θ. Results are shown for different combinations between the alignment $\mathcal{A}_2$ of the $1s2p^2\ J_i = 3/2$ level of lithiumlike W^{71+} ions and the splitting $\Delta\omega$ (a.u.) of the $1s2s2p_{1/2}\ J = 1/2, 3/2$ resonances: -1 and 0.1 (magenta dotted line), -1 and 0.3 (blue dash-dotted line), 1 and 0.1 (black solid line) as well as 1 and 0.3 (red dashed line).

angle θ_2 [109]. Results are presented for several combinations of assumed level splittings $\Delta\omega = 0.1$, 0.3 a.u. and of initial alignments with $\mathcal{A}_2 = \pm 1$. As seen from this figure, a very strong linear polarization is found for those γ_2 photons emitted perpendicular to the quantization axis, i.e., the incoming direction of the collision electrons that align the initial $1s2p^2\ J_i = 3/2$ level. For given small level splittings, similar to the anisotropy parameter $\beta^{\gamma_2}_{J_i=3/2}$, the linear polarization of the γ_2 photons is also very sensitive with respect to the alignment of the $1s2p^2\ J_i = 3/2$ level, not only to its magnitude but also its sign. Apart from the alignment, moreover, this polarization strongly depends also on the level splitting $\Delta\omega$ itself, which makes it interesting to perform further analysis for our purpose.

The linear polarization P_1 of the characteristic γ_2 photons has been found most sensitive to both the alignment and the level splitting at emission angles of $\theta \approx 90^o$. In Figure 5.7, therefore, we display the corresponding linear polarization for those γ_2 photons which are emitted at $\theta = 90^o$, as functions of the splitting $\Delta\omega$ of the two $1s2s2p\ J = 1/2, 3/2$ levels [109]. Similar to the angular distribution of the characteristic fluorescence γ_2 photons as discussed above, again, a very strong (lifetime-induced) dependence of the linear polarization on the level splitting is obtained. As

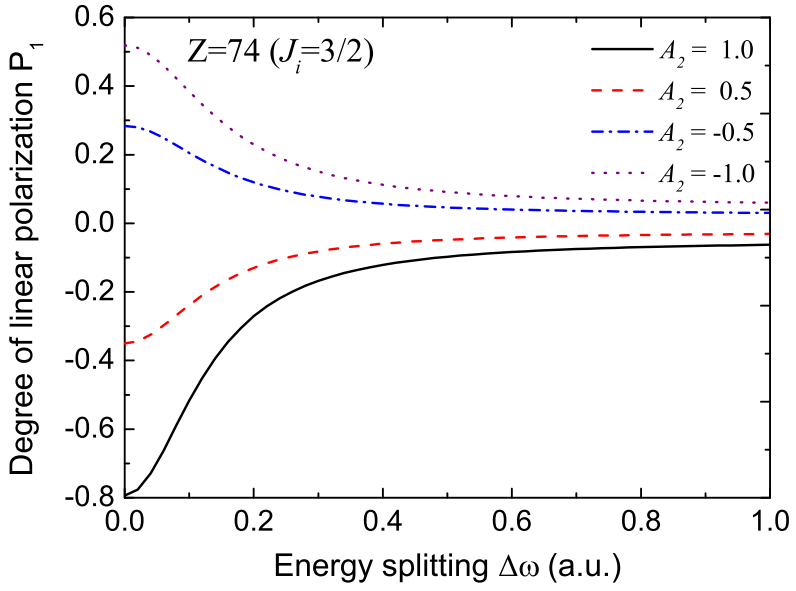

Figure 5.7: Degree of linear polarization of the second-step γ_2 photons as functions of the level splitting. Results are shown here for those of them that are emitted under $\theta = 90^o$ for four assumed alignment parameters of the $1s2p^2\ J_i = 3/2$ level: $\mathcal{A}_2 = -1.0$ (black solid line), -0.5 (blue dashed line), 0.5 (magenta dotted line), and 1.0 (red dash-dotted line).

the linear polarization can be readily measured for a wide range of photon energies nowadays by using Compton polarimetry [33, 39], accurate polarization measurements on the second-step γ_2 photons may help explore these level splittings.

5.3.3 Photon-photon angular correlation

Apart from recording only the second-step γ_2 fluorescence photons, the γ_1–γ_2 angular correlation functions (5.8) and (5.10) can also be used to investigate the radiative cascade (5.7) that proceeds via the overlapping intermediate resonances for our purpose, for instance, by measuring the corresponding anisotropy parameters, $\beta^{\gamma_1\gamma_2}$. In Figure 5.8, we present these anisotropy parameters as functions of the level splitting $\Delta\omega$ of the two intermediate levels [100]. Results are shown for both the cascade processes that start initially from the $1s2p^2\ J_i = 1/2$ (left panel) and $1s2p^2\ J_i = 3/2$ (right panel) resonances of lithiumlike W^{71+} ions, respectively. In the latter, four different alignment parameters $\mathcal{A}_2 = -1.0$, -0.5, 0.0 and 0.5 of the $1s2p^2\ J_i = 3/2$ level are assumed. For the case of the $1s2p^2\ J_i = 1/2$ level, in particular, the corresponding γ_1–γ_2 angular correlation function exhibits a strong anisotropy when

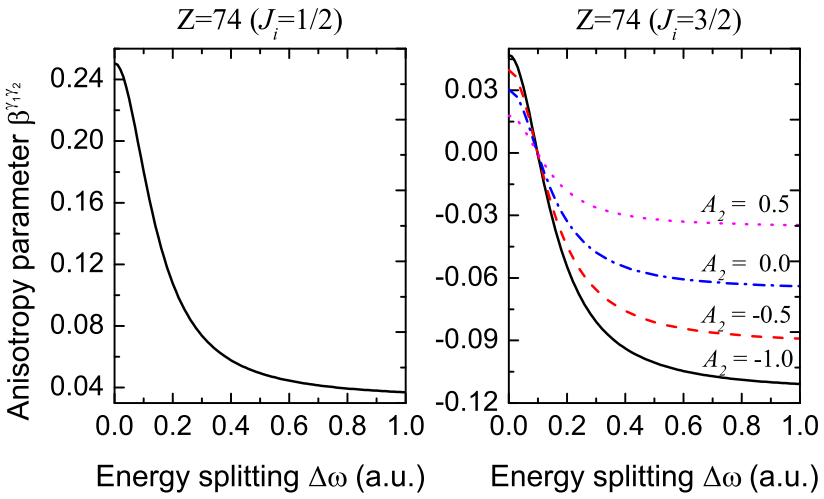

Figure 5.8: Anisotropy parameters (5.9) and (5.11) for the photon-photon angular correlation in the radiative cascade (5.7) which starts initially from the resonances $1s2p^2\ J_i = 1/2$ (left panel) and $1s2p^2\ J_i = 3/2$ (right panel) of lithiumlike W^{71+} ions, respectively. In the latter, these parameters are presented here as functions of the level splitting $\Delta\omega$ for four assumed alignment parameters: $\mathcal{A}_2 = -1.0$ (black solid line), -0.5 (red dotted line), 0.0 (blue dashed-dotted line), and 0.5 (pink dotted line).

compared with an isotropic angular emission of the second-step γ_2 photons alone, especially, in the range of $\Delta\omega \lesssim 0.2$ a.u. In contrast, the cascade of the $1s2p^2\ J_i = 3/2$ resonance just gives rise to a (relatively) weak angular correlation anisotropy. As seen clearly from the right panel of Figure 5.8, moreover, the anisotropy parameter $\beta^{\gamma_1\gamma_2}_{J_i=3/2}$ changes its sign at $\Delta\omega \simeq 0.1$ a.u. $\simeq 2.7$ eV and thus becomes positive for smaller level splittings, which means that the photon-photon angular correlation behavior is changed qualitatively near to the level crossing. This qualitative change of the angular correlation may provide a good chance to reach a new level of accuracy in the determination of tiny level splittings.

This kind of change in the γ_1–γ_2 angular correlation function $\beta^{\gamma_1\gamma_2}_{J_i=3/2}$ is illustrated explicit in the right panel of Figure 5.9, which displays the angular correlation functions (5.8) and (5.10) for the radiative cascade (5.7) that starts respectively from the initial $1s2p^2\ J_i = 1/2$ (left panel) and $1s2p^2\ J_i = 3/2$ resonances of lithiumlike W^{71+} ions. The results are shown here for the same (assumed) level splittings as in Figure 5.5 and in the latter two different alignment parameters $\mathcal{A}_2 = -1.0$ (middle panel) and 0.0 (right panel) of the $1s2p^2\ J_i = 3/2$ level are assumed [100]. As seen clearly, the obtained angular correlation function is very sensitive to the level splitting $\Delta\omega$ in both cases. While the smallest $\Delta\omega$ gives rise to the strongest

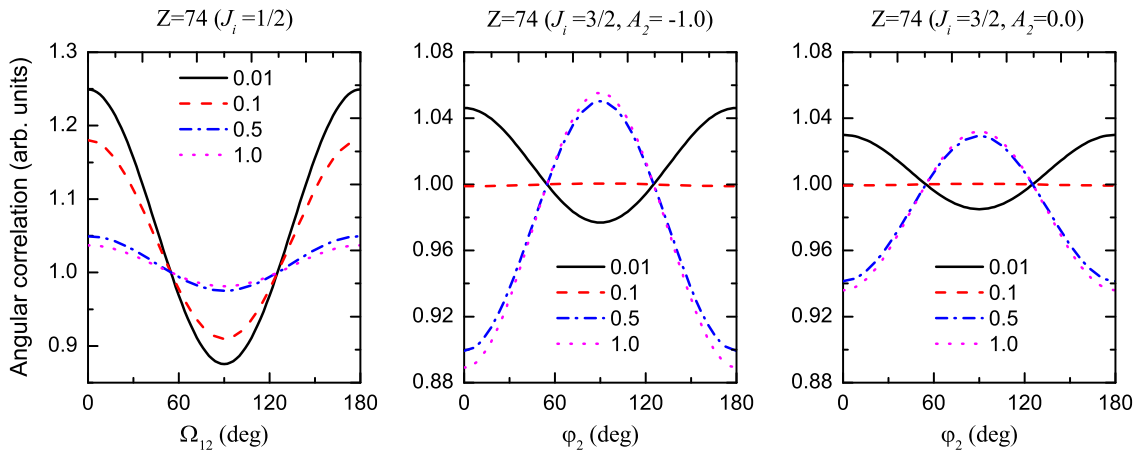

Figure 5.9: Photon-photon angular correlation in the respective radiative cascades (5.7) of the initial $1s2p^2\ J_i = 1/2$ (left panel) and $1s2p^2\ J_i = 3/2$ resonances of lithiumlike W^{71+} ions. In the latter, two different alignment parameters $\mathcal{A}_2 = -1.0$ (middle panel) and 0.0 (right panel) are assumed. Results are shown for the same level splittings of the intermediate resonances and by using the same symbols as in Figure 5.5.

anisotropic angular correlation $W^{\gamma_1\gamma_2}_{J_i=1/2}(\varphi_2)$, the lifetime-induced depolarization of the overlapping resonances could lead to a qualitatively different angular behavior of photons emitted in the two-step cascade of the $1s2p^2\ J_i = 3/2$ resonance.

From the theoretical analysis above we conclude that the angular and polarization properties of the characteristic fluorescence photons emitted from (partially) overlapping resonances of atoms or ions are strongly influenced by the lifetime-induced depolarization of the resonances, especially, when the level splitting of them becomes comparable with their (natural) linewidths in magnitude. We therefore suggest that accurate polarization or angle-resolved measurements on characteristic photon emissions may serve as a promising tool to determine tiny level splittings of atomic or ionic resonances that overlap with each other. Such kind of measurements is feasible nowadays by using solid-state or crystal (x-ray) photon detectors.

6 Stimulated plus spontaneous decay of ions: Determination of the hyperfine splitting

In this chapter, we shall propose an experimental scheme for determining hyperfine splitting in highly charged heliumlike ions with the utilization of an angle-resolved spectroscopic analysis. In particular, such a proposal can be achieved by performing two respective measurements on the angular distribution or linear polarization of the hyperfine $1s2p\ ^3P_1, F = I-1, I, I+1 \to 1s^2\ ^1S_0, F_f = I$ emission of heliumlike ions following a stimulated decay of the initial $1s2s\ ^1S_0, F_i = I$ resonance. In the next section, we will make a very brief introduction with respect to the studies of hyperfine splitting in heavy few-electron ions such as hydrogenlike or heliumlike ions. In order to simulate and explain the proposed experimental scheme, in Section 6.2 a theoretical method for its description based on the density matrix theory is presented. Finally, the simulated results are presented and discussed in Section 6.3. It is found that the obtained polarization and angular behaviors of the emitted characteristic photons depend strongly upon the splitting of the (partially) overlapping hyperfine $1s2p\ ^3P_1, F$ levels. This dependence could be a promising "signature" for determining the hyperfine splitting. The proposed scheme of measuring photon polarization and angular distribution are feasible with present-day photon detectors and thus might serve as a preliminary test of QED in the presence of strong Coulomb fields generated by heavy nuclei.

Before moving ahead, we claim that the main content of this chapter as presented below is based on our papers [*Phys. Rev. A* **93**, 063413 (2016); *Phys. Rev. A*, under review (2017)].

6.1 Hyperfine splitting in heavy few-electron ions

Hyperfine splitting in highly charged high-Z ions can provide an access to accurate tests of QED in strong Coulomb fields as generated by heavy nuclei. Hydrogen atom and hydrogenlike ions as the simplest atomic (or ionic) system have received a lot of attention in both theoretical and experimental studies of this kind. The hyperfine

splitting of the $1s$ ground-state level gives rise to the famous 21 cm hyperfine line of hydrogen [110]. With recent development of experimental techniques in producing and maintaining an ensemble of highly charged ions, the first successful measurement on the hyperfine $1s$ splitting of high-Z hydrogenlike ions was performed for $^{209}_{83}\mathrm{Bi}^{82+}$ [111]. Since this seminal work, there has been continuous interest in further exploring the $1s$ hyperfine splitting in $^{209}_{83}\mathrm{Bi}^{82+}$ [112–115] and also in other hydrogenlike ions such as $^{165}_{67}\mathrm{Ho}^{66+}$, $^{185}_{75}\mathrm{Re}^{74+}$, $^{187}_{75}\mathrm{Re}^{74+}$, $^{203}_{81}\mathrm{Tl}^{80+}$, $^{205}_{81}\mathrm{Tl}^{80+}$, $^{207}_{81}\mathrm{Tl}^{80+}$, and $^{207}_{82}\mathrm{Pb}^{81+}$ [116–120]. Among these investigations, some discrepancies between experimental and theoretical results were obtained, which were, at least in part, attributed to an improper understanding of QED or nuclear magnetization.

Apart from the simplest hydrogenlike ions, an experimental scheme for the measurement of the $2s$ hyperfine splitting in lithiumlike ions was presented with the aim to eliminate the discrepancies resulted from an improper understanding of QED and nuclear magnetization [121, 122]. Such kind of experimental measurements was performed just very recently for $^{141}_{59}\mathrm{Pr}^{56+}$ [123] and $^{209}_{83}\mathrm{Bi}^{80+}$ [124]. For these measurements, a very good agreement with previous theoretical results was achieved. Besides hydrogenlike and lithiumlike ions, the hyperfine splitting in berylliumlike ions was also studied [123].

Heliumlike ions represent another simple few-electron ionic system and thus are expected naturally to serve also for the same purpose. To the best of our knowledge, however, there are no such experimental studies up to the present, although some theoretical work has been done [125, 126]. This is because, compared to hydrogenlike or lithiumlike ions, there is no hyperfine splitting in the ground-state level of heliumlike ions. As for the excited levels such as $1s2p\ ^{1,3}P_1, F$, moreover, their natural linewidths are comparable in magnitude to or even larger than the corresponding hyperfine splitting, which will be hardly resolved by conventional fluorescence spectroscopy owing to their mutual overlap. Take the $1s2p\ ^3P_1, F$ levels for example, while the respective linewidth goes rapidly from 0.10 eV for $^{71}_{31}\mathrm{Ga}^{29+}$ to 12.82 eV for $^{209}_{83}\mathrm{Bi}^{81+}$, the corresponding hyperfine splitting changes just from 0.11 eV to 5.46 eV. Moreover, the transition energies from the excited (overlapping) $1s2p\ ^3P_1, F$ levels to the ground state are very large for highly charged ions, which could not be utilized for precision measurements. Therefore, it is very urgent to find a feasible experimental scheme to measure the hyperfine splitting in heliumlike ions.

For this reason, we propose a novel scheme to measure the hyperfine splitting in highly charged heliumlike ions by analyzing angle-resolved properties such as angular

distribution and polarization of emitted characteristic fluorescence photons. As a particular example, we explore these angle-resolved properties of the fluorescence γ_2 photons that are emitted from the $1s2s\ ^1S_0, F_i = I + \gamma_1 \rightarrow 1s2p\ ^3P_1, F = I - 1, I, I+1 \rightarrow 1s^2\ ^1S_0, F_f = I + \gamma_2$ radiative decay in order to determine the hyperfine splitting of the intermediate $1s2p\ ^3P_1, F = I - 1, I, I + 1$ levels. In this scheme, the initial $1s2s\ ^1S_0, F_i = I$ level can be populated selectively via a K-shell ionization of initially lithiumlike projectiles in relativistic collisions with low-density gas target at the experimental storage rings [127, 128]. Or, alternatively, it can also be produced selectively via the prompt decay $2s2p\ ^1P_1, F = I - 1, I, I + 1 \rightarrow 1s2s\ ^1S_0, F = I$ following resonant electron capture of initially hydrogenlike ions into the $2s2p\ ^1P_1$ resonance [129]. Owing to a very high selectivity, it is guaranteed that only the level $1s2s\ ^1S_0, F_i = I$ is populated initially. Therefore, the influence on the subsequent radiative decay from other neighboring levels can be neglected. For the initially populated level $1s2s\ ^1S_0, F_i = I$, as well known already, it decays primarily into the ground state via two-photon (2E1) emission [129–131]. Since we wish to understand the effect of the $1s2p\ ^3P_1, F = I - 1, I, I + 1$ hyperfine splitting upon the angular distribution and linear polarization of the fluorescence γ_2 photons, the aim is to make the first-step transition $1s2s\ ^1S_0, F_i = I \rightarrow 1s2p\ ^3P_1, F = I - 1, I, I + 1$ strong enough to compete with the 2E1 decay and thus to populate the intermediate levels. For this purpose, this transition is stimulated by a beam of laser with suitable intensities and adjustable photon energies $\hbar\omega$. Finally, the fluorescence γ_2 photons subsequently emitted in the second-step $1s2p\ ^3P_1, F = I-1, I, I+1 \rightarrow 1s^2\ ^1S_0, F_f = I$ spontaneous decay are measured by solid-state spectrometers [81, 132] or by Bragg crystal spectrometers [70]. It is found that the obtained γ_2 angular distribution and linear polarization strongly depend on the hyperfine structure values, if analyzed as a function of the γ_1 photon energy. In the following section we will present a density matrix description for the decay process above in order to explain the feasibility of this proposed scheme.

6.2 DM description of stimulated plus spontaneous decay

Let us consider the following general process of stimulated plus spontaneous decay

$$A\ (\alpha_i J_i F_i) + \gamma_1\ \rightarrow\ A^*(\alpha J I\, F = |J - I|, ..., J + I)\ \rightarrow\ A(\alpha_f J_f F_f) + \gamma_2\,, \quad (6.1)$$

in which the first-step radiative decay is stimulated by a laser which consists of γ_1 photons and the second-step spontaneous decay gives rise to γ_2 photon emission. While the initial and final hyperfine-structure levels $\alpha_i J_i F_i$ and $\alpha_f J_f F_f$ are assumed to be well-defined, the intermediate αJIF 'resonance' consists of a set of hyperfine-structure levels with $F = |J-I|, ..., J+I$ that overlap with each other due to finite lifetimes of them. In the notations above, F's denote total angular momenta of the hyperfine levels that consist of the associated angular momenta J's and nuclear spin I of the ions considered, and α's refer to all other quantum numbers that are needed for a unique specification of these levels. In contrast to typical *two-step* model for most of the excitation and subsequent decay of ions, we treat the whole process (6.1) together in order to allow for a *coherence transfer* of the (overlapping) intermediate hyperfine levels.

6.2.1 Second-order hyperfine transition amplitudes

The considered process (6.1) of stimulated plus spontaneous radiative decays of ions is quite analogue to the resonant Rayleigh scattering of photons by some ionic target. For the resonantly stimulated plus spontaneous radiative decays of the ions, the associated amplitude indeed contains singularities that can be removed by performing an (in)finite summation of the radiative corrections for the resonant (intermediate) levels [133, 134]. This summation naturally gives rise to the linewidths in the denominators of the second-order transition amplitude. For the case of a set of (overlapping) intermediate levels $\alpha JIF \equiv \beta F$ with $F = |J-I|, ..., J+I$, the second-order amplitude in the resonance approximation is expressed as [135]

$$\mathcal{M}^{\lambda_1,\lambda_2}_{M_i,M_f}(\hbar\omega) = \sum_{FM} \frac{\left\langle \beta_f F_f M_f \left| \sum_m \boldsymbol{\alpha}_m \cdot \boldsymbol{\epsilon}^*_{\lambda_2} e^{-i\boldsymbol{k}_2\cdot\boldsymbol{r}_m} \right| \beta F M \right\rangle \left\langle \beta F M \left| \sum_m \boldsymbol{\alpha}_m \cdot \boldsymbol{\epsilon}_{\lambda_1} e^{i\boldsymbol{k}_1\cdot\boldsymbol{r}_m} \right| \beta_i F_i M_i \right\rangle}{E_{\beta_i F_i} - E_{\beta F} - \hbar\omega + i\,\Gamma_{\beta F}/2}. \quad (6.2)$$

In the summations above, the total angular momentum F runs over $|J-I|, |J-I|+1, ..., J+I$ and for each F its projection M runs over $-F, -F+1, ..., F$. $\boldsymbol{\epsilon}_{\lambda_{1,2}}$ and $\boldsymbol{k}_{1,2}$ denote the polarization and wave vectors of the γ_1 and γ_2 photons, respectively. $\boldsymbol{r}_m$ and $\boldsymbol{\alpha}_m = (\alpha_{x,m}, \alpha_{y,m}, \alpha_{z,m})$ are the coordinate and the vector of the Dirac matrices for the mth electron. $|\beta_i F_i M_i\rangle \equiv |\alpha_i J_i I F_i M_i\rangle$ and $|\beta_f F_f M_f\rangle \equiv |\alpha_f J_f I F_f M_f\rangle$ characterize the initial and final states of the ions. Moreover, $E_{\beta_i F_i} - E_{\beta F}$ and $\Gamma_{\beta F}$ denote the transition energy and natural linewidth with respect to the level βF. The

operator $\sum_m \boldsymbol{\alpha}_m \cdot \boldsymbol{\epsilon}_\lambda \, e^{i\boldsymbol{k}\cdot\boldsymbol{r}_m}$ describes as usual the interaction of atomic electrons with the radiation field within the velocity gauge in terms of a sum of one-electron interaction operators. The second-order transition amplitude (6.2) can be explicitly simplified if the one-electron operator $\boldsymbol{\alpha_m} \cdot \boldsymbol{\epsilon}_\lambda e^{i\boldsymbol{k}\cdot\boldsymbol{r_m}}$ is decomposed into multipoles of the radiation field,

$$\boldsymbol{\alpha_m} \cdot \boldsymbol{\epsilon}_\lambda e^{i\boldsymbol{k}\cdot\boldsymbol{r_m}} = 4\pi \sum_{pLM_L} i^{L-p} \left[\boldsymbol{\epsilon}_\lambda \cdot \boldsymbol{Y}^{(p)*}_{LM_L}(\hat{\boldsymbol{k}})\right] \boldsymbol{\alpha_m} \, \boldsymbol{a}^p_{LM_L}(\boldsymbol{r_m}) \,, \tag{6.3}$$

in which $\boldsymbol{a}^p_{LM_L}(\boldsymbol{r})$ denotes the electric and magnetic multipoles of the radiation field and $\boldsymbol{Y}^{(p)}_{LM_L}(\hat{\boldsymbol{k}})$ is a vector spherical harmonics as function of $\hat{\boldsymbol{k}} \equiv \boldsymbol{k}/|\boldsymbol{k}|$. The explicit form of these multipoles has been discussed such as in the literature [136].

Now, we can simplify the general expression (6.2) by using Equation (6.3) and the Wigner-Eckart theorem. Figure 6.1 displays the level diagram of low-lying fine- and hyperfine-structure levels in heliumlike $^{71}_{31}\mathrm{Ga}^{29+}$ ions as an example and the geometry for the particular process $1s2s\ {}^1S_0, F_i = I + \gamma_1 \to 1s2p\ {}^3P_1, F = I-1, I, I+1 \to 1s^2\ {}^1S_0, F_f = I + \gamma_2$ as proposed above. If the geometry as shown in Figure 6.1 is employed, the corresponding second-order transition amplitude reads,

$$\begin{aligned}
\mathcal{M}^{\lambda_1,\lambda_2}_{M_i,M_f}(\hbar\omega) = \sum_{FM} \sum_{p_1 L_1 M_{L_1}} \sum_{p_2 L_2 M_{L_2}} & i^{-L_1-L_2} \, (i\lambda_1)^{p_1} \, (i\lambda_2)^{p_2} \, \delta_{\lambda_1 M_{L_1}} D^{L_2}_{M_{L_2}\lambda_2}(\varphi,\theta,0) \\
& \times [L_1, L_2]^{1/2} \, [F_i, F]^{-1/2} \, \langle F_f M_f, L_2 M_{L_2} \mid FM \rangle \, \langle FM, L_1 M_{L_1} \mid F_i M_i \rangle \\
& \times (-1)^{F_i - F_f} \, \frac{\left\langle F_f \left\| \sum_m \boldsymbol{\alpha}_m \boldsymbol{a}^{p_2}_{L_2}(\boldsymbol{r}_m) \right\| F \right\rangle \left\langle F \left\| \sum_m \boldsymbol{\alpha}_m \boldsymbol{a}^{p_1}_{L_1}(\boldsymbol{r}_m) \right\| F_i \right\rangle}{E_{F_i} - E_F - \hbar\omega + i\,\Gamma_F/2} .
\end{aligned} \tag{6.4}$$

Here, $\delta_{\lambda_1 M_{L_1}}$ is a Kronecker delta, and $[a, b] \equiv (2a+1)(2b+1)$. Moreover, individual photons are characterized in terms of their helicity λ and multipolarities pL with $p = 0$ for magnetic multipoles and $p = 1$ for electric ones. E_F and Γ_F denote the energy and linewidth of the $|F\rangle \equiv |\beta F\rangle$ hyperfine level. The reduced matrix element $\langle F_f \| \sum_m \boldsymbol{\alpha}_m \boldsymbol{a}^p_L(\boldsymbol{r}_m) \| F_i \rangle$ represents the hyperfine transition amplitude between the $|F_i\rangle$ and $|F_f\rangle$ levels. If the hyperfine-induced level mixing is neglected, this reduced hyperfine transition amplitude can be expressed in terms of the corresponding fine-structure reduced amplitude as [38, 126],

$$\begin{aligned}
& \left\langle F_f \left\| \sum\nolimits_m \boldsymbol{\alpha}_m \boldsymbol{a}^p_L(\boldsymbol{r}_m) \right\| F_i \right\rangle \\
& \quad = (-1)^{I+F_i+J_f+L} \, [F_i, F_f]^{1/2} \left\{ \begin{array}{ccc} J_i & I & F_i \\ F_f & L & J_f \end{array} \right\} \left\langle J_f \left\| \sum\nolimits_m \boldsymbol{\alpha}_m \boldsymbol{a}^p_L(\boldsymbol{r}_m) \right\| J_i \right\rangle ,
\end{aligned} \tag{6.5}$$

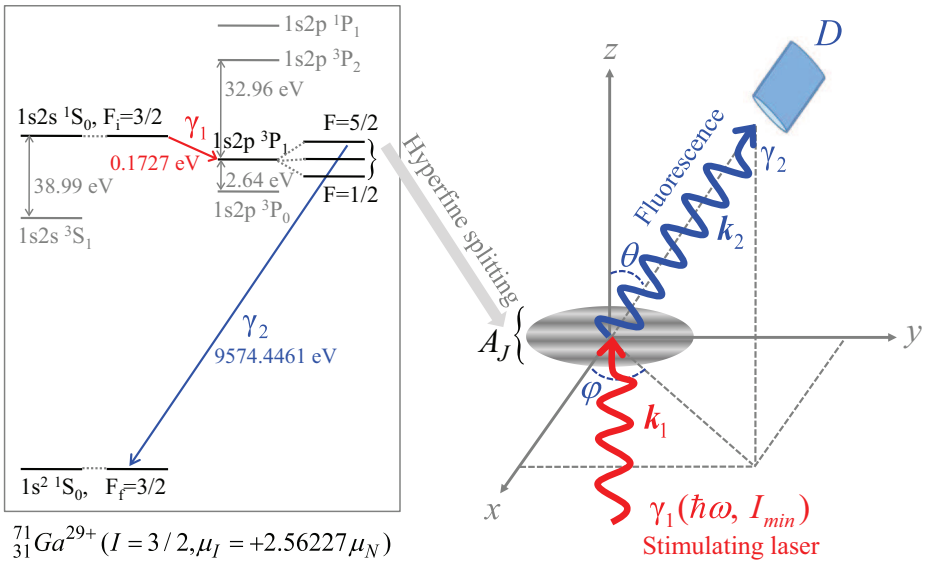

Figure 6.1: Level scheme of low-lying fine- and hyperfine-structure levels in heliumlike $^{71}_{31}\mathrm{Ga}^{29+}$ ($I = 3/2$, $\mu_I = +2.56227\,\mu_N$) ions and the geometry for the two-step radiative decay. While the first-step decay is stimulated by a laser beam with γ_1 photon energy $\hbar\omega$ and minimum intensity I_{min}, the second-step one occurs spontaneously with the emission of fluorescence γ_2 photons.

which is obtained by transforming I-J coupled atomic basis to uncoupled ones. Once the transition amplitude (6.5) is attained, the decay rate of individual hyperfine-resolved transitions and thus the linewidth of excited hyperfine levels can be readily determined. For electric-dipole transitions as considered in the following, for example, such a decay rate reads [137]

$$A_{if} = \frac{2.02613 \times 10^{18}}{(2F_i + 1)\,\lambda_{if}^3} \left| \left\langle F_f \left\| \sum\nolimits_m \boldsymbol{\alpha}_m \boldsymbol{a}_1^1(\boldsymbol{r}_m) \right\| F_i \right\rangle \right|^2 , \tag{6.6}$$

where A_{if} is in units of s^{-1}, the transition wavelength λ_{if} is in Å, and the amplitude is dimensionless. Moreover, the linewidth of a particular hyperfine level $|i\rangle$ is given by $\Gamma_i = 6.582 \times 10^{-16} \sum_f A_{if}$, in which Γ_i is given in eV and the summation runs over all possible radiative and non-radiative decay channels.

To evaluate the second-order amplitudes (6.4), apart from the hyperfine-resolved amplitudes (6.5) and the (natural) linewidth Γ_F, one still needs to know hyperfine transition energies. Since the electric-quadrupole hyperfine interactions are negligibly small throughout the isoelectronic sequence of heliumlike ions when compared

with the nuclear magnetic-dipole ones [126], they are not taken into account here. In this case, the hyperfine splitting of a fine-structure level αJ is given by

$$\Delta E^{\rm hf}_{\alpha JIF} = A_{\alpha J} \cdot K_{JIF} \,/\, 2 \tag{6.7}$$

in terms of $K_{JIF} = F(F{+}1){-}I(I{+}1){-}J(J{+}1)$ and the hyperfine constant $A_{\alpha J}$ [137]. Therefore, the hyperfine energy E_F in Equation (6.4) reads as $E_F = E_{\alpha J} + \Delta E^{\rm hf}_{\alpha JIF}$, in which $E_{\alpha J}$ is the energy of the corresponding fine-structure level. As seen from Equation (6.7), once the hyperfine constant is determined, the associated hyperfine splitting becomes known.

6.2.2 Density matrix of emitted spontaneous decay photons

As the second-order transition amplitudes (6.4) 'connects' the initial and final states of the (combined) stimulated plus spontaneous decay of the ions, one can naturally write down the (spin) density matrix of the emitted fluorescence γ_2 photons in terms of these transition amplitudes and the density matrix of the γ_1 photons [47, 69]. If the initial state of the ions is assumed to be unpolarized and the final state remains unobserved in the measurements, this density matrix is given as follows [135],

$$\langle \hat{\boldsymbol{k}}_2, \lambda_2 | \rho_{\gamma_2} | \hat{\boldsymbol{k}}_2, \lambda_2^{'} \rangle = \hat{J}_i^{\,-2} \sum_{M_i, M_f} \sum_{\lambda_1 \lambda_1^{'}} \mathcal{M}^{\lambda_1, \lambda_2}_{M_i, M_f}(\hbar\omega)\, \mathcal{M}^{\lambda_1^{'}, \lambda_2^{'}\,*}_{M_i, M_f}(\hbar\omega) \langle \hat{\boldsymbol{k}}_1, \lambda_1 | \rho_{\gamma_1} | \hat{\boldsymbol{k}}_1, \lambda_1^{'} \rangle. \tag{6.8}$$

Here, $\hat{J}_i \equiv \sqrt{2J_i + 1}$. As can be seen from this equation, for given ionic systems the density matrix (6.8) just depends on the polarization of the stimulating laser beam that consists of the γ_1 photons, as characterized generally by Equation (2.15).

If the stimulating laser is assumed to be unpolarized, which is the case considered here, this density matrix can be simplified further to be [135]

$$\begin{aligned} &\langle \hat{\boldsymbol{k}}_2, \lambda_2 | \rho_{\gamma_2} | \hat{\boldsymbol{k}}_2, \lambda_2^{'} \rangle \\ &= \frac{1}{2(2J_i + 1)} \sum_{M_i, M_f} \Big[\mathcal{M}^{1, \lambda_2}_{M_i, M_f}(\hbar\omega)\, \mathcal{M}^{1, \lambda_2^{'}\,*}_{M_i, M_f}(\hbar\omega) + \mathcal{M}^{-1, \lambda_2}_{M_i, M_f}(\hbar\omega)\, \mathcal{M}^{-1, \lambda_2^{'}\,*}_{M_i, M_f}(\hbar\omega) \Big]. \end{aligned} \tag{6.9}$$

Since both the angular distribution and degree of (linear and circular) polarization of an individual photon are fully determined by its spin density matrix [47, 48], we are ready now to analyze these angular and polarization properties for the emitted characteristic γ_2 fluorescence photons.

6.2.3 Angular distribution and polarization parameters

If, for instance, the polarization of the fluorescence γ_2 photons is unobserved, their angular distribution follows simply from the trace of the density matrix (6.9),

$$\sigma(\hat{\boldsymbol{k}}_2) = \langle \hat{\boldsymbol{k}}_2, \lambda_2 = +1 | \rho_{\gamma_2} | \hat{\boldsymbol{k}}_2, \lambda_2' = +1 \rangle + \langle \hat{\boldsymbol{k}}_2, \lambda_2 = -1 | \rho_{\gamma_2} | \hat{\boldsymbol{k}}_2, \lambda_2' = -1 \rangle . \quad (6.10)$$

Since the initial state of the stimulated plus spontaneous decay (6.1) and the stimulating laser have been assumed to be unpolarized, the emission of the fluorescence γ_2 photons is azimuthally symmetric. Therefore, the associated γ_2 angular distribution (6.10) is independent of the azimuthal angle φ and, hence, can be parameterized by a single anisotropy parameter within the dipole approximation,

$$\sigma(\theta) = \frac{\sigma_0}{4\pi} \left[1 + \beta \, P_2(\cos\theta) \right] . \quad (6.11)$$

In this parameterization, σ_0 denotes (overall) 4π-integrated photon emission intensity, and $P_2(\cos\theta)$ is the second-order Legendre polynomial as a function of the polar angle θ with respect to the quantization z axis.

Apart from the angular distribution, the density matrix (6.9) can be also used to give rise to the polarization of emitted fluorescence photons. As usual in atomic and optical physics, the linear polarization is characterized by two Stokes parameters P_1 and P_2. The parameter $P_1 = (I_{0^\circ} - I_{90^\circ})/(I_{0^\circ} + I_{90^\circ})$, for instance, is determined by the intensities of the emitted fluorescence photons linearly polarized in parallel (I_{0°) or perpendicular (I_{90°) with regard to the plane as defined by the propagation directions of the γ_1 and γ_2 photons. As discussed above, of course, the parameter P_1 can be expressed also in terms of the density matrix (6.9) as follows,

$$P_1(\hat{\boldsymbol{k}}_2) = \frac{\langle \hat{\boldsymbol{k}}_2, \lambda_2 = +1 | \rho_{\gamma_2} | \hat{\boldsymbol{k}}_2, \lambda_2' = -1 \rangle + \langle \hat{\boldsymbol{k}}_2, \lambda_2 = -1 | \rho_{\gamma_2} | \hat{\boldsymbol{k}}_2, \lambda_2' = +1 \rangle}{\langle \hat{\boldsymbol{k}}_2, \lambda_2 = +1 | \rho_{\gamma_2} | \hat{\boldsymbol{k}}_2, \lambda_2' = +1 \rangle + \langle \hat{\boldsymbol{k}}_2, \lambda_2 = -1 | \rho_{\gamma_2} | \hat{\boldsymbol{k}}_2, \lambda_2' = -1 \rangle} . \quad (6.12)$$

With the use of Eqs. (6.10)–(6.12), one can readily study the angular and polarization properties of these characteristic fluorescence γ_2 photons and explore how they are affected by the hyperfine level splitting of the intermediate resonances.

6.3 Results and discussion

Formulae (6.4)–(6.12) can be applied, of course, to the proposed $1s2s\ {}^1S_0, F_i = I + \gamma_1 \to 1s2p\ {}^3P_1, F = I-1, I, I+1 \to 1s^2\ {}^1S_0, F_f = I+\gamma_2$ stimulated plus spontaneous

decay of highly charged heliumlike ions. Once the second-order transition amplitudes (6.4) are evaluated for this particular decay process, they can be employed to obtain the spin density matrix of the γ_2 photons and hence further to explore the effect of the (intermediate) hyperfine splittings on their angular and polarization properties. Here, these transition amplitudes are calculated in the framework of perturbation theory including first-order interelectronic-interaction corrections, see Ref. [138] for details. Moreover, we here state clearly again that the stimulating laser photons γ_1 are assumed to be unpolarized and that the E1 approximation of the radiation fields is applied.

6.3.1 Laser intensities required for the stimulated decay

Table 6.1 displays several selected isotopes with nuclear charge $31 \leq Z \leq 83$ which will be considered below [95]. For the $1s2p\ ^3P_1$ level of their corresponding heliumlike ions, the presently calculated hyperfine constants A_J and natural linewidths Γ_F are tabulated. Moreover, the transition energies of the fine-structure $1s2s\ ^1S_0 \rightarrow 1s2p\ ^3P_1$ and $1s2p\ ^3P_1 \rightarrow 1s^2\ ^1S_0$ decays are taken from Ref. [139]. The respective linewidths of the $1s2p\ ^3P_1, F = I-1, I, I+1$ hyperfine levels remain the same as each other and also as the one for the corresponding fine-structure level $1s2p\ ^3P_1$ of heliumlike ions with $I = 0$. This is because the $1s2p\ ^3P_1$ hyperfine splittings are negligibly small when compared to the transition energy of the $1s2p\ ^3P_1 \rightarrow 1s^2\ ^1S_0$ decay. As discussed above, moreover, in order to compete with dominant 2E1 decay of the initial $1s2s\ ^1S_0, F_i = I$ level, suitable intensities of the stimulating laser beam are required to dominate the first-step decay. For this reason, let us consider the decay rate $W_{2\,^1S_0 \rightarrow 2\,^3P_1}$ of the $1s2s\ ^1S_0 \rightarrow 1s2p\ ^3P_1$ transition when it is stimulated by the laser. It has been known that this stimulated decay rate is proportional to the corresponding spontaneous decay rate $A_{2\,^1S_0 \rightarrow 2\,^3P_1}$ and the used laser intensity $\mathcal{I}$, to be more specific, which is given by [140]

$$W_{2\,^1S_0 \rightarrow 2\,^3P_1} = \frac{3}{4\pi^2} \frac{A_{2\,^1S_0 \rightarrow 2\,^3P_1}}{\Gamma_{2\,^1S_0}} \lambda^3_{2\,^1S_0 \rightarrow 2\,^3P_1} \mathcal{I}\,. \tag{6.13}$$

Here, $\Gamma_{2\,^1S_0}$ is the natural linewidth of the $1s2s\ ^1S_0$ level, and $\lambda_{2^1S_0 \rightarrow 2\ ^3P_1}$ is the associated transition wavelength. Take heliumlike $^{71}_{31}\mathrm{Ga}^{29+}$ for example: $A_{\ 2\ ^1S_0 \rightarrow 2\ ^3P_1} = 5.22 \times 10^1\ \mathrm{s}^{-1}$, $\Gamma_{\ 2\ ^1S_0} = \hbar(A_{\ 2\ ^1S_0 \rightarrow 2\ ^3P_1} + A_{\ 2\ ^1S_0 \rightarrow 2\ ^3S_1} + A_{\ 2\ ^1S_0 \rightarrow 1\ ^1S_0}) = 7.96 \times 10^{-6}$ eV, and $\lambda_{\ 2\ ^1S_0 \rightarrow 2\ ^3P_1} = 7.18 \times 10^4$ Å. By operating these data, numerically, we obtain $W_{\ 2\ ^1S_0 \rightarrow 2\ ^3P_1}(\mathrm{s}^{-1}) = 3.84 \times 10^4 \mathcal{I}$, where the intensity $\mathcal{I}$ is in $\mathrm{W/cm}^2$.

Table 6.1: Table of isotopes with nuclear spin I and magnetic dipole moment μ_I in units of the nuclear magneton μ_N considered. While the hyperfine constant A_J (eV) and natural linewidth Γ (eV) of the level $1s2p\ ^3P_1$ of their corresponding heliumlike ions are presently calculated, the transition energies (eV) of both $1s2s\ ^1S_0 \to 1s2p\ ^3P_1$ (1st-step) and $1s2p\ ^3P_1 \to 1s^2\ ^1S_0$ (2nd-step) decays are taken from Ref. [139]. Moreover, minimum intensities $\mathcal{I}_{\rm min}$ (W/cm^2) of the stimulating laser are estimated.

${}^A_Z X$	I	μ_I	$A_J(2\,^3P_1)$	$\Gamma_{2\,^3P_1,F}$	$\triangle E_{\rm 1st-step}$	$\triangle E_{\rm 2nd-step}$	$\mathcal{I}_{\rm min}$
${}^{71}_{31}\mathrm{Ga}^{29+}$	3/2	+2.56227	0.0278	0.1026	0.1727	9574.4461	3.15×10^5
${}^{141}_{59}\mathrm{Pr}^{57+}$	5/2	+4.2754	0.2573	2.9606	12.461	36391.292	2.96×10^9
${}^{209}_{83}\mathrm{Bi}^{81+}$	9/2	+4.1103	0.5457	12.815	63.961	76131.359	3.64×10^{11}

The condition that the stimulated $1s2s\ ^1S_0 \to 1s2p\ ^3P_1$ decay occurs faster than the 2E1 decay gives rise to $W_{2\ ^1S_0 \to 2\ ^3P_1} > A_{2\ ^1S_0 \to 1\ ^1S_0} = 1.21\times10^{10}$ s^{-1}, from which one can readily obtain required laser intensities $\mathcal{I} \geq \mathcal{I}_{min} = 3.15\times10^5$ W/cm^2. For heliumlike ${}^{141}_{59}\mathrm{Pr}^{57+}$ and ${}^{209}_{83}\mathrm{Bi}^{81+}$ ions, moreover, such minimum intensities are also estimated and given in Table 6.1. These intensities are easily accessible with present-day laser sources.

6.3.2 Angular distribution and polarization of the spontaneous decay photons

Since both the angular distribution (described by the so-called anisotropy parameter) and linear polarization of photons are characterized fully by their density matrix, we are now ready to analyze these angle-resolved properties for the fluorescence γ_2 photons with the use of Eqs. (6.10)–(6.12). Figure 6.2 displays the anisotropy parameter β and the degree of linear polarization P_1 for the fluorescence γ_2 photons emitted from the (second-step) transitions $1s2p\ ^3P_1, F = 1/2, 3/2, 5/2 \to 1s^2\ ^1S_0, F_f = 3/2$ of heliumlike ions ${}^{71}_{31}\mathrm{Ga}^{29+}$ ($I = 3/2$, $\mu_I = +2.56227\,\mu_N$), as functions of photon energy $\hbar\omega$ of the stimulating laser. Results are shown for the actual hyperfine constant $A_J = 0.0271$ eV that is calculated presently as well as for two assumed ones $0.8A_J$ and $1.2A_J$. Moreover, the polarization P_1 is predicted for the γ_2 photons emitted perpendicular to the incident stimulating laser beam, i.e., at $\theta = 90°$.

As can be seen from this figure, both the anisotropy parameter (angular distribution) and the linear polarization depend strongly upon the hyperfine constant A_J, especially, at stimulating γ_1 photon energies near the resonances, say, $\hbar\omega \simeq 0.17$ eV. The polarization P_1, for instance, changes from -0.39 for $A_J = 0.0278$ eV to -0.51

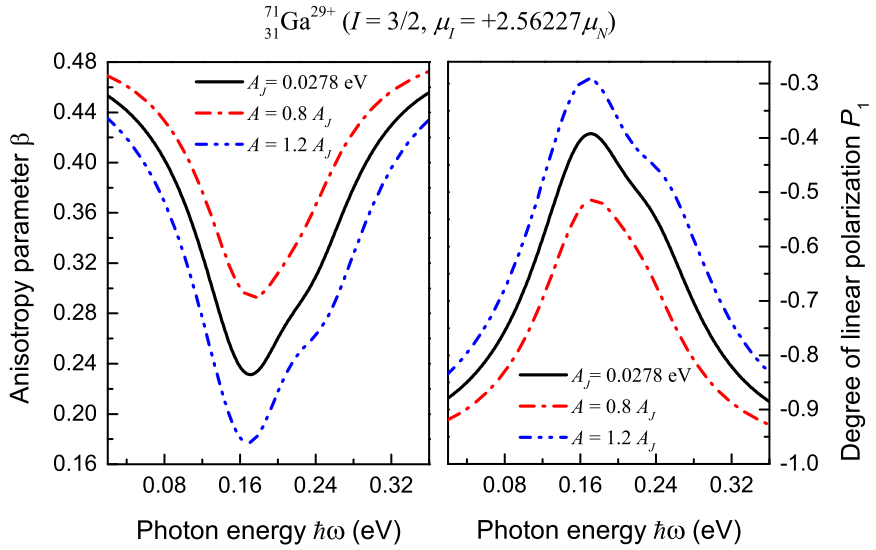

Figure 6.2: Anisotropy parameter β (left panel) and degree of linear polarization P_1 (right panel) of the hyperfine $1s2p\ ^3P_1, F = 1/2, 3/2, 5/2 \rightarrow 1s^2\ ^1S_0, F_f = 3/2$ fluorescence emissions from heliumlike $^{71}_{31}Ga^{29+}$ ($I = 3/2$, $\mu_I = +2.56227\,\mu_N$) ions as functions of photon energy $\hbar\omega$ of the incident light γ_1. Results are shown for the calculated hyperfine constant $A_J = 0.0278$ eV (black solid lines) as given in Table 6.1 and also for two assumed values, $0.8A_J$ (red dash-dotted lines) and $1.2A_J$ (blue dash-dot-dotted lines), which differ by just 20%.

for $0.8A_J$, which is large enough to be observed with present-day x-ray photon detectors [70, 81, 132]. This strong dependence on the hyperfine constant could be a clear and promising "signature" for the determination of hyperfine splittings in highly charged ions. Actually, a different attempt has been made by Henderson *et al.* for the same purpose also by measuring associated photon polarization. [36]. Moreover, for a given hyperfine constant, both of the angular and polarization behaviors appear to be very sensitive to the γ_1 photon energy. While the emitted γ_2 photons possess the weakest anisotropy and polarization near the resonances, they become promptly more and more anisotropic and linearly polarized when the γ_1 photon energy deviates from the resonances. This dependence and sensitivity arise from non-negligible linewidths of the (partially) overlapping resonances $1s2p\ ^3P_1, F = 1/2, 3/2, 5/2$, which leads to a coherence transfer in the population of these resonances during the stimulated (first-step) decay and, ultimately, influences the angular and polarization behaviors of the spontaneously emitted (second-step) γ_2 photons.

Apart from low-Z heliumlike ions like $^{71}_{31}Ga^{29+}$, we will also consider intermediate

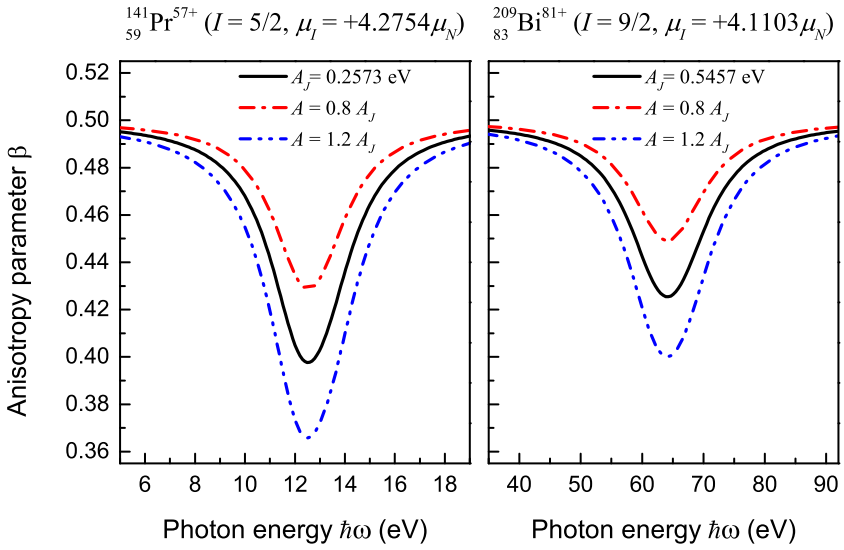

Figure 6.3: Anisotropy parameter of the hyperfine $1s2p\ ^3P_1, F = 3/2, 5/2, 7/2 \rightarrow 1s^2\ ^1S_0, F_f = 5/2$ and $1s2p\ ^3P_1, F = 7/2, 9/2, 11/2 \rightarrow 1s^2\ ^1S_0, F_f = 9/2$ fluorescence emissions from heliumlike $^{141}_{59}Pr^{57+}$ ($I = 5/2$, $\mu_I = +4.2754\,\mu_N$; left panel) and $^{209}_{83}Bi^{81+}$ ($I = 9/2$, $\mu_I = +4.1103\,\mu_N$; right panel) ions, respectively, as functions of photon energy $\hbar\omega$ of the incident light γ_1. Results are shown for the calculated hyperfine constant $A_J = 0.2573$ eV and 0.5457 eV (black solid lines), respectively, and also for two assumed values, $0.8A_J$ (red dash-dotted lines) and $1.2A_J$ (blue dash-dot-dotted lines) each, which differ by just 20%.

and high-Z ions such as $^{141}_{59}Pr^{57+}$ ($I = 5/2$, $\mu_I = +4.2754\,\mu_N$) and $^{209}_{83}Bi^{81+}$ ($I = 9/2$, $\mu_I = +4.1103\,\mu_N$). For these ions, the corresponding γ_2 angular and polarization dependence remains still prominent on the $1s2p\ ^3P_1, F = I - 1, I, I + 1$ hyperfine splittings and also on the γ_1 photon energy, as clearly shown in Figure 6.3 for the anisotropy parameter β and in Figure 6.4 for the linear polarization P_1, respectively, although it becomes weak when compared to the case of $^{71}_{31}Ga^{29+}$ ions. This is because such a dependence results from the linewidth of the intermediate hyperfine resonances as discussed above, which reaches its maximum when the hyperfine splitting becomes the same as the linewidth in magnitude. While the linewidth goes rapidly from 0.10 eV for $^{71}_{31}Ga^{29+}$ to 12.82 eV for $^{209}_{83}Bi^{81+}$, the corresponding hyperfine splitting changes just from 0.11 eV to 5.46 eV, even for the selected stable isotopes with the biggest nuclear magnetic dipole moment.

The measurements on the characteristic fluorescence γ_2 emission $1s2p\ ^3P_1, F = I - 1, I, I + 1 \rightarrow 1s^2\ ^1S_0, F_f = I$ of heliumlike ions are feasible with present-day

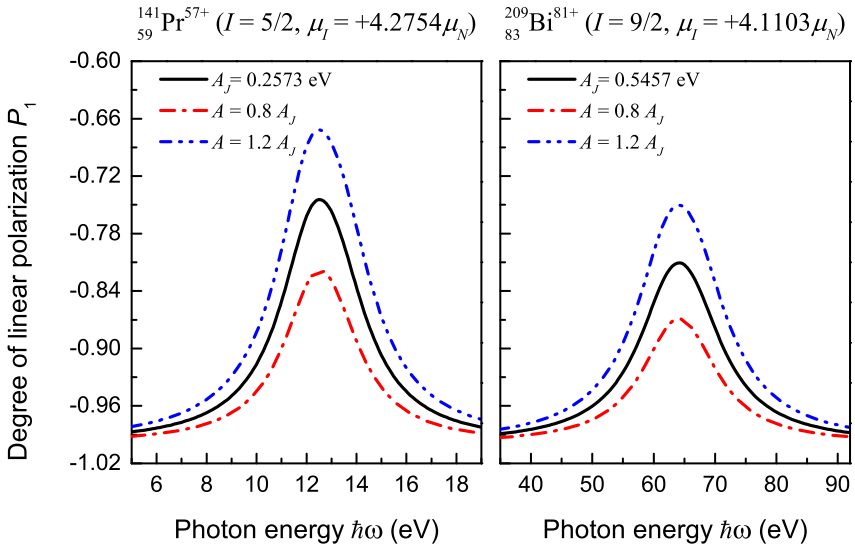

Figure 6.4: The same as Figure 6.3 but for the degree of linear polarization P_1.

experimental facilities and techniques, for instance, at the heavy-ion storage rings or electron-beam ion traps. At the GSI storage ring, for instance, a combined angular distribution and polarization measurement of the Ly-α_1 fluorescence photons emitted following the radiative electron capture into initially bare uranium ions has been performed to determine the magnetic-quadrupole contribution to the $2p_{3/2} \to 1s_{1/2}$ transition in hydrogenlike ions [39]. As seen from the simulated results as presented in Figs. 6.2–6.4, this proposed experimental scheme of measuring photon polarization and/or angular distribution could allow a direct determination of hyperfine splittings in highly charged ions.

7 Summary & Outlook

In the present thesis, we have performed a series of theoretical studies on angular correlation and linear polarization of (characteristic) x-ray fluorescence photons emitted from excited highly charged ions. As well known, these angle-resolved properties have been found much more sensitive with respect to the details of electron-electron, electron-nuclei, and electron-photon interactions than total (radiative) decay rates [32, 37, 39]. These studies were motivated by such a sensitivity and thus further by the intention to explore various weak interaction effects in atomic physics by analyzing these angle-resolved observables. It was expected that these angle-resolved properties of fluorescence photons could be used as an effective tool, for instance, to determine nuclear parameters of isotopes or to resolve (small) fine- and hyperfine-structure level splittings in highly charged ions, as considered in the thesis. In order to do this, a particular formalism was developed for each of the case studies within the framework of density matrix theory [47] and the MCDF method [62]. Our expectations as proposed above were confirmed by the present simulation results obtained with the use of the developed formalism.

To be summarized in more detail, we first started this thesis with a brief introduction in Chapter 1, in which existing studies on the angular distribution and polarization of x-ray photons emitted from highly charged ions were briefly reviewed. While the present work focused on the theoretical simulations, we also discussed how these photon angular distribution and polarization studies have been performed experimentally, for instance, at ion storage rings or at electron beam ion traps.

In Chapter 2 we outlined a theoretical framework of the present work — density matrix theory. It was started with a discussion on the most fundamental concepts of the theory, i.e., pure and mixed states. Such a discussion was essential as the density matrix theory has been developed to characterize mixed states, which is in contrast to a state vector (or wave function) description of pure states in quantum physics. From this discussion of mixed states we naturally introduced the concepts of (spin) density matrix and corresponding statistical tensors. As particular examples, the spin density matrix of free electrons, atomic bound states, and individual photons were specially discussed, which would be "building blocks" of developing theoretical formalism for the subsequent case studies. On the basis of these spin density matrix and statistical tensors, in addition, a time-independent description was introduced

for "atomic transitions" in electron-atom collisions or in photon-atom interactions. Thereafter, we applied this time-independent description to two particular transition processes — production and (radiative) decay of polarized atomic or ionic states — simply as an example to demonstrate how such an application could be performed in practice. We then discussed how angular distribution and polarization of emitted fluorescence photons can be expressed in terms of initial alignments of atoms or ions. Since the density matrix (or statistical tensors) of initial- and final-state ensembles of a particular atomic transition are "connected" by so-called transition amplitudes in the time-independent description, we ended this chapter with a brief review on the MCDF method, based on which all necessary transition amplitudes used in the following case studies have been calculated.

Up to then, we had presented the necessary theoretical basis and hence had been ready to carry out case studies on photon polarization and/or angular distribution following particular atomic or ionic excitation processes. Therefore, we studied the linear polarization of the characteristic transition lines $Ly\text{-}\alpha_1$ ($3d_{5/2} \rightarrow 2p_{3/2}$) and $Ly\text{-}\alpha_2$ ($3d_{3/2} \rightarrow 2p_{3/2}$) following inner-shell photoionization of tungsten by an unpolarized photon beam, as discussed in Chapter 3. This was motivated by a comparison with existing experimental measurements on the same physical observables in order to demonstrate the validity of the theoretical basis as presented in Chapter 2. It was found that the presently calculated linear polarizations for both the lines show a very weak dependence upon the ionizing photon energy in the considered range of 10–23 keV. While the $Ly\text{-}\alpha_1$ line shows a positive linear polarization and it changes between +1% and +2% within the photon energy range, the $Ly\text{-}\alpha_2$ polarization possesses a negative sign and changes in the range –5% $\sim$ –7%. The linear polarization was determined in experiment to be $+(1.6\pm0.5)\%$ and $-(7.0\pm2.0)\%$ for the $Ly\text{-}\alpha_{1,2}$ lines, respectively, which are in good agreements with the present theoretical values within the given uncertainties.

With this successful comparison that gave rise to good agreements, in Chapter 4 we further investigated angular emission properties of the characteristic $K\alpha_1$ x-ray photons following the REC into excited levels $1s2p_{3/2}\ ^{1,3}P_{1,2}$ of (finally) heliumlike ions with nonzero nuclear spin ($I \neq 0$). In particular, we tried to understand the question of how the hyperfine interactions of the magnetic moment of the nucleus with those of the electrons influence the (hyperfine- and fine-structure averaged) $K\alpha_1$ angular emission. For that purpose, detailed computations within the density matrix formalism and the MCDF method had been performed for selected ions Sn^{48+}, Xe^{52+},

and Tl^{79+}. From these computations a sizable effect of the hyperfine interaction on the overall $K\alpha_1$ angular emission was found especially for those isotopes with nuclear spin $I = 1/2$ and large nuclear magnetic moment, while this effect is remarkably suppressed for most isotopes that have nuclear spin $I > 1/2$. Therefore, we suggested that accurate measurements of the $K\alpha_1$ angular distribution at ion storage rings might be used as an independent tool for probing nuclear parameters such as the magnetic dipole moment of radioactive or rare stable isotopes with $I \geq 1/2$.

Apart from the characteristic x-ray emissions from isolated atomic or ionic levels as discussed in the previous chapters, in the subsequent content we turned our attention to another interesting topic — fluorescence photon emissions from (partially) overlapping resonances of atoms or ions. In Chapter 5 the photon polarization and angular distribution as well as the photon-photon angular correlation were studied for characteristic fluorescence photons emitted from two-step radiative cascades that proceed via overlapping resonances of highly charged ions. With such a study we intended to answer two practical questions: (i) how level splittings of these overlapping resonances affect the emission of characteristic fluorescence photons; (ii) whether or not these level splittings can be determined by measuring the angular and polarization properties of the emitted photons. To account for the role of the overlapping resonances, a lifetime-induced depolarization factor was introduced. As a particular example, the radiative cascade $1s2p^2\ J_i = 1/2,\ 3/2 \to 1s2s2p\ J = 1/2,\ 3/2 + \gamma_1 \to 1s^22s\ J_f = 1/2 + \gamma_1 + \gamma_2$ of lithiumlike ions was explored by using the presently developed density matrix formalism. These ions have a relatively simple level structure and display a level crossing of the two intermediate $1s2s2p\ J = 1/2, 3/2$ resonances among $74 \leq Z \leq 79$. For this cascade, with increasing level splitting $\Delta\omega$ especially at small ones $\Delta\omega \lesssim 0.2$ a.u. ≈ 5.4 eV, a remarkably strong depolarization effect associated with finite lifetimes of the intermediate resonances was found for the γ_1–γ_2 angular correlation as well as for the γ_2 angular distribution and polarization. From this theoretical analysis, we concluded that accurate angle- or polarization-resolved x-ray measurements may help determine (tiny) level splittings of overlapping resonances in excited highly charged ions.

As it was motivated by the previous studies, in Chapter 6 we proposed a novel experimental scheme to determine hyperfine splittings in highly charged heliumlike ions by measuring angle-resolved observables such as photon angular distribution and linear polarization. In particular, we studied the stimulated plus spontaneous $1s2s\ {}^1S_0, F_i = I + \gamma_1 \to 1s2p\ {}^3P_1, F = I - 1, I, I + 1 \to 1s^2\ {}^1S_0, F_f = I + \gamma_2$

radiative decay for selected isotopes $^{71}_{31}\mathrm{Ga}^{29+}$, $^{141}_{59}\mathrm{Pr}^{57+}$, and $^{209}_{83}\mathrm{Bi}^{81+}$. By analyzing the emitted characteristic γ_2 photon, it was found that its angular and polarization properties depend strongly on the intermediate $1s2p\,^3P_1, F = I-1, I, I+1$ hyperfine splittings. This dependence could be a promising "signature" for the determination of the hyperfine splittings in highly charged heliumlike ions.

For these angular distribution and/or polarization studies of characteristic fluorescence photons as proposed in the present thesis, it is feasible nowadays to perform corresponding experimental measurements. To be more specific, they can be carried out at heavy-ion storage ring or electron beam ion trap facilities by using present-day Bragg crystal spectrometers and photon detection techniques [70, 81, 132], just as achieved for the $Ly\text{-}\alpha_{1,2}$ emission lines in Chapter 3 and also for many other examples such as in Refs. [32, 39].

As one might notice that in the implemented case studies all of involved photon beams have been assumed to be unpolarized, such as the ionizing photon beam used in Chapter 3 and the stimulating beam in Chapter 6. Admittedly, the utilization of polarized photon beams in these studies may change or even enhance the obtained angular and polarization dependences of the emitted fluorescence photons. This can be seen, for instance, from the polarization transfer studies in the inner-shell photoionization of sodiumlike ions [54] and also in the Rayleigh scattering of hard x-rays [45]. As a matter of fact, with the use of modern laser facilities or synchrotron radiation sources such as the PETRA III at DESY, one can produce nearly 100% linearly polarized light beams [45]. Moreover, polarization impurities of the beams could be accurately diagnosed by means of Rayleigh scattering process and hence might be well tuned for different purposes. For this reason, applications of these light beams to the photon angular distribution and polarization studies as presented in the thesis are therefore expected to be a promising attempt.

Apart from discussing the light (or photon) beams utilized potentially in future studies, which generally affect the population of excited states in photon-atom/ion interactions and thus ultimately the angular and polarization properties of emitted fluorescence photons, of course, the detection of these photons is also very important in such studies. With state-of-the-art channel-cut silicon crystal polarimeters [46], the polarization of x-ray photons could be measured with extremely high accuracy. For instance, this accuracy has reached a level of $\sim 10^{-10}$ for the polarization purities and of ~ 1 arcsec for rotations of the corresponding polarization plane [141]. When relying on a more accurate theory, applications of such a high-precision x-

ray polarimeter to the case study as presented in Chapter 6 could serve as a probe of QED in the presence of strong Coulomb fields generated by few-electron heavy nuclei. This might be another promising attempt in the future.

Bibliography

[1] W. C. Röntgen. "Über eine neue Art von Strahlen". In: *Secretary of the Physical-Medical Society, Würzburg* (1895).

[2] W. C. Röntgen. "On a New Kind of Rays". In: *Nature* **53** (1896), p. 274. DOI: doi:10.1038/053274b0.

[3] P Beiersdorfer. "A "brief" history of spectroscopy on EBIT". In: *Can. J. Phys.* **86** (2008), p. 1. DOI: 10.1139/p07-135.

[4] C. Biedermann et al. "First results from the Berlin EBIT". In: *Phys. Scr.* **1997** (1997), p. 360. URL: http://stacks.iop.org/1402-4896/1997/i=T73/a=118.

[5] J. D. Gillaspy. "First results from the EBIT at NIST". In: *Phys. Scr.* **1997** (1997), p. 99. URL: http://stacks.iop.org/1402-4896/1997/i=T71/a=017.

[6] C. H. Skinner. "Applications of EBIT to magnetic fusion diagnostics". In: *Can. J. Phys.* **86** (2008), p. 285. DOI: 10.1139/p07-100.

[7] U. Kentsch et al. "Dresden EBIT: Results and perspectives". In: *Rev. Sci. Instrum.* **73** (2002), p. 660. DOI: 10.1063/1.1429311.

[8] N Nakamura et al. "An overview of the Tokyo electron beam ion trap". In: *Phys. Scr.* **1997** (1997), p. 362. URL: http://stacks.iop.org/1402-4896/1997/i=T73/a=119.

[9] H. Watanabe et al. "Characteristics of the Tokyo Electron-Beam Ion Trap". In: *J. Phys. Soc. Jpn.* **66** (1997), p. 3795. DOI: 10.1143/JPSJ.66.3795.

[10] M. Steck et al. "Electron cooling experiments at the ESR". In: *Nucl. Instr. Meth. Phys. Res. A* **532** (2004), p. 357. DOI: http://dx.doi.org/10.1016/j.nima.2004.06.065.

[11] T. Kandler, P. Mokler, and T. Stöhlker. "A case study for charge state breeding of heavy ions in the storage ring, ESR". In: *Nucl. Instr. Meth. Phys. Res. B* **107** (1996), p. 357. DOI: http://dx.doi.org/10.1016/0168-583X(95)00839-X.

[12] P. Mokler and T. Stöhlker. "The Physics of Highly Charged Heavy Ions Revealed by Storage/Cooler Rings". In: ed. by B. Bederson and H. Walther. Vol. **37**. Adv. At. Mol. Opt. Phy. Academic Press, 1996, p. 297. DOI: http://dx.doi.org/10.1016/S1049-250X(08)60103-2.

[13] H. Poth. "Electron cooling: Theory, experiment, application". In: *Phys. Rep.* **196** (1990), p. 135. DOI: http://dx.doi.org/10.1016/0370-1573(90)90040-9.

[14] B. Franzke. "The heavy ion storage and cooler ring project ESR at GSI". In: *Nucl. Instr. Meth. Phys. Res. B* **24-25** (1987), p. 18. DOI: http://dx.doi.org/10.1016/0168-583X(87)90583-0.

[15] J Wykes. "The variation with electron scattering angle of the polarization of atomic line radiation excited by electron impact". In: *J. Phys. B* **5** (1972), p. 1126. URL: http://stacks.iop.org/0022-3700/5/i=6/a=015.

[16] P. J. Mohr, G. Plunien, and G. Soff. "QED corrections in heavy atoms". In: *Phys. Rep.* **293** (1998), p. 227. ISSN: 0370-1573. DOI: http://dx.doi.org/10.1016/S0370-1573(97)00046-X.

[17] A. Gumberidze et al. "Electron-Electron Interaction in Strong Electromagnetic Fields: The Two-Electron Contribution to the Ground-State Energy in He-like Uranium". In: *Phys. Rev. Lett.* **92** (2004), p. 203004. DOI: 10.1103/PhysRevLett.92.203004.

[18] A. Gumberidze. "Experimental Studies of the Ground State QED Corrections in H- and He-like Uranium". PhD thesis. Goethe University Frankfurt, 2003.

[19] S. Tashenov. "Hard x-ray polarimetry with position sensitive germanium detectors – studies of the recombination transitions into highly charged ions". PhD thesis. Goethe University Frankfurt, 2005.

[20] S. Zakowicz, W. Scheid, and N. Grün. "Angular distribution and correlation of photons emitted during dielectronic recombination into hydrogen-like ions". In: *Nucl. Instr. Meth. Phys. Res. B* **205** (2003), p. 386. ISSN: 0168-583X. DOI: http://dx.doi.org/10.1016/S0168-583X(02)01960-2.

[21] E. G. Berezhko and N. M. Kabachnik. "Theoretical study of inner-shell alignment of atoms in electron impact ionisation: angular distribution and polarisation of X-rays and Auger electrons". In: *J. Phys. B* **10** (1977), p. 2467. URL: http://stacks.iop.org/0022-3700/10/i=12/a=025.

[22] M. Gail, N. Grün, and W. Scheid. "Angular distribution of radiation emitted after resonant transfer and excitation". In: *J. Phys. B* **31** (1998), p. 4645. URL: http://stacks.iop.org/0953-4075/31/i=20/a=021.

[23] J. Eichler and A. Ichihara. "Polarization of photons emitted in radiative electron capture by bare high-Z ions". In: *Phys. Rev. A* **65** (2002), p. 052716. DOI: 10.1103/PhysRevA.65.052716.

[24] H Schmoranzer et al. "Angular distribution of the fluorescence radiation of Kr II satellite states". In: *J. Phys. B* **30** (1997), p. 4463. URL: http://stacks.iop.org/0953-4075/30/i=20/a=010.

[25] A. Surzhykov et al. "Polarization studies on the radiative recombination of highly charged bare ions". In: *Phys. Rev. A* **68** (2003), p. 022710. DOI: 10.1103/PhysRevA.68.022710.

[26] G. Vassilev et al. "Measurements of Photon Polarization and Angular Correlations for He^+ -He Collisions Coincidence Technique Using an Ion-Photon". In: *Phys. Rev. Lett.* **34** (1975), p. 444. DOI: 10.1103/PhysRevLett.34.444.

[27] Z. W. Wu, C. Z. Dong, and J. Jiang. "Degrees of polarization of the two strongest $5f \rightarrow 3d$ lines following electron-impact excitation and dielectronic recombination processes of Cu-like to Se-like gold ions". In: *Phys. Rev. A* **86** (2012), p. 022712. DOI: 10.1103/PhysRevA.86.022712.

[28] M. H. Chen and K. J. Reed. "Relativistic effects on angular distribution of Auger electrons emitted from Be-like ions following electron-impact excitation". In: *Phys. Rev. A* **50** (1994), p. 2279. DOI: 10.1103/PhysRevA.50.2279.

[29] A. Surzhykov et al. "Lyman- α_1 Decay in Hydrogenlike Ions: Interference between the $E1$ and $M2$ Transition Amplitudes". In: *Phys. Rev. Lett.* **88** (2002), p. 153001. DOI: 10.1103/PhysRevLett.88.153001.

[30] S. Fritzsche, A. Surzhykov, and T. Stöhlker. "Dominance of the Breit Interaction in the X-Ray Emission of Highly Charged Ions Following Dielectronic Recombination". In: *Phys. Rev. Lett.* **103** (2009), p. 113001. DOI: 10.1103/PhysRevLett.103.113001.

[31] S Fritzsche et al. "Electron emission from highly charged ions: signatures of magnetic interactions and retardation in strong fields". In: *New J. Phys.* **14** (2012), p. 083018. URL: http://stacks.iop.org/1367-2630/14/i=8/a=083018.

[32] Z. Hu et al. “Experimental Demonstration of the Breit Interaction which Dominates the Angular Distribution of X-ray Emission in Dielectronic Recombination”. In: *Phys. Rev. Lett.* **108** (2012), p. 073002. DOI: 10.1103/PhysRevLett.108.073002.

[33] H. Jörg et al. “Linear polarization of x-ray transitions due to dielectronic recombination in highly charged ions”. In: *Phys. Rev. A* **91** (2015), p. 042705. DOI: 10.1103/PhysRevA.91.042705.

[34] C. Shah et al. “Polarization measurement of dielectronic recombination transitions in highly charged krypton ions”. In: *Phys. Rev. A* **92** (2015), p. 042702. DOI: 10.1103/PhysRevA.92.042702.

[35] N. Nakamura. “Breit interaction effect on dielectronic recombination of heavy ions”. In: *J. Phys. B* **49** (2016), p. 212001. URL: http://stacks.iop.org/0953-4075/49/i=21/a=212001.

[36] J. R. Henderson et al. “Polarization of x-ray emission lines from heliumlike scandium as a probe of the hyperfine interaction”. In: *Phys. Rev. Lett.* **65** (1990), p. 705. DOI: 10.1103/PhysRevLett.65.705.

[37] A. Surzhykov et al. “Hyperfine-induced effects on the linear polarization of $K\alpha_1$ emission from heliumlike ions”. In: *Phys. Rev. A* **87** (2013), p. 052507. DOI: 10.1103/PhysRevA.87.052507.

[38] Z. W. Wu, A. Surzhykov, and S. Fritzsche. “Hyperfine-induced modifications to the angular distribution of the $K\alpha_1$ x-ray emission”. In: *Phys. Rev. A* **89** (2014), p. 022513. DOI: 10.1103/PhysRevA.89.022513.

[39] G. Weber et al. “Direct Determination of the Magnetic Quadrupole Contribution to the Lyman-α_1 Transition in a Hydrogenlike Ion”. In: *Phys. Rev. Lett.* **105** (2010), p. 243002. DOI: 10.1103/PhysRevLett.105.243002.

[40] G Weber et al. “Combined linear polarization and angular distribution measurements of x-rays for precise determination of multipole-mixing in characteristic transitions of high- Z systems”. In: *J. Phys. B* **48** (2015), p. 144031. URL: http://stacks.iop.org/0953-4075/48/i=14/a=144031.

[41] R. E. Marrs, S. R. Elliott, and D. A. Knapp. “Production and Trapping of Hydrogenlike and Bare Uranium Ions in an Electron Beam Ion Trap”. In: *Phys. Rev. Lett.* **72** (1994), p. 4082. DOI: 10.1103/PhysRevLett.72.4082.

[42] T. Stöhlker et al. “Strong Alignment Observed for the Time-Reversed Photoionization Process Studied in Relativistic Collisions with Bare Uranium Ions”. In: *Phys. Rev. Lett.* **79** (1997), p. 3270. DOI: 10.1103/PhysRevLett.79.3270.

[43] T. Stöhlker et al. “Applications of position sensitive germanium detectors for X-ray spectroscopy of highly charged heavy ions”. In: *Nucl. Instr. Meth. Phys. Res. B* **205** (2003), p. 210. DOI: http://dx.doi.org/10.1016/S0168-583X(03)00557-3.

[44] F. Metzger and M. Deutsch. “A Study of the Polarization-Direction Correlation of Successive Gamma-Ray Quanta”. In: *Phys. Rev.* **78** (1950), p. 551. DOI: 10.1103/PhysRev.78.551.

[45] K.-H. Blumenhagen et al. “Polarization transfer in Rayleigh scattering of hard x-rays”. In: *New J. Phys.* **18** (2016), p. 103034. URL: http://stacks.iop.org/1367-2630/18/i=10/a=103034.

[46] B. Marx et al. “Determination of high-purity polarization state of X-rays”. In: *Opt. Commun.* **284** (2011), p. 915. DOI: http://dx.doi.org/10.1016/j.optcom.2010.10.054.

[47] V. V. Balashov, A. N. Grum-Grzhimailo, and N. M. Kabachnik. *Polarization and Correlation Phenomena in Atomic Collisions*. New York: Kluwer Academic, 2000. DOI: 10.1007/978-1-4757-3228-3.

[48] K. Blum. *Density matrix theory and applications; 3rd ed.* Berlin Heidelberg: Springer-Verlag, 2012. DOI: 10.1007/978-3-642-20561-3.

[49] J. von Neumann. “Wahrscheinlichkeitstheoretischer Aufbau der Quantenmechanik”. In: *Göttinger Nachrichten* (1927), p. 245. URL: http://eudml.org/doc/59230.

[50] U. Fano. “Description of States in Quantum Mechanics by Density Matrix and Operator Techniques”. In: *Rev. Mod. Phys.* **29** (1957), p. 74. DOI: 10.1103/RevModPhys.29.74.

[51] D. ter Haar. “Theory and applications of the density matrix”. In: *Rep. Prog. Phys.* **24** (1961), p. 304. URL: http://stacks.iop.org/0034-4885/24/i=1/a=307.

[52] Z. W. Wu, J. Jiang, and C. Z. Dong. "Influence of Breit interaction on the polarization of radiation following inner-shell electron-impact excitation of highly charged berylliumlike ions". In: *Phys. Rev. A* **84** (2011), p. 032713. DOI: 10.1103/PhysRevA.84.032713.

[53] S. Baier, A. N. Grum-Grzhimailo, and N. M. Kabachnik. "Angular distribution of photoelectrons in resonant photoionization of polarized atoms". In: *J. Phys. B* **27** (1994), p. 3363. URL: http://stacks.iop.org/0953-4075/27/i=15/a=014.

[54] L. Sharma et al. "Polarization transfer in the inner-shell photoionization of sodiumlike ions". In: *Phys. Rev. A* **81** (2010), p. 023419. DOI: 10.1103/PhysRevA.81.023419.

[55] M. K. Inal, A. Surzhykov, and S. Fritzsche. "Linear polarization of the $2p^5 3s \rightarrow 2p^6$ lines following the inner-shell photoionization of sodiumlike ions". In: *Phys. Rev. A* **72** (2005), p. 042720. DOI: 10.1103/PhysRevA.72.042720.

[56] K.-N. Huang. "Angular distribution and spin polarization of Auger electrons following photoionization and photoexcitation". In: *Phys. Rev. A* **26** (1982), p. 2274. DOI: 10.1103/PhysRevA.26.2274.

[57] K. Ueda et al. "Experimental Determination of Auger-Decay Amplitudes from the Angular Correlations in Auger Cascade Following the $2p \rightarrow 4s$ Photoexcitation in Ar". In: *Phys. Rev. Lett.* **83** (1999), p. 5463. DOI: 10.1103/PhysRevLett.83.5463.

[58] S. Southworth et al. "Electron-spectroscopy study of inner-shell photoexcitation and ionization of Xe". In: *Phys. Rev. A* **28** (1983), p. 261. DOI: 10.1103/PhysRevA.28.261.

[59] N. Bohr. "I. On the constitution of atoms and molecules". In: *Philos. Mag. Ser. 6* **26** (1913), p. 1. DOI: 10.1080/14786441308634955.

[60] R. D. Cowan. *The Theory of Atomic Structure and Spectra*. Berkeley: University of California Press, 1981. ISBN: 9780520906150.

[61] I. Lindgren and J. Morrison. *Atomic many-body theory*. Berlin Heidelberg: Springer, 1986. DOI: 10.1007/978-3-642-96614-9.

[62] I. P. Grant. *Relativistic Quantum Theory of Atoms and Molecules: Theory and Computation*. New York: Springer-Verlag, 2007. DOI: 10.1007/978-0-387-35069-1.

[63] J. P. Desclaux. "A multiconfiguration relativistic DIRAC-FOCK program". In: *Comput. Phys. Commun.* **9** (1975), p. 31. DOI: http://dx.doi.org/10.1016/0010-4655(75)90054-5.

[64] I. P. Grant et al. "An atomic multiconfigurational Dirac-Fock package". In: *Comput. Phys. Commun.* **21** (1980), p. 207. DOI: http://dx.doi.org/10.1016/0010-4655(80)90041-7.

[65] K. G. Dyall et al. "GRASP: A general-purpose relativistic atomic structure program". In: *Comput. Phys. Commun.* **55** (1989), p. 425. DOI: http://dx.doi.org/10.1016/0010-4655(89)90136-7.

[66] F. A. Parpia, C. F. Fischer, and I. P. Grant. "GRASP92: A package for large-scale relativistic atomic structure calculations". In: *Comput. Phys. Commun.* **94** (1996), p. 249. DOI: http://dx.doi.org/10.1016/0010-4655(95)00136-0.

[67] P. Jönsson et al. "The grasp2K relativistic atomic structure package". In: *Comput. Phys. Commun.* **177** (2007), p. 597. DOI: http://dx.doi.org/10.1016/j.cpc.2007.06.002.

[68] S. Fritzsche. "The Ratip program for relativistic calculations of atomic transition, ionization and recombination properties". In: *Comput. Phys. Commun.* **183** (2012), p. 1525. DOI: http://dx.doi.org/10.1016/j.cpc.2012.02.016.

[69] N. M. Kabachnik et al. "Coherence and correlations in photoinduced Auger and fluorescence cascades in atoms". In: *Phys. Rep.* **451** (2007), p. 155. DOI: http://dx.doi.org/10.1016/j.physrep.2007.07.005.

[70] T. Kämpfer et al. "Linear polarization of the characteristic x-ray lines following inner-shell photoionization of tungsten". In: *Phys. Rev. A* **93** (2016), p. 033409. DOI: 10.1103/PhysRevA.93.033409.

[71] H. Kleinpoppen, B. Lohmann, and A. N. Grum-Grzhimailo. *Perfect/Complete Scattering Experiments: Probing Quantum Mechanics on Atomic and Molecular Collisions and Coincidences*. Berlin Heidelberg: Springer, 2013. DOI: 10.1007/978-3-642-40514-3.

[72] U. Kleiman and B. Lohmann. "Photoionization of closed-shell atoms: Hartree–Fock calculations of orientation and alignment". In: *J. Electron Spectrosc. Relat. Phenom.* **131-132** (2003), p. 29. DOI: http://dx.doi.org/10.1016/S0368-2048(03)00034-3.

[73] R. Diamant et al. "Structure of the W $L\alpha_{1,2}$ x-ray spectrum". In: *Phys. Rev. A* **63** (2001), p. 022508. DOI: 10.1103/PhysRevA.63.022508.

[74] J. Eichler and W. E. Meyerhof. *Relativistic Atomic Collisions*. San Diego: Academic Press, 1995. ISBN: 978-0-12-233675-1.

[75] J. R. Oppenheimer. "On the Quantum Theory of the Capture of Electrons". In: *Phys. Rev.* **31** (1928), p. 349. DOI: 10.1103/PhysRev.31.349.

[76] T. Stöhlker et al. "Angular Distribution Studies for the Time-Reversed Photoionization Process in Hydrogenlike Uranium: The Identification of Spin-Flip Transitions". In: *Phys. Rev. Lett.* **82** (1999), p. 3232. DOI: 10.1103/PhysRevLett.82.3232.

[77] T. Stöhlker et al. "Near-Threshold Photoionization of Hydrogenlike Uranium Studied in Ion-Atom Collisions via the Time-Reversed Process". In: *Phys. Rev. Lett.* **86** (2001), p. 983. DOI: 10.1103/PhysRevLett.86.983.

[78] T. Stöhlker et al. "L-Subshell Resolved Photon Angular Distribution of Radiative Electron Capture into He-like Uranium". In: *Phys. Rev. Lett.* **73** (1994), p. 3520. DOI: 10.1103/PhysRevLett.73.3520.

[79] T. Stöhlker et al. "1s Lamb Shift in Hydrogenlike Uranium Measured on Cooled, Decelerated Ion Beams". In: *Phys. Rev. Lett.* **85** (2000), p. 3109. DOI: 10.1103/PhysRevLett.85.3109.

[80] T. Stöhlker et al. "Radiative electron capture studied in relativistic heavy-ion–atom collisions". In: *Phys. Rev. A* **51** (1995), p. 2098. DOI: 10.1103/PhysRevA.51.2098.

[81] S. Tashenov et al. "First Measurement of the Linear Polarization of Radiative Electron Capture Transitions". In: *Phys. Rev. Lett.* **97** (2006), p. 223202. DOI: 10.1103/PhysRevLett.97.223202.

[82] G. A. Machicoane et al. "Internal dielectronic excitation in highly charged ions colliding with surfaces". In: *Phys. Rev. A* **65** (2002), p. 042903. DOI: 10.1103/PhysRevA.65.042903.

[83] J.-M. Bizau et al. "Photoionization of Highly Charged Ions Using an ECR Ion Source and Undulator Radiation". In: *Phys. Rev. Lett.* **84** (2000), p. 435. DOI: 10.1103/PhysRevLett.84.435.

[84] M. S. Pindzola et al. "Single photoionization of highly charged atomic ions including the full electromagnetic-field potential". In: *Phys. Rev. A* **85** (2012), p. 032701. DOI: 10.1103/PhysRevA.85.032701.

[85] S Fritzsche, P Indelicato, and T. Stöhlker. "Relativistic quantum dynamics in strong fields: photon emission from heavy, few-electron ions". In: *J. Phys. B* **38** (2005), S707. URL: http://stacks.iop.org/0953-4075/38/i=9/a=018.

[86] X. Ma et al. "Electron-electron interaction studied in strong central fields by resonant transfer and excitation with H-like U ions". In: *Phys. Rev. A* **68** (2003), p. 042712. DOI: 10.1103/PhysRevA.68.042712.

[87] A. Surzhykov et al. "$K\alpha_1$ radiation from heavy, heliumlike ions produced in relativistic collisions". In: *Phys. Rev. A* **74** (2006), p. 052710. DOI: 10.1103/PhysRevA.74.052710.

[88] A. Surzhykov et al. "Electron capture into few-electron heavy ions: Independent particle model". In: *Eur. Phys. J. D* **46** (2008), p. 27. ISSN: 1434-6079. DOI: 10.1140/epjd/e2007-00269-3.

[89] J Dubau, Y Garbuzov, and A Urnov. "Account for the influence of hyperfine interaction on the polarization of X-ray lines". In: *Phys. Scr.* **49** (1994), p. 39. URL: http://stacks.iop.org/1402-4896/49/i=1/a=006.

[90] R Bensaid, M. K. Inal, and J Dubau. "Polarization of line radiation due to mixed E1–M2 transitions. Application to hyperfine components of the heliumlike $1s2p\ ^3P_2 \rightarrow 1s^2\ ^1S_0$ line". In: *J. Phys. B* **39** (2006), p. 4131. URL: http://stacks.iop.org/0953-4075/39/i=20/a=011.

[91] A. Surzhykov et al. "Radiative electron capture into high-Z few-electron ions: Alignment of the excited ionic states". In: *Phys. Rev. A* **73** (2006), p. 032716. DOI: 10.1103/PhysRevA.73.032716.

[92] Z. W. Wu, A. Surzhykov, and S. Fritzsche. "Reply to "Comment on 'Hyperfine-induced modifications to the angular distribution of the $K\alpha_1$ x-ray emission' "". In: *Phys. Rev. A* **91** (2015), p. 056502. DOI: 10.1103/PhysRevA.91.056502.

[93] Z. W. Wu, S Fritzsche, and A Surzhykov. "Nuclear magnetic dipole moment effect on the angular distribution of the Kα lines". In: *Phys. Scr.* **T166** (2015), p. 014029. URL: http://stacks.iop.org/1402-4896/2015/i=T166/a=014029.

[94] W. R. Johnson. "Hyperfine quenching: review of experiment and theory". In: *Can. J. Phys.* **89** (2011), p. 429. DOI: 10.1139/p11-018.

[95] N. Stone. "Table of nuclear magnetic dipole and electric quadrupole moments". In: *At. Data Nucl. Data Tables* **90** (2005), p. 75. DOI: http://dx.doi.org/10.1016/j.adt.2005.04.001.

[96] M. Levine et al. "The use of an electron beam ion trap in the study of highly charged ions". In: *Nucl. Instr. Meth. Phys. Res. B* **43** (1989), p. 431. DOI: http://dx.doi.org/10.1016/0168-583X(89)90386-8.

[97] M. Schulz et al. "X-ray emission from slow highly charged Ar ions interacting with a Ge surface". In: *Phys. Rev. A* **44** (1991), p. 1653. DOI: 10.1103/PhysRevA.44.1653.

[98] P. Beiersdorfer et al. "X-Ray Emission Following Low-Energy Charge Exchange Collisions of Highly Charged Ions". In: *Phys. Rev. Lett.* **85** (2000), p. 5090. DOI: 10.1103/PhysRevLett.85.5090.

[99] K. Honda, K. Mima, and F. Koike. "M-shell x-ray spectra of laser-produced gold plasmas". In: *Phys. Rev. E* **55** (1997), p. 4594. DOI: 10.1103/PhysRevE.55.4594.

[100] Z. W. Wu et al. "Determination of small level splittings in highly charged ions via angle-resolved measurements of characteristic x rays". In: *Phys. Rev. A* **90** (2014), p. 052515. DOI: 10.1103/PhysRevA.90.052515.

[101] E. V. Gryzlova et al. "Angular correlations between two electrons emitted in the sequential two-photon double ionization of atoms". In: *J. Phys. B* **43** (2010), p. 225602. URL: http://stacks.iop.org/0953-4075/43/i=22/a=225602.

[102] S Fritzsche et al. "Angular distributions and angular correlations in sequential two-photon double ionization of atoms". In: *J. Phys. B* **41** (2008), p. 165601. URL: http://stacks.iop.org/0953-4075/41/i=16/a=165601.

[103] S Fritzsche et al. "Sequential two-photon double ionization of the 4d shell in xenon". In: *J. Phys. B* **44** (2011), p. 175602. URL: http://stacks.iop.org/0953-4075/44/i=17/a=175602.

[104] K Ueda et al. "Experimental and theoretical study of the Auger cascade following 2p→4s photoexcitation in Ar". In: *J. Phys. B* **34** (2001), p. 107. URL: http://stacks.iop.org/0953-4075/34/i=1/a=308.

[105] K Ueda et al. "Angular correlation between Auger electrons successively emitted from photoexcited resonances in Kr and Xe". In: *J. Phys. B* **36** (2003), p. 319. URL: http://stacks.iop.org/0953-4075/36/i=2/a=312.

[106] J. Eichler, A. Ichihara, and T. Shirai. "Alignment caused by photoionization and in radiative electron capture into excited states of hydrogenic high-Z ions". In: *Phys. Rev. A* **58** (1998), p. 2128. DOI: 10.1103/PhysRevA.58.2128.

[107] J. H. Scofield. "Angular distribution of cascade x rays following radiative recombination from a beam". In: *Phys. Rev. A* **44** (1991), p. 139. DOI: 10.1103/PhysRevA.44.139.

[108] E. G. Drukarev et al. "Angular distribution of characteristic photons after radiative electron capture at strong central fields". In: *Phys. Rev. A* **74** (2006), p. 022717. DOI: 10.1103/PhysRevA.74.022717.

[109] Z. W. Wu et al. "Linear polarization of x-rays emitted in the decay of highly-charged ions via overlapping resonances". In: *J. Phys. Conf. Ser.* **635** (2015), p. 012020. URL: http://stacks.iop.org/1742-6596/635/i=1/a=012020.

[110] H. I. Ewen and E. M. Purcell. "Observation of a Line in the Galactic Radio Spectrum: Radiation from Galactic Hydrogen at 1,420 Mc./sec". In: *Nature* **168** (1951), p. 356. DOI: 10.1038/168356a0.

[111] I. Klaft et al. "Precision Laser Spectroscopy of the Ground State Hyperfine Splitting of Hydrogenlike $^{209}Bi^{82+}$". In: *Phys. Rev. Lett.* **73** (1994), p. 2425. DOI: 10.1103/PhysRevLett.73.2425.

[112] M. Tomaselli et al. "Ground-state magnetization of ^{209}Bi in a dynamic-correlation model". In: *Phys. Rev. C* **51** (1995), p. 2989. DOI: 10.1103/PhysRevC.51.2989.

[113] H. Persson et al. "Self-Energy Correction to the Hyperfine Structure Splitting of Hydrogenlike Atoms". In: *Phys. Rev. Lett.* **76** (1996), p. 1433. DOI: 10.1103/PhysRevLett.76.1433.

[114] P. Sunnergren et al. “Radiative corrections to the hyperfine-structure splitting of hydrogenlike systems”. In: *Phys. Rev. A* **58** (1998), p. 1055. DOI: 10.1103/PhysRevA.58.1055.

[115] T. Nagasawa, A. Haga, and M. Nakano. “Hyperfine splitting of hydrogenlike atoms based on relativistic mean field theory”. In: *Phys. Rev. C* **69** (2004), p. 034322. DOI: 10.1103/PhysRevC.69.034322.

[116] J. R. Crespo López-Urrutia et al. “Direct Observation of the Spontaneous Emission of the Hyperfine Transition $F = 4$ to $F = 3$ in Ground State Hydrogenlike $^{165}Ho^{66+}$ in an Electron Beam Ion Trap”. In: *Phys. Rev. Lett.* **77** (1996), p. 826. DOI: 10.1103/PhysRevLett.77.826.

[117] J. R. Crespo López-Urrutia et al. “Nuclear magnetization distribution radii determined by hyperfine transitions in the $1s$ level of H-like ions $^{185}\mathrm{Re}^{74+}$ and $^{187}\mathrm{Re}^{74+}$”. In: *Phys. Rev. A* **57** (1998), p. 879. DOI: 10.1103/PhysRevA.57.879.

[118] P. Beiersdorfer et al. “Hyperfine structure of hydrogenlike thallium isotopes”. In: *Phys. Rev. A* **64** (2001), p. 032506. DOI: 10.1103/PhysRevA.64.032506.

[119] M. Tomaselli et al. “Hyperfine splitting of hydrogenlike thallium”. In: *Phys. Rev. A* **65** (2002), p. 022502. DOI: 10.1103/PhysRevA.65.022502.

[120] P. Seelig et al. “Ground State Hyperfine Splitting of Hydrogenlike $^{207}\mathrm{Pb}^{81+}$ by Laser Excitation of a Bunched Ion Beam in the GSI Experimental Storage Ring”. In: *Phys. Rev. Lett.* **81** (1998), p. 4824. DOI: 10.1103/PhysRevLett.81.4824.

[121] V. M. Shabaev et al. “Towards a Test of QED in Investigations of the Hyperfine Splitting in Heavy Ions”. In: *Phys. Rev. Lett.* **86** (2001), p. 3959. DOI: 10.1103/PhysRevLett.86.3959.

[122] A. V. Volotka et al. “Test of Many-Electron QED Effects in the Hyperfine Splitting of Heavy High-Z Ions”. In: *Phys. Rev. Lett.* **108** (2012), p. 073001. DOI: 10.1103/PhysRevLett.108.073001.

[123] P. Beiersdorfer et al. “Hyperfine Splitting of the $2s_{1/2}$ and $2p_{1/2}$ Levels in Li- and Be-like Ions of $^{141}_{59}\mathrm{Pr}$”. In: *Phys. Rev. Lett.* **112** (2014), p. 233003. DOI: 10.1103/PhysRevLett.112.233003.

[124] M. Lochmann et al. "Observation of the hyperfine transition in lithium-like bismuth $^{209}Bi^{80+}$: Towards a test of QED in strong magnetic fields". In: *Phys. Rev. A* **90** (2014), p. 030501. DOI: 10.1103/PhysRevA.90.030501.

[125] P. Indelicato, F. Parente, and R. Marrus. "Effect of hyperfine structure on the 2 $^3P_1$ and the 2 $^3P_0$ lifetime in heliumlike ions". In: *Phys. Rev. A* **40** (1989), p. 3505. DOI: 10.1103/PhysRevA.40.3505.

[126] W. R. Johnson, K. T. Cheng, and D. R. Plante. "Hyperfine structure of 2^3P levels of heliumlike ions". In: *Phys. Rev. A* **55** (1997), p. 2728. DOI: 10.1103/PhysRevA.55.2728.

[127] J. Rzadkiewicz et al. "Selective population of the $[1s2s]$ $^1S_0$ and $[1s2s]$ $^3S_1$ states of He-like uranium". In: *Phys. Rev. A* **74** (2006), p. 012511. DOI: 10.1103/PhysRevA.74.012511.

[128] S. Trotsenko et al. "Spectral Shape of the Two-Photon Decay of the 2 $^1S_0$ State in He-Like Tin". In: *Phys. Rev. Lett.* **104** (2010), p. 033001. DOI: 10.1103/PhysRevLett.104.033001.

[129] P. H. Mokler et al. "Single transfer-excitation resonance observed via the two-photon decay in He-like Ge^{30+}". In: *Phys. Rev. Lett.* **65** (1990), p. 3108. DOI: 10.1103/PhysRevLett.65.3108.

[130] A. Dalgarno and D. R. Bates. "Two-photon Decay of Singlet Metastable Helium". In: *Mon. Not. R. Astron. Soc.* **131** (1966), p. 311. DOI: 10.1093/mnras/131.2.311.

[131] A. V. Volotka et al. "Interelectronic-interaction effects on the two-photon decay rates of heavy He-like ions". In: *Phys. Rev. A* **83** (2011), p. 062508. DOI: 10.1103/PhysRevA.83.062508.

[132] S. Tashenov et al. "Measurement of the Correlation between Electron Spin and Photon Linear Polarization in Atomic-Field Bremsstrahlung". In: *Phys. Rev. Lett.* **107** (2011), p. 173201. DOI: 10.1103/PhysRevLett.107.173201.

[133] V. Shabaev. "Two-time Green's function method in quantum electrodynamics of high-Z few-electron atoms". In: *Phys. Rep.* **356** (2002), p. 119. DOI: http://dx.doi.org/10.1016/S0370-1573(01)00024-2.

[134] O. Y. Andreev et al. "QED theory of the spectral line profile and its applications to atoms and ions". In: *Phys. Rep.* **455** (2008), p. 135. DOI: http://dx.doi.org/10.1016/j.physrep.2007.10.003.

[135] Z. W. Wu et al. “Level sequence and splitting identification of closely spaced energy levels by angle-resolved analysis of fluorescence light”. In: *Phys. Rev. A* **93** (2016), p. 063413. DOI: 10.1103/PhysRevA.93.063413.

[136] D. A. Varshalovich, A. N. Moskalev, and V. K. Khersonskii. *Quantum Theory of Angular Momentum*. Singapore: World Scientific, 1988. ISBN: 978-981-4578-28-8.

[137] K. T. Cheng, M. H. Chen, and W. R. Johnson. “Hyperfine quenching of the $2s2p\ ^3P_0$ state of berylliumlike ions”. In: *Phys. Rev. A* **77** (2008), p. 052504. DOI: 10.1103/PhysRevA.77.052504.

[138] P. Indelicato, V. M. Shabaev, and A. V. Volotka. “Interelectronic-interaction effect on the transition probability in high-Z He-like ions”. In: *Phys. Rev. A* **69** (2004), p. 062506. DOI: 10.1103/PhysRevA.69.062506.

[139] A. N. Artemyev et al. “QED calculation of the $n = 1$ and $n = 2$ energy levels in He-like ions”. In: *Phys. Rev. A* **71** (2005), p. 062104. DOI: 10.1103/PhysRevA.71.062104.

[140] F. Ferro, A. Surzhykov, and T. Stöhlker. “Hyperfine transitions in He-like ions as a tool for nuclear-spin-dependent parity-nonconservation studies”. In: *Phys. Rev. A* **83** (2011), p. 052518. DOI: 10.1103/PhysRevA.83.052518.

[141] B. Marx et al. “High-Precision X-Ray Polarimetry”. In: *Phys. Rev. Lett.* **110** (2013), p. 254801. DOI: 10.1103/PhysRevLett.110.254801.

List of Figures

3.1 Degree of linear polarization of the $Ly\text{-}\alpha_1$ ($3d_{5/2} \rightarrow 2p_{3/2}$; blue squares) and $Ly\text{-}\alpha_2$ ($3d_{3/2} \rightarrow 2p_{3/2}$; black circles) fluorescence emission lines following the inner-shell $2p_{3/2}$ photoionization of tungsten by an unpolarized photon beam, as functions of the ionizing photon energy in the range of 10–23 keV. The photon energies of the $Ly\text{-}\alpha_1$ and $Ly\text{-}\alpha_2$ lines are calculated to be 8398 eV and 8335 eV, respectively. Calculations are performed within the MCDF method. 28

3.2 The same as Figure 3.1 but together with a comparison with the experimental results measured by a crystal-based spectropolarimeter. 29

4.1 Scheme of the low-lying energy levels of heliumlike ions with nuclear spin $I = 1/2$. The energy splittings in the fine- and hyperfine-structure levels are estimated here for the ions with nuclear charge in the range $50 \leq Z \leq 81$. 38

4.2 Effective anisotropy parameters $\beta_2^{\rm eff}$ of the characteristic $K\alpha_1$ emission as functions of the magnetic dipole moment μ_I following the REC into the two excited $1s2p_{3/2}\ ^{1,3}P_{1,2}$ levels of (finally) heliumlike projectile ions with a kinetic energy of $T_p = 50$ MeV/u. Results are shown for the ions $^{A}_{50}\mathrm{Sn}^{48+}$ ($A = 119$, 113, 121; black points), $^{A}_{54}\mathrm{Xe}^{52+}$ ($A =$ 129, 127, 125, 123; red squares) and $^{A}_{81}\mathrm{Tl}^{79+}$ ($A = 187$, 205, 207; blue triangles) as well as their zero-spin counterparts (shadowed area), respectively. Lines are drawn just to guide the eyes. 42

4.3 Effective anisotropy parameter $\beta_2^{\rm eff}$ of the characteristic $K\alpha_1$ emission as functions of the projectile energy T_p following the REC into the excited $1s2p_{3/2}\ ^{1,3}P_{1,2}$ levels of (finally) heliumlike ions. Results are shown for the ions $^{119}_{50}\mathrm{Sn}^{48+}$ ($I = 1/2$, $\mu_I = -1.047\,\mu_N$; left panel) and $^{207}_{81}\mathrm{Tl}^{79+}$ ($I = 1/2$, $\mu_I = +1.876\,\mu_N$; right panel), respectively. Computations for the two spin-1/2 ions (black solid lines) are compared with those for the corresponding zero-spin ions (blue dashed lines). . 44

4.4 Angular distribution of the $K\alpha_1$ characteristic emission following the REC into the excited $1s2p_{3/2}$ $^{1,3}P_{1,2}$ levels of (finally) helium-like ions. Results for the spin-1/2 isotopes from Fig. 4.3 (black solid lines) are compared with computations for zero-spin isotopes (blue dashed lines) of the same element. All calculations were performed within the projectile frame and for projectile ions with kinetic energy $T_p = 10$ MeV/u. 45

4.5 The same as Figure 4.4 but for the projectile energy $T_p = 50$ MeV/u and for three different xenon isotopes with nuclear spin $I \geq 1/2$ and comparable magnetic dipole moment μ_I: $^{129}_{54}\mathrm{Xe}^{52+}$ ($I = 1/2$, $\mu_I = -0.778\,\mu_N$; left panel), $^{121}_{54}\mathrm{Xe}^{52+}$ ($I = 5/2$, $\mu_I = -0.701\,\mu_N$; middle panel), and $^{137}_{54}\mathrm{Xe}^{52+}$ ($I = 7/2$, $\mu_I = -0.968\,\mu_N$; right panel). 46

5.1 Level scheme of the two-step radiative cascade (5.1). The ion that is assumed to be initially in the doubly excited level $\alpha_i J_i$ decays radiatively to the ground level $\alpha_f J_f$ via the two intermediate overlapping resonances αJ and $\alpha' J'$. While the γ_1 and γ_2 photons can be distinguished energetically, no further line structure could be resolved individually due to (partial) overlap of the αJ and $\alpha' J'$ resonances. . 49

5.2 Level scheme and dominant decay channels of the doubly excited (initial) levels $1s2p^2$ $J_i = 1/2, 3/2$ for lithiumlike W^{71+} ions, together with their branching fractions estimated. About 0.01% of them proceeds via the radiative cascade (5.7) of interest as marked in blue. . . 54

5.3 Level splitting $\Delta\omega$ of the two intermediate $1s2s2p_{1/2}$ $J = 1/2, 3/2$ resonances as a function of nuclear charge Z along the lithium isoelectronic sequence. A crossing of these two resonances occurs among $74 \leq Z \leq 79$ approximately. 57

5.4 Anisotropy parameters (5.13) of the γ_2 angular distribution as functions of the level splitting $\Delta\omega$. Results are shown for four assumed alignment parameters of the $1s2p^2$ $J_i = 3/2$ resonance of lithiumlike W^{71+} ions owing to its prior excitations: $\mathcal{A}_2 = 1.0$ (black solid line), 0.5 (red dashed lined), -0.5 (blue dashed-dotted line), and -1.0 (gray dotted line). 58

5.5 Angular distribution of the second-step γ_2 photons emitted in the decay cascade (5.7). Results are shown for two assumed alignment parameters $\mathcal{A}_2 = -1.0$ (left panel) and 1.0 (right panel) of the $1s2p^2\ J_i = 3/2$ resonance of lithiumlike W^{71+} ions. For each of them, four different level splittings of the intermediate resonances $1s2s2p_{1/2}\ J = 1/2, 3/2$ are assumed: $\Delta\omega = 0.01$ a.u. (black solid line), 0.1 a.u. (red dashed line), 0.5 a.u. (blue dash-dotted line), and 1.0 a.u. (pink dotted line). 59

5.6 Degree of linear polarization of the γ_2 photons as functions of the emission angle θ. Results are shown for different combinations between the alignment $\mathcal{A}_2$ of the $1s2p^2\ J_i = 3/2$ level of lithiumlike W^{71+} ions and the splitting $\Delta\omega$ (a.u.) of the $1s2s2p_{1/2}\ J = 1/2, 3/2$ resonances: -1 and 0.1 (magenta dotted line), -1 and 0.3 (blue dash-dotted line), 1 and 0.1 (black solid line) as well as 1 and 0.3 (red dashed line). 60

5.7 Degree of linear polarization of the second-step γ_2 photons as functions of the level splitting. Results are shown here for those of them that are emitted under $\theta = 90^o$ for four assumed alignment parameters of the $1s2p^2\ J_i = 3/2$ level: $\mathcal{A}_2 = -1.0$ (black solid line), -0.5 (blue dashed line), 0.5 (magenta dotted line), and 1.0 (red dash-dotted line). 61

5.8 Anisotropy parameters (5.9) and (5.11) for the photon-photon angular correlation in the radiative cascade (5.7) which starts initially from the resonances $1s2p^2\ J_i = 1/2$ (left panel) and $1s2p^2\ J_i = 3/2$ (right panel) of lithiumlike W^{71+} ions, respectively. In the latter, these parameters are presented here as functions of the level splitting $\Delta\omega$ for four assumed alignment parameters: $\mathcal{A}_2 = -1.0$ (black solid line), -0.5 (red dotted line), 0.0 (blue dashed-dotted line), and 0.5 (pink dotted line). 62

5.9 Photon-photon angular correlation in the respective radiative cascades (5.7) of the initial $1s2p^2\ J_i = 1/2$ (left panel) and $1s2p^2\ J_i = 3/2$ resonances of lithiumlike W^{71+} ions. In the latter, two different alignment parameters $\mathcal{A}_2 = -1.0$ (middle panel) and 0.0 (right panel) are assumed. Results are shown for the same level splittings of the intermediate resonances and by using the same symbols as in Figure 5.5. . 63

6.1 Level scheme of low-lying fine- and hyperfine-structure levels in heliumlike $^{71}_{31}\mathrm{Ga}^{29+}$ ($I = 3/2$, $\mu_I = +2.56227\,\mu_N$) ions and the geometry for the two-step radiative decay. While the first-step decay is stimulated by a laser beam with γ_1 photon energy $\hbar\omega$ and minimum intensity I_{min}, the second-step one occurs spontaneously with the emission of fluorescence γ_2 photons. 70

6.2 Anisotropy parameter β (left panel) and degree of linear polarization P_1 (right panel) of the hyperfine $1s2p\ ^3P_1, F = 1/2, 3/2, 5/2 \rightarrow 1s^2\ ^1S_0, F_f = 3/2$ fluorescence emissions from heliumlike $^{71}_{31}\mathrm{Ga}^{29+}$ ($I = 3/2$, $\mu_I = +2.56227\,\mu_N$) ions as functions of photon energy $\hbar\omega$ of the incident light γ_1. Results are shown for the calculated hyperfine constant $A_J = 0.0278$ eV (black solid lines) as given in Table 6.1 and also for two assumed values, $0.8A_J$ (red dash-dotted lines) and $1.2A_J$ (blue dash-dot-dotted lines), which differ by just 20%. 75

6.3 Anisotropy parameter of the hyperfine $1s2p\ ^3P_1, F = 3/2, 5/2, 7/2 \rightarrow 1s^2\ ^1S_0, F_f = 5/2$ and $1s2p\ ^3P_1, F = 7/2, 9/2, 11/2 \rightarrow 1s^2\ ^1S_0, F_f = 9/2$ fluorescence emissions from heliumlike $^{141}_{59}\mathrm{Pr}^{57+}$ ($I = 5/2$, $\mu_I = +4.2754\,\mu_N$; left panel) and $^{209}_{83}\mathrm{Bi}^{81+}$ ($I = 9/2$, $\mu_I = +4.1103\,\mu_N$; right panel) ions, respectively, as functions of photon energy $\hbar\omega$ of the incident light γ_1. Results are shown for the calculated hyperfine constant $A_J = 0.2573$ eV and 0.5457 eV (black solid lines), respectively, and also for two assumed values, $0.8A_J$ (red dash-dotted lines) and $1.2A_J$ (blue dash-dot-dotted lines) each, which differ by just 20%. 76

6.4 The same as Figure 6.3 but for the degree of linear polarization P_1. . 77

List of Tables

6.1 Table of isotopes with nuclear spin I and magnetic dipole moment μ_I in units of the nuclear magneton μ_N considered. While the hyperfine constant A_J (eV) and natural linewidth Γ (eV) of the level $1s2p\ ^3P_1$ of their corresponding heliumlike ions are presently calculated, the transition energies (eV) of both $1s2s\ ^1S_0 \rightarrow 1s2p\ ^3P_1$ (1st-step) and $1s2p\ ^3P_1 \rightarrow 1s^2\ ^1S_0$ (2nd-step) decays are taken from Ref. [139]. Moreover, minimum intensities $\mathcal{I}_{\rm min}$ (W/cm^2) of the stimulating laser are estimated. 74

Acknowledgements

During the course of my PhD study here in Jena, I have received a lot of help and support from a number of people, some of whom have also contributed both directly and indirectly to the success of this work as presented in the thesis in its present form. On this page, I would like to mention and acknowledge all of them.

First of all, I sincerely thank my supervisor Prof. Dr. Stephan Fritzsche for all of his support, encouragement, and care always throughout all the period. Without his constant support and elaborate guidance, this work would have never been possible. To be honest, from the daily discussions I was fully impressed by his rigorous attitude towards scientific research. Here, it is memorable for me to keep his quote "what's going on?" and the "building a house" story with regard to scientific writing, which sometimes made me nervous but all the time pushed me to make progress.

I would like to deliver my special thanks to Prof. Dr. Andrey Surzhykov from the National Metrology Institute of Germany, who helped me settle down academically in the group during my first 2 months' visit, and afterwards, also provided me with numerous guidance and support on my work. Moreover, I deliver my special thanks also to Dr. Andrey V. Volotka for sharing his good scientific ideas and also for very helpful discussions, which made the success of part of my PhD work.

I express my thanks to Prof. Dr. Nikolay M. Kabachnik and Dr. Alexei N. Grum-Grzhimailo from Lomonosov Moscow State University for very useful discussions on the density matrix theory and its application to the studies of photon polarization and angular correlation phenomena.

A special acknowledgement is devoted to my "alma mater" — Northwest Normal University of China, where I officially started my study in physics. I thank heartily Prof. Dr. Chenzhong Dong for bringing me into the field of atomic physics and also for encouraging me studying abroad. In addition, I thank Dr. Denghong Zhang for his financial support on my business trip.

A pleasant and friendly working environment is always appreciated. I would like to thank all of my current and former colleagues from the theoretical atomic physics group in the Helmholtz Institute Jena: Dr. Daniel Seipt, Dr. Thorsten Jahrsetz, Anton Peshkov, Randolf Beerwerth, Jiri Hofbrucker, Sebastian Stock, Robert Müller, Dr. Oliver Matula, Dr. Vladimir Yerokhin, Dr. Anton Artemyev, Dr. Valery Serbo,

Dr. Biplab Goswami, Moazzam Bilal, Birger Böning, Willi Paufler, Dr. Jacinda Ginges, Shahram Panahiyan, Dr. Krishna Prasanna, Tobias Bucher, Vladimir Zaytsev, Kunming Ruan, Erik Abraham, Marie Scholz-Marggraf, Stefan Tietze, Wilko Middens, Katharina Wölf, Antonio Zegarra. I thank my friends (T.J., A.P., R.B., J.H., and A.V.) here in Jena for their helps to me in anyway and also for the pleasant biking and pingpong time spent together.

I would also like to acknowledge the Helmholtz Graduate School for Hadron and Ion Research (HGS-HIRe) and the Research School for Advanced Photon Science (RS-APS) for funding my PhD study and for providing good educational opportunities (soft-skill courses and lecture weeks). In particular, I thank Dr. Günter Weber, Dr. Renate Märtin and Barbara Kirchner for their warm help to me on the affairs within the RS-APS and the Helmholtz Institute Jena. Moreover, the Wilhelm and Else Heraeus Foundation is also acknowledged for supporting me to attend the DPG (Deutsche Physikalische Gesellschaft) Spring Meetings.

I would like to express my deepest gratitude to my family for the consistent love and support that I have received in the past 30 years — my mother Yinhe Wei, my father Shunfu Wu, and my sister Caifeng Wu. The same deepest gratitude of mine goes also to my parents-in-law for their trust, love, and support.

Finally, to the love of my life — my beautiful wife, Meimei Zhao — your unconditional love and support, in the good times as well as the tough during the past 10 years, is a true blessing for us. Thank you!

Zhongwen Wu
7th, Feb. 2017, Jena

Curriculum Vitae

Personal Information

Name	Zhongwen Wu
Gender	Male
Nationality	Chinese
Date of birth	28.09.1987
Place of birth	Gansu, P.R. China

School education

09.1993 – 06.1999	Wujiahe Central Primary School of Gangu, Gansu, China
09.1999 – 06.2002	Wujiahe Junior High School of Gangu, Gansu, China
09.2002 – 06.2005	No. 4 Senior High School of Gangu, Gansu, China

University education

09.2005 – 06.2009	Bachelor in Physics, Department of Physics, Northwest Normal University, Lanzhou, China
09.2009 – 06.2012	Master in Atomic and Molecular Physics, Department of Physics, Northwest Normal University, Lanzhou, China
01.2014 – 06.2017	PhD in Theoretical Atomic Physics, Faculty of Physics and Astronomy, Friedrich Schiller University Jena, Germany

Employment

06.2012 – 04.2013	Research fellow, Key Laboratory of Atomic and Molecular Physics & Functional Materials of Gansu Province, Northwest Normal University, Lanzhou, China
05.2013 – 06.2017	Research fellow, Helmholtz Institute Jena, Germany

Jena, den

.....

Zhongwen Wu

Publications

As part of the PhD study, the author has contributed to the following publications:

- Z. W. Wu, A. Surzhykov, and S. Fritzsche, "*Hyperfine-induced modifications to the angular distribution of the $K\alpha_1$ x-ray emission*", Phys. Rev. A **89**, 022513 (2014).
- Z. W. Wu, N. M. Kabachnik, A. Surzhykov, C. Z. Dong, and S. Fritzsche, "*Determination of small level splittings in highly charged ions via angle-resolved measurements of characteristic x rays*", Phys. Rev. A **90**, 052515 (2014). — (Selected as an Editor's Suggestion and highlight paper.)
- Z. W. Wu, Y. Z. Zhang, Y. B. Fu, A. Surzhykov, S. Fritzsche, and C. Z. Dong, "*Dielectronic recombination rate coefficients of initially rubidium-like tungsten*", Eur. Phys. J. D **69**, 140 (2015).
- Z. W. Wu, A. Surzhykov, N. M. Kabachnik, C. Z. Dong, and S. Fritzsche, "*Linear polarization of x-rays emitted in the decay of highly-charged ions via overlapping resonances*", J. Phys. Conf. Ser. **635**, 012020 (2015).
- Z. W. Wu, A. Surzhykov, and S. Fritzsche, "*Reply to "Comment on 'Hyperfine-induced modifications to the angular distribution of the $K\alpha_1$ x-ray emission' "* ", Phys. Rev. A **91**, 056502 (2015).
- Z. W. Wu, S. Fritzsche, and A. Surzhykov, "*Nuclear magnetic dipole moment effect on the angular distribution of the $K\alpha$ lines*", Phys. Scr. **T166**, 014029 (2015).
- Z. W. Wu, A. V. Volotka, A. Surzhykov, C. Z. Dong, and S. Fritzsche, "*Level sequence and splitting identification of closely spaced energy levels by angle-resolved analysis of fluorescence light*", Phys. Rev. A **93**, 063413 (2016).
- T. Kämpfer, I. Uschmann, Z. W. Wu, A. Surzhykov, S. Fritzsche, E. Förster, and G. G. Paulus, "*Linear polarization of the characteristic x-ray lines following inner-shell photoionization of tungsten*", Phys. Rev. A **93**, 033409 (2016).
- Z. W. Wu, A. V. Volotka, C. Z. Dong, and S. Fritzsche, "*Dielectronic recombination of highly charged ions with spin-polarized electrons*", Nucl. Instr. Meth. Phys. Res. B, in press (2017).
- Z. W. Wu, A. V. Volotka, A. Surzhykov, and S. Fritzsche, "*Novel angle-resolved x-ray spectroscopic scheme to determine overlapping hyperfine splittings in highly charged helium-like ions*", Phys. Rev. A, under review (2017).

Ehrenwörtliche Erklärung (Declaration of Authorship)

Ich erkläre hiermit ehrenwörtlich, dass ich die vorliegende Arbeit selbstständig, ohne unzulässige Hilfe Dritter und ohne Benutzung anderer als der angegebenen Hilfsmittel und Literatur angefertigt habe. Die aus anderen Quellen direkt oder indirekt übernommenen Daten und Konzepte sind unter Angabe der Quelle gekennzeichnet.

Bei der Auswahl und Vorbereitung dieser Arbeit haben mir meine Betreuer und die Koautoren der oben genannten Publikationen unentgeldlich geholfen.

Weitere Personen waren an der inhaltlich-materiellen Erstellung der vorliegenden Arbeit nicht beteiligt. Insbesondere habe ich hierfür nicht die entgeltliche Hilfe von Vermittlungs- bzw. Beratungsdiensten (Promotionsberater oder andere Personen) in Anspruch genommen. Niemand hat von mir unmittelbar oder mittelbar geldwerte Leistungen für Arbeiten erhalten, die im Zusammenhang mit dem Inhalt der vorgelegten Dissertation stehen.

Die Arbeit wurde bisher weder im In- noch im Ausland in gleicher oder ähnlicher Form einer anderen Prüfungsbehörde vorgelegt.

Die geltende Promotionsordnung der Physikalisch-Astronomischen Fakultät ist mir bekannt.

Ich versichere ehrenwörtlich, dass ich nach bestem Wissen die reine Wahrheit gesagt und nichts verschwiegen habe.

Jena, den

.....

Zhongwen Wu